RANS/PDF AND LES/FDF FOR PREDICTION OF TURBULENT PREMIXED FLAMES

by

Server Levent Yılmaz

Submitted to the Graduate Faculty of

the Swanson School of Engineering in partial fulfillment

of the requirements for the degree of

Doctor of Philosophy

University of Pittsburgh

2008

UNIVERSITY OF PITTSBURGH

SWANSON SCHOOL OF ENGINEERING

This dissertation was presented

by

Server Levent Yılmaz

It was defended on

November 12th 2008

and approved by

Dr. Peyman Givi, William Kepler Whiteford Professor of Mechanical Engineering and Materials Science

Dr. Minking K. Chyu, Leighton Orr Professor and Chairman of Mechanical Engineering and Materials Science

Dr. Giovanni P. Galdi, William Kepler Whiteford Professor of Mechanical Engineering and Materials Science

Dr. William J. Layton, Professor of Mathematics

Dissertation Director: Dr. Peyman Givi, William Kepler Whiteford Professor of Mechanical Engineering and Materials Science

RANS/PDF AND LES/FDF FOR PREDICTION OF TURBULENT PREMIXED FLAMES

Server Levent Yılmaz, Ph.D.

University of Pittsburgh, 2008

Probability density function (PDF) and filtered density function (FDF) methodologies are developed and implemented, respectively, for Reynolds-averaged Navier-Stokes (RANS) and large eddy simulation (LES) of turbulent premixed flames. RANS predictions are made of a lean premixed bluff-body flame via the joint velocity-scalar-frequency PDF model. LES of a premixed Bunsen-burner flame is conducted via the scalar FDF methodology. Both simulations employ finite rate kinetics via a reduced methane chemistry mechanism to account for combustion. Prediction results are compared with experimental data, and are shown to capture some of the intricate physics of turbulent premixed combustion.

Keywords: large eddy simulation, filtered density function, Reynolds-averaged Navier-Stokes, probability density function, turbulent reacting flows, lean premixed combustion.

TABLE OF CONTENTS

LIST OF TABLES

LIST OF FIGURES

NOMENCLATURE

Roman

C_0 : model parameter in the SLM equation

C_3, C_4 : model parameters in the equation for ω

C_I : SGS viscosity model parameter

c_p : constant pressure specific heat

C_R : SGS viscosity model parameter

c_v : constant volume specific heat

C_ϕ : model parameter in the LMSE mixing model

C_Ω : constant in the definition of Ω (in Chapter 2)

C_Ω : model parameter for SGS mixing (in Chapter 3)

$C_{\omega 1}, C_{\omega 2}$: model parameters in the equation for ω

d : reference diameter

D_i : drift coefficient in the Langevin equation

Da : Damköhler number

$\mathcal{E}$: SGS kinetic energy resolved with respect to the reference velocity $\mathcal{U}$

E : diffusion coefficient in the Langevin equation

f : probability density function (in Chapter 2)

f : the conserved scalar (in Chapter 3)

F_L : the scalar filtered mass density function

$\mathcal{G}$: filter kernel

h : enthalpy

h_s : equivalent enthalpy

J_i^α : scalar (heat or mass) flux

k : turbulent kinetic energy

k_{bk} : backward reaction rate coefficient

k_{fk} : forward reaction rate coefficient

L_i : air entrainment (pilot/air mixing layer) height

Le : Lewis number

$\mathcal{M}_\alpha$: molar mass of species α

M_i^α : SGS scalar fluxes

N : total number of realizations

N_E : number of MC particles inside the ensemble domain

N_S : number of species

P : rate of production of turbulent kinetic energy

p : pressure

$\dot{q}$: heat source for h_s due to chemical reaction

R : mixture gas constant

r : number of reactions in a chemical mechanism

$R(\boldsymbol{x}, t)$: a random variable

R^0 : universal gas constant

Re : Reynolds number

$\mathcal{S}_{ij}$: strain rate tensor

S_α : chemical source term

S_ω : mean source of turbulence frequency

Sc_t : SGS Schmidt number

T : temperature

t : time

T_{ij} : SGS stress tensor

$\boldsymbol{\mathcal{U}}$: reference velocity vector used in MKEV SGS model

$\boldsymbol{u}$: Eulerian velocity

$\boldsymbol{u}^*$: velocity vector used in the calculation of $\mathcal{E}$

$\boldsymbol{v}$: sample space variable corresponding to $\boldsymbol{u}$

$\boldsymbol{W}$: independent vector valued Wiener process in the physical space

W_k : rate of reaction k

$w^{(n)}$: particle weight

$\boldsymbol{W}^u$: independent vector-valued Wiener process in the velocity space

W^ω : independent Wiener process in the frequency space

$\boldsymbol{x}$: position vector

x : axial (streamwise) direction

X_α : mole fraction of species α

y, z : lateral directions

Y_α : mass fraction of species α

Greek

γ : specific heat ratio

γ : thermal or mass diffusivity

γ_t : subgrid diffusivity

δ : Dirac delta function

δ_{ij} : Kronecker delta

Δ_E : ensemble domain size

Δ_L : filter width

$\Delta_{l'}$: secondary filter size used in MKEV model

Δm : mass of a particle with unit weight

Δx : FD grid spacing along x

Δy : FD grid spacing along y

Δz : FD grid spacing along z

ζ : fine-grained density

θ : sample space variable corresponding to ω

μ : dynamic viscosity

$\nu'_{\alpha k}$: the stoichiometric coefficients of reaction k in forward direction

$\nu''_{\alpha k}$: the stoichiometric coefficients of reaction k in backward direction

ν_t : subgrid viscosity

ξ : random number with normal distribution

ρ : density

$\langle\rho\rangle^{\mathrm{MC}}$: MC density defined in Eq. (3.33)

τ_{ij} : viscous stress tensor

ϕ : fuel/air equivalence ratio

$\boldsymbol{\phi}$: scalar (mass fractions and enthalpy) vector

$\boldsymbol{\psi}$: sample space variable corresponding to $\boldsymbol{\phi}$

Ω : conditional Favré averaged turbulent frequency

ω : turbulent frequency

Ω_m : frequency of SGS mixing

Superscripts

q^+ : Lagrangian variable

q' : fluctuating component

q'' : Favré fluctuating component

$q^{(n)}$: n-th particle or n-th realization

Subscripts

α : scalar index

i : dimensional index

k : reaction index

q_{ref} : reference value of the quantity q

Symbols

$\overline{Q}$: time average

$\langle R \,|\, \boldsymbol{v}, \boldsymbol{\psi}\rangle$: mean of R conditional on $\boldsymbol{u} = \boldsymbol{v}$ and $\boldsymbol{\phi} = \boldsymbol{\psi}$

$\langle q\rangle$: ensemble average

$\widetilde{q}$: Favré mean

$\langle Q\rangle_l$: filtered quantity Q with the filter width of Δ_L (Eq. (3.6))

$\langle Q\rangle_L$: Favré filter

$\langle q\rangle_{l'}$: filtered quantity Q with the filter width of $\Delta_{l'}$

$\langle Q \,|\, \boldsymbol{\psi}\rangle_l$: filtered value of Q conditional on $\boldsymbol{\phi} = \boldsymbol{\psi}$

Abbreviations

DNS : direct numerical simulation

FD : finite difference

FDF : filtered density function

FV : finite volume

GB : 10^9 bytes

GFLOP : 10^9 floating point operations

GTC : gas turbine combustion

LES : large eddy simulation

LHS : left-hand-side

LMSE : linear mean square estimation

LP : lean premixed

LPC : lean premixed combustion

MC : Monte-Carlo

MKEV : modified kinetic energy viscosity

ODE : ordinary differential equation

PaSR : partially stirred reactor

PDF : probability density function

PSR : perfectly stirred reactor

RANS : Reynolds-averaged Navier Stokes

RHS : right-hand-side

SDE : stochastic differential equation

SFMDF : scalar filtered mass density function

SGS : subgrid scale

SLM : simplified Langevin model

ACKNOWLEDGMENTS

I am sincerely grateful to my advisor Professor Peyman Givi for his support, patience and guidance throughout the course of my graduate studies. I am also indebted to Dr. Peter A. Strakey of the National Energy Technology Laboratory (NETL) for serving as my second advisor. I would like to thank the members of my doctoral committee, Professors Minking K. Chyu, Giovanni P. Galdi and William J. Layton. I am especially indebted to Professor Layton for introducing me to Professor Givi. Throughout my studies, I had the privilege and the honor to interact and collaborate closely with several outstanding researchers including Dr. Kent H. Castleton and Dr. Geo A. Richards of NETL, and Professor İsmail Çelik and Dr. Jaggu Nanduri of the West Virginia University. I would also like to acknowledge the Combustion Group at the Cornell University headed by Professor Stephen B. Pope. They gracefully provided the computational codes which I used in some of the simulations in Chapter 2 of this Dissertation.

I am indebted to some very brilliant individuals, my dear colleagues and friends at the Computational Transport Phenomena Laboratory at the University of Pittsburgh, (in alphabetical order) Dr. Tomasz G. Drozda, Mr. Mahdi Mohebbi, Mr. Mehdi B. Nik, Mr. Patrick H. Pisciuneri, and Dr. Reza H. Sheikhi. They made this endeavor rewarding and crafted it into fun and games.

My deepest gratitude goes to two wonderful women in my life: My mother Nevin Ferruh and my wife Yonca Karakılıç Yılmaz. My mother has spent all her life to make sure her only child gets the best possible education, and has the opportunity for success. My wife's presence and support (in every imaginable way) have been the key element in accomplishing this work. I am indebted to them for their endless patience and love.

This research is sponsored by the Department of Energy, the National Energy Technology Laboratory under RDS Contract DE-AC26-04NT41817. Dr. Strakey is the Technical Monitor and Program Manager of this Contract. Computational resources are provided by the Pittsburgh Supercomputing Center (PSC) under TeraGrid Grant CTS070048, and the Swanson School of Engineering Computational Support Team at the University of Pittsburgh.

1.0 INTRODUCTION

Research into optimization of power generation systems for advanced energy and emissions performance has become increasingly important in the last two decades largely due to the increasing regulation of NO_x and SO_x emissions, along with other greenhouse gases such as CO_2.[1] Microturbine generation systems are on the forefront of this research due to the promise of "high-efficiency, ultra-clean" systems that can be used to produce electrical energy as well as thermal energy in co-generation applications. Specific objectives of optimizing microturbines include fuel flexibility with the ability to use multiple fuels such as diesel, ethanol, landfill gas and biofuels along with natural gas, and a total NO_x emission typically less than 7 ppm for natural gas. The efficiency and emissions of microturbines rely on the use of lean premixed combustion (LPC) techniques, performance issues of which are widely known to be a function of the fuel composition. Even the seasonal variability in the composition of natural gas, which is the primary fuel of choice, may alter the emission characteristics of the combustor by changing the combustion process and chemical kinetics.[2] Some recent experimental studies[3–5] have tackled the issue of fuel variability on gas turbine combustion by tabulating the emissions for a variety of fuel compositions. Another promising area of low-emission gas turbine combustion (GTC) is the use of hydrogen enriched gaseous fuels. Some recent experimental studies[6–9] have identified the advantages of hydrogen enriched fuels in lowering emissions.

There is a continuing need to develop and implement advanced computational tools for modeling and prediction of turbulent combustion for a wide range of mixing, fuel compositions and flow configurations. Reliable and flexible computational modeling is the key in achieving the objectives of modern gas-turbine design. Direct numerical simulation (DNS), Reynolds-averaged Navier-Stokes (RANS) and large eddy simulation (LES) are widely con-

sidered as three principal approaches in computational turbulent combustion.[10] DNS consists of solving the transport equations of fluid flow and resolving all of the scales of motion. In RANS, the transport equations are averaged over realizations, and the mean transport equations are solved. In LES, the spatially filtered equations of motion are considered, solution of which portrays the large scale motion. DNS provides a very accurate, model-free representation of the unsteady evolution of turbulent flows. However, applications are limited by the computational power.[11–13] RANS is the most popular approach for engineering applications.[14] LES has been the subject of much modern research and is increasingly becoming more popular.[15]

Turbulence-chemistry interactions require modeling in both RANS and LES.[11] The probabilistic approach has proven effective in this regard.[11,15–17] This approach follows from the definition of the *fine-grained density function*.[18] In RANS, the ensemble average of the fine-grained density function is considered, and is termed the *probability density function* (PDF).[19] In LES, the spatially filtered fine-grained density is termed the *filtered density function* (FDF).[11,15,17] The primary advantages of probability methods are: (i) they provide closed-form representation of chemical source terms, and (ii) they are applicable to both premixed and non-premixed flames.[15,20,21]

The RANS/PDF methods have been popular since 1970's.[22–24] Development of the Lagrangian Monte Carlo particle methods[20] has enabled PDF calculations to be conducted of a variety of flame configurations.[14,25–43] Most of the progress in LES/FDF has occurred within the past decade, but the methodology is rapidly becoming very popular.[38,44] Examples are contributions in its basic implementation,[45–55] fine-tuning of its sub-closures,[56,57] and its validation via laboratory experiments.[58–61] The LES/FDF is finding its way into commercial codes[62,63] and has been the subject of detailed discussions in several textbooks.[16,21,64,65] Givi[15] provides a comprehensive review of the state of progress in LES/FDF.

1.1 OBJECTIVE AND SCOPE

The objective of this Dissertation is to implement both RANS/PDF and LES/FDF methodologies for prediction of turbulent premixed flames. The joint velocity-scalar-frequency PDF is formulated for RANS predictions of a lean-premixed bluff-body stabilized methane flame.[66,67] The scalar FDF is employed for LES of a Bunsen burner.[68] In Chapter 2, the results of RANS/PDF predictions are presented, whereas Chapter 3 contains the results via LES/FDF. Chapter 4 provides a concise summary along with some suggestions for future research.

2.0 RANS/PDF PREDICTION

In RANS, the ensemble averaged forms of the transport equations of the chemically reacting flow are considered.[69] These equations require closures for the convection and chemical reaction source terms. Compared to conventional turbulence models,[16] the probability density function (PDF) method offers the advantage of accounting for convection and reaction in closed forms.[20] This has proven to be very useful for prediction of complex turbulent reacting flows.[14,25] The two most widely used PDF methods in RANS are the scalar PDF and the velocity-scalar-frequency PDF methods.[16] In the former, a model is required for the turbulent transport. In the latter, the convective transport is in a closed form.

PDF methods are appropriate for prediction of premixed, partially premixed, and non-premixed flames.[14,21,70] Raman *et al.*[71] and Lindstedt *et al.*[72] employed scalar PDF in RANS prediction of the Sandia piloted flames.[73] These flames were also investigated by Xu and Pope,[32] Tang *et al.*,[74] and Wang and Pope[75] using the joint velocity-scalar-frequency PDF. The non-premixed bluff-body stabilized flame[76] has been investigated by Muradoglu *et al.*[33] using scalar PDF, and by Liu *et al.*[37] using the joint velocity-scalar-frequency PDF. Cao *et al.*[36] employed velocity-scalar-frequency PDF for prediction of partially premixed lifted H_2/O_2 flames. Masri *et al.*[77] employed scalar PDF for simulation of a strongly swirling bluff body stabilized non-premixed flame. Applications to premixed and lean premixed flames are somewhat limited. Cannon *et al.*[30] and Vicente *et al.*[35] employed scalar PDF for simulation of a lean premixed bluff body flame. Lindstedt and Vaos[40] employed the same methodology for simulation of the Bunsen burner.

The present work provides the first application of the joint velocity-scalar-frequency for RANS prediction of a lean premixed turbulent flame. The bluff-body stabilized lean premixed (LP) methane-air flame is considered. This configuration has been the subject of

several previous experiments and computational investigations. Pan[66] studied the effects of the stabilizer geometry and provided measurements of the velocity and the temperature fields under several lean-stoichiometric conditions. Nandula *et al.*[67] provided non-intrusive measurements of temperature, major and minor species mole fractions, including the pollutants CO and NO. Cannon *et al.*[30] and Brewster *et al.*[70] employed the velocity-composition PDF coupled with the $k-\epsilon$ turbulence model in RANS simulation of the bluff-body LP flame. Fueyo *et al.*[78] employed the composition PDF for a comparative study of alternative reduced-chemistry mechanisms for prediction of the LP flame. Vicente *et al.*[35] used the same model to investigate the effects of mixing. Nanduri *et al.*[79] compared the predicted results via various RANS based models in the commercial software FLUENT[80] with those presented in this Dissertation.

2.1 FORMULATION

The hydrodynamic and thermochemical properties of reacting system are characterized by the velocity, enthalpy, pressure and mass fractions of each chemically reacting species. Space ($\boldsymbol{x} \equiv x_i, i = 1, 2, 3$) and time ($t$) variations of these quantities satisfy the following compressible form of the continuity, momentum, enthalpy and species mass conservation equations, under the assumptions of low Mach number, ideal gas, negligible viscous dissipation:[69]

$$\frac{\partial \rho}{\partial t} + \frac{\partial \rho u_i}{\partial x_i} = 0 \tag{2.1a}$$

$$\frac{\partial \rho u_i}{\partial t} + \frac{\partial \rho u_i u_j}{\partial x_j} = -\frac{\partial p}{\partial x_i} + \frac{\partial \tau_{ij}}{\partial x_j} \tag{2.1b}$$

$$\frac{\partial \rho \phi_\alpha}{\partial t} + \frac{\partial \rho \phi_\alpha u_j}{\partial x_j} = -\frac{\partial J_i^\alpha}{\partial x_i} + \rho S_\alpha \tag{2.1c}$$

$$p = \rho R T. \tag{2.1d}$$

where $\boldsymbol{u} = u_i$, $i = 1, 2, 3$ is the velocity vector, p is the pressure, ρ is the flow density, $\phi_\alpha = Y_\alpha$ for $\alpha = 1, 2, \ldots, N_s$ are the species mass fractions for N_s species, and $\phi_{Ns+1} = h$ is the enthalpy representing thermodynamic and chemical (but not mechanical) energy. $R = R^0 \sum_{\alpha=1}^{N_s} Y_\alpha / \mathcal{M}_\alpha$ is the mixture gas constant with the universal gas constant R^0 and molar

mass of species $\mathcal{M}_\alpha$, and T is the gas temperature. For a Newtonian fluid with zero bulk velocity and Fickian diffusion, the viscous stress tensor τ_{ij}, and the scalar (mass and heat) flux J_i^α are given by,

$$\tau_{ij} = \mu\left(\frac{\partial u_i}{\partial x_j} + \frac{\partial u_j}{\partial x_i} - \frac{2}{3}\frac{\partial u_k}{\partial x_k}\delta_{ij}\right) \tag{2.2a}$$

$$J_i^\alpha = -\gamma\frac{\partial \phi_\alpha}{\partial x_i}, \tag{2.2b}$$

where, μ is the dynamic viscosity and $\gamma = \rho\Gamma$ denotes the thermal and the mass diffusivity coefficients for all species (assuming unity thermal to mass diffusivity ratio, *i.e.*, Lewis number $\mathrm{Le} = 1$).

The chemical source terms, S_α for $\alpha = 1, \ldots, N_s$, are functions of the composition variables $\boldsymbol{\phi} = [Y_1, Y_2, \ldots, Y_{Ns}, h]$ and are determined by the gas-phase reaction mechanisms. Most of the reaction rate data for pure hydrocarbon fuels up to n-heptane and iso-octane are very detailed.[81] For example, the GRI-Mech 3.0 mechanism[82] for methane oxidation accounts for 325 reactions among 53 species. The rate of reaction k in a mechanism containing r chemical reactions is

$$W_k \equiv k_{fk}\prod_{\alpha=1}^{N_s}\left(\frac{\rho Y_\alpha}{\mathcal{M}_\alpha}\right)^{\nu'_{\alpha k}} - k_{bk}\prod_{\alpha=1}^{N_s}\left(\frac{\rho Y_\alpha}{\mathcal{M}_\alpha}\right)^{\nu''_{\alpha k}}, \tag{2.3}$$

where k_{fk} and k_{bk} are the rate coefficients of the forward and backward reaction, respectively. In general, they are temperature dependent and may also depend on pressure. The exponents $\nu'_{\alpha k}$ and $\nu''_{\alpha k}$ are the stoichiometric coefficients of reaction k in forward and backward direction, respectively. The mass production rate of species α per unit volume and unit time is the sum over all reactions in the mechanism:

$$\rho S_\alpha = \mathcal{M}_\alpha\sum_{k=1}^{r}\nu_{\alpha k}W_k \tag{2.4}$$

where $\nu_{\alpha k} = \nu''_{\alpha k} - \nu'_{\alpha k}$. The sum over all source terms vanishes:

$$\sum_{\alpha=1}^{N_s}\rho S_\alpha = 0 \tag{2.5}$$

Under the assumptions of negligible viscous dissipation and low compressibility, the source term for the enthalpy, S_{Ns+1}, represents the effects of radiation. For small laboratory flames heat loss by radiation is usually a negligible fraction of the total heat flow; therefore $S_{Ns+1} \approx 0$.

Equations (2.1) and (2.2) form a closed set. Analytical solutions have only been obtained for simple laminar flows. In general, numerical solution via DNS is the only way for turbulent flows, but this is restricted by computer power to very low Reynolds number flows. In RANS, *ensemble (realization) averaging* operation is used:

$$\langle q(\boldsymbol{x},t)\rangle \equiv \lim_{N\to\infty}\frac{1}{N}\sum_{n=1}^{N} q^{(n)}(\boldsymbol{x},t). \tag{2.6}$$

where $q^{(n)}(\boldsymbol{x},t)$ is the value of a transport variable q at $\boldsymbol{x}$ and t in the n-th of N total realizations. The fluctuations are defined as

$$\begin{aligned} q'(\boldsymbol{x},t) &\equiv q(\boldsymbol{x},t) - \langle q(\boldsymbol{x},t)\rangle, & (2.7)\\ \langle q'\rangle &= 0. & (2.8)\end{aligned}$$

A more convenient form of the equations are obtained by the density weighted or Favré averaging:[83]

$$\begin{aligned} \widetilde{q} &\equiv \frac{\langle \rho q\rangle}{\langle\rho\rangle} & (2.9)\\ q'' &\equiv q - \widetilde{q} & (2.10)\\ \widetilde{q''} &= 0,\ \langle q''\rangle \neq 0. & (2.11)\end{aligned}$$

The Favré averaged form of the transport equations are

$$\begin{aligned} \frac{\partial\langle\rho\rangle}{\partial t} + \frac{\partial\langle\rho\rangle\widetilde{u}_i}{\partial x_i} &= 0 & (2.12)\\ \frac{\partial\langle\rho\rangle\widetilde{u}_i}{\partial t} + \frac{\partial\langle\rho\rangle\widetilde{u}_i\widetilde{u}_j}{\partial x_j} &= -\frac{\partial\langle p\rangle}{\partial x_i} + \frac{\partial\langle\tau_{ij}\rangle}{\partial x_j} - \frac{\partial}{\partial x_j}\left(\langle\rho\rangle\widetilde{u_i''u_j''}\right) & (2.13)\\ \frac{\partial\langle\rho\rangle\widetilde{\phi_\alpha}}{\partial t} + \frac{\partial\langle\rho\rangle\widetilde{u}_i\widetilde{\phi_\alpha}}{\partial x_i} &= -\frac{\partial\widetilde{J_i^\alpha}}{\partial x_i} - \frac{\partial}{\partial x_i}\left(\langle\rho\rangle\widetilde{u_i''\phi_\alpha''}\right) + \langle\rho\rangle\widetilde{S_\alpha} & (2.14)\\ \langle p\rangle &= \langle\rho\rangle\widetilde{RT}, & (2.15)\end{aligned}$$

The quantities appearing in these equations are (i) the mean quantities which it is the objective to determine ($\widetilde{\boldsymbol{u}}$, $\widetilde{\boldsymbol{\phi}}$ and $\langle p \rangle$), (ii) the density weighted velocity-velocity and velocity-scalar correlations ($\widetilde{u_i'' u_j''}$ and $\widetilde{u_i'' \phi_\alpha''}$), and (iii) the density weighted average of the highly nonlinear reaction source term $\widetilde{S_\alpha}$. It is the principle aim of combustion modeling in RANS to provide closure for the terms (ii) and (iii). At the core of PDF methods lies the definition of the one-point, one-time, joint probability density function (PDF) of $\boldsymbol{u}(\boldsymbol{x}, t)$ and $\boldsymbol{\phi}(\boldsymbol{x}, t)$ at location $\boldsymbol{x}$ and time t:

$$f(\boldsymbol{v}, \boldsymbol{\psi}; \boldsymbol{x}, t) \equiv \langle \zeta [\boldsymbol{v}, \boldsymbol{u}(\boldsymbol{x}, t), \boldsymbol{\psi}, \boldsymbol{\phi}(\boldsymbol{x}, t)] \rangle \tag{2.16}$$

where $\boldsymbol{v} = [v_1, v_2, v_3]$ and $\boldsymbol{\psi} = [\psi_1, \psi_2, \ldots, \psi_{Ns+1}]$ are the sample space variables for the velocity and the composition vectors, respectively. The PDF is the ensemble average of the *fine-grained density*, ζ, defined as,[18]

$$\zeta [\boldsymbol{v}, \boldsymbol{u}(\boldsymbol{x}, t), \boldsymbol{\psi}, \boldsymbol{\phi}(\boldsymbol{x}, t)] \equiv \prod_{i=1}^{3} \prod_{\alpha=1}^{N_s+1} \delta (v_i - u_i(\boldsymbol{x}, t)) \, \delta (\psi_\alpha - \phi_\alpha(\boldsymbol{x}, t)) . \tag{2.17}$$

where δ is the Dirac delta (or unit impulse) function. In variable density flows, the density-weighted joint PDF is a useful quantity, and is defined as

$$\begin{aligned} \widetilde{f}(\boldsymbol{v}, \boldsymbol{\psi}; \boldsymbol{x}, t) &\equiv \langle \rho(\boldsymbol{\phi}(\boldsymbol{x}, t)) \, \zeta [\boldsymbol{v}, \boldsymbol{u}(\boldsymbol{x}, t), \boldsymbol{\psi}, \boldsymbol{\phi}(\boldsymbol{x}, t)] \rangle \\ &= f(\boldsymbol{v}, \boldsymbol{\psi}; \boldsymbol{x}, t) \frac{\rho(\boldsymbol{\psi})}{\langle \rho \rangle} \end{aligned} \tag{2.18}$$

For a random variable $R(\boldsymbol{x}, t)$, the Favré mean can be determined by

$$\begin{aligned} \widetilde{R} &= \int_{\boldsymbol{\psi}} \int_{\boldsymbol{v}} \langle \rho(\boldsymbol{\phi}) R \mid \boldsymbol{u} = \boldsymbol{v}, \boldsymbol{\phi} = \boldsymbol{\psi} \rangle f(\boldsymbol{v}, \boldsymbol{\psi}) / \langle \rho \rangle \, \mathrm{d}\boldsymbol{v} \mathrm{d}\boldsymbol{\psi} \\ &= \int_{\boldsymbol{\psi}} \int_{\boldsymbol{v}} \langle R \mid \boldsymbol{u} = \boldsymbol{v}, \boldsymbol{\phi} = \boldsymbol{\psi} \rangle \rho(\boldsymbol{\psi}) f(\boldsymbol{v}, \boldsymbol{\psi}) / \langle \rho \rangle \, \mathrm{d}\boldsymbol{v} \mathrm{d}\boldsymbol{\psi} \\ &= \int_{\boldsymbol{\psi}} \int_{\boldsymbol{v}} \langle R \mid \boldsymbol{u} = \boldsymbol{v}, \boldsymbol{\phi} = \boldsymbol{\psi} \rangle \widetilde{f}(\boldsymbol{v}, \boldsymbol{\psi}) \, \mathrm{d}\boldsymbol{v} \mathrm{d}\boldsymbol{\psi} \end{aligned} \tag{2.19}$$

where $\langle R \mid \boldsymbol{u} = \boldsymbol{v}, \boldsymbol{\phi} = \boldsymbol{\psi} \rangle$, or in short $\langle R \mid \boldsymbol{v}, \boldsymbol{\psi} \rangle$, denotes the expectation of R conditioned on $\boldsymbol{u} = \boldsymbol{v}$ and $\boldsymbol{\phi} = \boldsymbol{\psi}$. If R is independent of $\boldsymbol{u}$ and $\boldsymbol{\phi}$, then

$$\langle R \mid \boldsymbol{v}, \boldsymbol{\psi} \rangle = \langle R \rangle , \tag{2.20}$$

in which case f does not carry any information about R, and Eq. (2.19) is not useful. If R is completely determined by $\boldsymbol{u}$ and $\boldsymbol{\phi}$, then

$$\langle R(\boldsymbol{u},\boldsymbol{\phi}) \mid \boldsymbol{v},\boldsymbol{\psi}\rangle = R(\boldsymbol{v},\boldsymbol{\psi}) \tag{2.21}$$

and Eq. (2.19) reduces to the definition of the unconditional mean.

The significance of the PDF approach is that the reaction source and the convective transport terms are functions of $\boldsymbol{u}$ and $\boldsymbol{\phi}$ can be evaluated directly. For example, for the reaction rates

$$\widetilde{S_\alpha}(\boldsymbol{x},t) = \widetilde{\hat{S}_\alpha}(\boldsymbol{\phi}(\boldsymbol{x},t)) = \int_{\boldsymbol{\psi}}\int_{\boldsymbol{v}} \hat{S}_\alpha(\boldsymbol{\psi})\widetilde{f}(\boldsymbol{v},\boldsymbol{\psi};\boldsymbol{x},t)\,\mathrm{d}\boldsymbol{v}\mathrm{d}\boldsymbol{\psi} \tag{2.22}$$

where $\hat{S}_\alpha$ is the reaction rate as a function of composition variables. Of course, $\widetilde{f}(\boldsymbol{v},\boldsymbol{\psi};\boldsymbol{x},t)$ contains far much more information than is required – that is $\widetilde{S_\alpha}$, $\widetilde{u_i''u_j''}$ and $\widetilde{u_i''\phi_\alpha''}$.

Using the above definitions, the transport equation for $\widetilde{f}$ can be derived from the conservation equations, Eqs. (2.1):[84]

$$\begin{aligned}\frac{\partial\widetilde{f}}{\partial t}+\frac{\partial v_j\widetilde{f}}{\partial x_j} &= -\frac{\partial S_\alpha\widetilde{f}}{\partial\psi_\alpha}+\frac{\partial}{\partial v_k}\left(\left\langle\frac{1}{\rho}\frac{\partial p}{\partial x_k}\,\middle|\,\boldsymbol{v},\boldsymbol{\psi}\right\rangle\widetilde{f}\right)\\ &- \frac{\partial}{\partial v_k}\left(\left\langle\frac{1}{\rho}\frac{\partial\tau_{kj}}{\partial x_j}\,\middle|\,\boldsymbol{v},\boldsymbol{\psi}\right\rangle\widetilde{f}\right)+\frac{\partial}{\partial\psi_\alpha}\left(\left\langle\frac{1}{\rho}\frac{\partial J_j^\alpha}{\partial x_j}\,\middle|\,\boldsymbol{v},\boldsymbol{\psi}\right\rangle\widetilde{f}\right).\end{aligned} \tag{2.23}$$

The two terms on the left-hand-side (LHS) of this equation denote evolution in time and physical space due to convection, and are closed. Also closed is the first term on the RHS, which is transport in the composition space due to chemical reaction. The two terms involving conditional expectations require closures. These are the transport in velocity space due to viscous stress tensor and the pressure gradient, and the molecular transport in the composition space, respectively.

The unclosed terms in the joint PDF transport equation, Eq. (2.23), are due to the fact that $\widetilde{f}$ is a one-point, one-time statistic, and contains no length-scale information. Ievlev[85] provides a general transport equation for n-point joint PDF of velocity and scalars in which the $(n+1)$-point distribution is approximated in terms of n-point distributions.

2.2 MODELING AND SIMULATION

The closure for PDF transport equation is provided in the form of a set of *Stochastic Differential Equations* (SDEs).[86–88] All of the modeling in the PDF transport equation is via selection of the parameters of the SDEs which describe a diffusion process.[89] A deterministic description of this process is given by the corresponding Fokker-Planck equation.[90] The closure for the PDF transport equation, Eq. (2.23), is made by constructing a direct analogy to the Fokker-Planck equation.

The most comprehensive model to date is given by the joint velocity-scalar-frequency PDF model, which introduces the following SDEs:[14,21,25,27]

$$\mathrm{d}X_i^+ = u_i^+ \mathrm{d}t\,, \tag{2.24a}$$

$$\mathrm{d}u_i^+ = -\frac{1}{\langle\rho\rangle}\frac{\partial\langle p\rangle}{\partial x_i}\mathrm{d}t - \left(\frac{1}{2}+\frac{3}{4}C_0\right)\Omega(u_i^+ - \widetilde{u}_i)\mathrm{d}t + \sqrt{C_0\widetilde{k}\Omega}\,\mathrm{d}W_i^u\,, \tag{2.24b}$$

$$\mathrm{d}\phi_\alpha^+ = S_\alpha\left(\phi^+\right)\mathrm{d}t - C_\phi\Omega\left(\phi_\alpha^+ - \widetilde{\phi}_\alpha\right)\mathrm{d}t\,, \tag{2.24c}$$

$$\mathrm{d}\omega^+ = -C_3\left(\omega^+ - \widetilde{\omega}\right)\Omega\mathrm{d}t - S_\omega\Omega\omega^+\mathrm{d}t + \sqrt{2C_3C_4\widetilde{\omega}\Omega\omega^+}\mathrm{d}W^\omega\,, \tag{2.24d}$$

where $\boldsymbol{X}^+(t)$, $\boldsymbol{u}^+(t)$, $\boldsymbol{\phi}^+(t)$ and $\omega^+(t)$ denote the stochastic evolution of position, velocity vector, composition variables and turbulence frequency, respectively. The models implied by these equations are the *Simplified Langevin Model* (SLM)[16] for closure of viscous dissipation and fluctuating pressure gradient, the *linear mean-square estimation* (LMSE)[22] to account for the effects of molecular diffusion, and the modified *gamma-distribution model*[31] for turbulent frequency. In these equations, $\Omega \equiv C_\Omega \langle \rho^+\omega^+ \,|\, \omega^+ \geq \widetilde{\omega}\rangle / \langle\rho\rangle$ is the conditional Favré averaged turbulent frequency, $\widetilde{k} \equiv \widetilde{u_i''u_i''}/2$ is the turbulent kinetic energy, W terms are independent Wiener processes in the velocity (u) and frequency (ω) space, $S_\omega = C_{\omega 2} - C_{\omega 1}P/\widetilde{k}\Omega$ is the turbulence source term where $P \equiv -\widetilde{u_i''u_j''}\frac{\partial\widetilde{u}_i}{\partial x_j}$ is the turbulent production, and the coefficients $C_0, C_\Omega, C_{\omega 1}, C_{\omega 2}, C_3, C_4$ and C_ϕ are the model constants. The Fokker-Planck corresponding to these SDEs gives the following modeled PDF transport equation:

$$
\begin{aligned}
\frac{1}{\langle\rho\rangle}\frac{\partial\langle\rho\rangle\widetilde{f}}{\partial t} &= -\frac{v_i}{\langle\rho\rangle}\frac{\partial\langle\rho\rangle\widetilde{f}}{\partial x_i}+\frac{1}{\langle\rho\rangle}\frac{\partial\langle p\rangle}{\partial x_i}\frac{\partial\widetilde{f}}{\partial v_i} \\
&\quad+\left(\frac{1}{2}+\frac{3}{4}C_0\right)\Omega\frac{\partial}{\partial v_i}[\widetilde{f}(v_i-\widetilde{u_i})]+\frac{1}{2}C_0\widetilde{k}\Omega\frac{\partial^2\widetilde{f}}{\partial v_i\partial v_i} \\
&\quad+\Omega\frac{\partial}{\partial\theta}(\widetilde{f}\theta S_\omega)+C_3\Omega\frac{\partial}{\partial\theta}[\widetilde{f}(\theta-\widetilde{\omega})]+C_3C_4\Omega\widetilde{\omega}\frac{\partial^2\widetilde{f}\theta}{\partial\theta^2} \\
&\quad-\frac{\partial\widetilde{f}S_\alpha}{\partial\psi_\alpha}+\frac{1}{2}C_\phi\Omega\frac{\partial}{\partial\psi_\alpha}[\widetilde{f}(\psi_\alpha-\widetilde{\phi}_\alpha)]. \qquad (2.25)
\end{aligned}
$$

From the computational standpoint, solution of the SDEs is significantly easier than that of the modeled PDF transport Eq. (2.25). The most effective way is via the Monte Carlo (MC) method. These methods have been used for simulation of a wide variety of stochastic problems[91] and have benefited significantly from modern developments in numerical methods for SDEs.[92] In the MC method, the PDF is represented by an ensemble of stochastic particles. These particles carry information pertaining to their positions $\boldsymbol{X}^{(n)}(t)$, velocities $u^{(n)}(t)$, scalar values $\boldsymbol{\phi}^{(n)}(t)$ and turbulence frequency $\omega^{(n)}(t)$, which are initialized in accord with the initial mean fields. This information is updated via temporal integration of the modeled SDEs given in Eq. (2.24). Several mean fields are required in order to carry out the integration. In a sole MC simulation, these fields are extracted directly from the particle properties. However, it has been shown that such simulations suffer from deficiencies caused by statistical fluctuations in the particle mean fields.[93,94] To overcome these deficiencies, a hybrid methodology is devised by Jaberi *et al.*[95] in which a set of deterministic transport equations are solved along with MC simulation of SDEs. These are the mean conservation equations obtained by integration of the model PDF transport Eq. (2.25), and are solved by traditional finite difference (FD) or finite volume (FV) techniques:

$$
\begin{aligned}
\frac{\partial\langle\rho\rangle}{\partial t}+\frac{\partial\langle\rho\rangle\widetilde{u_i}}{\partial x_i} &= 0, \qquad (2.26a) \\
\frac{\partial\langle\rho\rangle\widetilde{u_i}}{\partial t}+\frac{\partial\langle\rho\rangle\widetilde{u_i}\widetilde{u_j}}{\partial x_j}+\frac{\partial\langle p\rangle}{\partial x_i} &= -\frac{\partial}{\partial x_j}\left(\langle\rho\rangle\widetilde{u_i''u_j''}\right), \qquad (2.26b) \\
\frac{\partial\langle\rho\rangle\widetilde{h}_s}{\partial t}+\frac{\partial\langle\rho\rangle\widetilde{h}_s\widetilde{u_i}}{\partial x_i} &= -\frac{\partial\langle\rho\rangle\widetilde{u_i''h_s''}}{\partial x_i}+\langle\rho\rangle\widetilde{\dot{q}} \qquad (2.26c)
\end{aligned}
$$

where $h_s \equiv (\gamma/(\gamma-1))p/\rho$ is the equivalent enthalpy with $\gamma = c_p/c_v$ being the ratio of specific heats, and $\dot{q} = \sum_\alpha \frac{\partial h_s}{\partial \phi_\alpha} S_\alpha$ is the heat source due to chemical reaction. All the terms appearing on the right-hand side are obtained from the MC simulations as statistical estimations.

To understand the operational procedure, the elements of the computation as utilized in our simulations are shown in Fig. 1. The computational domain is discretized on a number of fixed grid points with spatial spacing Δ. The MC particles are distributed randomly and are free to move anywhere within the domain as governed by Eq. (2.24). This transport is Lagrangian, and thus the solution is free of mesh constraints typical of FD or FV simulations. Statistical information required in Eqs. (2.26) at any grid point is obtained by considering an ensemble of N_E computational particles residing within an ensemble domain of side length Δ_E centered around the grid point. For reliable statistics with minimal numerical dispersion, it is desirable to minimize the size of ensemble domain and maximize the number of MC particles.[20] In this way, the ensemble statistics tend to the desired Favré averaged values. Some of the coefficients of the SDEs in Eq. (2.24) are in turn obtained by interpolation to the particle locations.

With the hybrid method employed here, some of the quantities are obtained by MC, some by FV, and some by both. In particular, since the deterministic equations are introduced only to overcome the problem associated with statistical errors of the stand-alone MC simulation, all of the mean quantities obtained from FV solutions can be extracted from the particle fields. At the level of governing equations, Eq. (2.24) and Eq. (2.26) are consistent. However with certain schemes, the solutions may not be identical due to the accumulation of numerical errors. Here, in RANS/PDF simulations a time-inaccurate, semi-implicit FV scheme is employed in order to achieve fast steady state solutions. The SDEs are integrated with a first order accurate explicit Euler-Maruyamma scheme.[92] In order to enforce consistency, artificial correction of particle fields are required. The correction algorithm proposed by Muradoglu *et al.*[96] is employed here for this purpose.

2.3 FLAME CONFIGURATION AND MODEL PARAMETERS

The schematic diagram of the bluff-body flow configuration as considered in the experiments of Pan[66] and Nandula *et al.*[67] is given in Fig. 2. Methane and air under lean premixed conditions with equivalence ratio $\phi = 0.586$ is fed through an annular ring. A conical bluff body stabilizes the flame within the recirculation zone that extends about one diameter downstream. The recirculation zone anchors the flame by trapping the hot products, which then flow downstream and exit into the atmosphere. Transient eddies issued at the bluff body base enhance mixing between the reactants and the products. The Reynolds number based on inlet gas velocity and bluff body diameter is 66,000. The experiments[66,67] provide data in the form of radial profiles near the recirculation zone at selected axial locations (shown in Fig. 2) above the bluff-body.

In our simulations, the combustor chamber is represented by a 2D axisymmetric domain starting at the bluff body base and extends to 5.6 diameters downstream. The two lateral boundaries coincide with the chamber wall and the symmetry axis. The inlet velocity and Reynolds stress profiles are imposed based on cold flow simulations (obtained via the FLUENT[80]) which also include upstream of the conical bluff-body. Perfectly mixed conditions for fuel and air are assumed at the inlet. Adiabatic conditions are imposed at the bluff-body base and at the walls. The domain is discretized into 140×70 non-uniform structured FV cells with stretching applied at the shear layer and near the walls. The mesh size and stretching is based on the grid independence tests made for cold flow (see Figs. 3 and 6). The ensemble domain size is equal to the FV cell size. About 100 Monte-Carlo particles per ensemble domain are used. The PDF model constants are those suggested in previous work,[37] and are shown in Table 1.

A systematically reduced chemical mechanism with 5 global steps, 9 solved and 38 steady state species is used for methane oxidation. This mechanism is developed by Mallampalli *et al.*[97] and is based on the Gas Research Institute (GRI) 2.11 mechanism.[98] The species considered are CH_4, O_2, H_2O, CO_2, N_2, OH, NO, H_2 and CO. The reduced system is

Table 1: PDF model constants used in bluff-body simulations

C_0	C_Ω	$C_{\omega 1}$	$C_{\omega 2}$	C_3	C_4	C_ϕ
2.1	0.6893	0.56	0.9	1.0	0.25	1.5

described by the following global reaction steps:

$$\begin{aligned}
&\text{R1}: && 3H_2 + O_2 + CO_2 \Longleftrightarrow 3H_2O + CO \\
&\text{R2}: && H_2 + 2OH \Longleftrightarrow 2H_2O \\
&\text{R3}: && 3H_2 + CO \Longleftrightarrow H_2O + CH_4 \\
&\text{R4}: && H_2 + CO_2 \Longleftrightarrow H_2O + CO \\
&\text{R5}: && 3H_2 + CO_2 + 2NO \Longleftrightarrow 3H_2O + CO + N_2
\end{aligned} \tag{2.27}$$

Mallampalli *et al.*[97] evaluated this mechanism in a perfectly stirred reactor (PSR), and in laminar premixed flames. Their calculated temperature, CO and NO concentrations are shown to be within 2% of the full mechanism predictions at lean conditions. They also take into account the effects of molecular mixing in a partially stirred reactor (PaSR) model, and observe that the mechanism accurately describes the evolution of the mean and the rms temperature, CO and NO concentration over a wide range of the mixing frequency.

2.4 RESULTS

The capability of the method to predict the hydrodynamics is demonstrated by comparison with the cold flow measurements of Pan.[66] Figure 3 shows the predicted radial profiles of the mean axial and radial velocities compared with the experimental measurements. The agreement is good, in particular the extent of the recirculation zone is captured well. This is further ascertained via comparison of the 2D axial velocity contours shown in Fig. 4. It is observed that the predicted stagnation boundary (identified with the thick black contour) is similar to that in the experiment. Closer to the axis, the magnitude of the axial velocity

is underpredicted. This is attributed to the simplified Langevin model employed in model SDEs, which yields the Rotta's closure[99] for the pressure-strain correlation. This model does not properly account for the anisotropies of the highly recirculating flow in this region. Moreover, the measurements for the magnitude of the radial velocity are somewhat sensitive and more prone to experimental errors.[66] As shown by the radial profiles in Fig. 3 and 2D contours in Fig. 5, the predictions are in good agreements with data at all axial locations. However, the magnitude is overpredicted in the upstream, and is underpredicted downstream. Figure 6 shows the radial profiles of the rms velocity components. Despite some statistical errors, the overall agreement with experimental data is good.

Figure 7 shows the predicted radial profiles of the mean axial and the radial velocities. The location of the shear layer is portrayed well by the model. Also captured is the decrease of the axial velocity along the streamwise direction up to $x/d = 0.6$, and the increase from 0.6 to 1.0. The discrepancies in predictions of the centerline axial velocity are similar to those reported by Cannon *et al.*[30] and Vicente *et al.*[35] who employed RANS models without proper consideration of the recirculation effects.

Figure 9 shows the radial profiles of the mean temperature. The recirculation zone behind the bluff-body allows hot combustion products to mix and react with the incoming fuel-air mixture and, thus stabilizes the flame. The profiles for temperature reveal the location of cold reactants and hot products within the combustion chamber. The predicted mean temperature in the recirculation zone ($r/d < 0.5$) is in agreement with the data, except in the upstream region the values are overpredicted by ≈100K. This is due to the neglect of heat losses due to radiation and convection on the bluff body surface. In fact, the predicted value is closer to the adiabatic equilibrium temperature (≈1640K). The predicted locations of the sharp temperature gradients where hot and cold gases mix, are in good agreement with data, particularly at $x/d = 0.3, 0.6$ and 0.8. The location of the gradient at $x/d = 1.0$ is underpredicted by about $0.1d$. This indicates either an insufficient heat-release due to the reduced chemical mechanism, or an over-prediction of mixing at this location. Also shown in Fig. 9 are the radial profiles of the mean N_2 mole fractions. The reduced chemistry model accounts for only one other N-containing species, NO, and that is a minor species which exists only in trace amounts. All other N-containing species are lumped into the N_2

concentration. Therefore, the predicted profiles are more or less flat in the chamber, whereas the experimental profiles show variations, particularly close to the flame surface.

The radial profiles of CH_4 and CO_2 mole fractions are shown in Fig. 10. The locations of hot product and cold reactants are revealed by these profiles. The predictions are in excellent agreements with data at all axial locations except at $x/d = 1.0$ where the shift in the gradient is similar to that observed in the temperature profiles. This indicates that the model underpredicts the CH_4 consumption at the end of the recirculation zone, and may be attributed to an excess mixing rate. The radial profiles of H_2O and O_2 mole fractions are given in Fig. 11. The predictions are in good agreements with the measurements. As observed for the temperature and for CH_4, the predicted values of the reactants are higher than those measured experimentally at downstream of the recirculation region. The differences of the calculated and the measured values of H_2O mole fractions in this region are not as pronounced. This indicates that H_2O approaches the equilibrium value at a faster rate than does CO_2. Overall, the major species predictions are in good agreements with measurements in the recirculation zone at all axial locations, and in the shear layer region.

The radial profiles of mole fractions of the minor species NO and OH are shown in Fig. 12. The NO profiles indicate the location of reacted or partially reacted gas experiences long reaction times to form prompt, N_2O-intermediate, and thermal NO. The reduced mechanism accounts for these reasonably well. The OH profiles are overpredicted by a factor of 10 at the lowest axial location $x/d = 0.1$, but the predictions are in a better agreement with data at $x/d = 1.0$. The measured value of OH mole fraction at the lower recirculation region is close to the equilibrium value of 200 ppm, and much higher in the upstream region. The superequilibrium behavior portrayed by the model may be due to two factors: (i) the reduced mechanism does not account for OH in an accurate manner, which is also indicated in previous PSR calculations.[97] (ii) The production of OH is very sensitive to temperature, and slight overprediction of temperature leads to excess amount of OH. Temperature is indeed overpredicted in the downstream region as shown in Fig. 9.

The radial profiles of the minor species CO and H_2 are shown in Fig. 13. The measured data for CO reveal the location of the quenched product zone. The CO mole fractions peak at the mixing layer, indicating reaction quenching at the region where the hot products meet

the cold stream. At the opposite end, closer to the centerline, and near the bluff body base, the CO oxidizes to form CO_2. The measured values in the chamber are much higher that the equilibrium value of 7 ppm. This is captured by the model reasonably well, except at $x/d = 1.0$, where the values are underpredicted especially near the shear layer. The H_2 profiles follow similar trend as CO, and predictions are in good agreements with data.

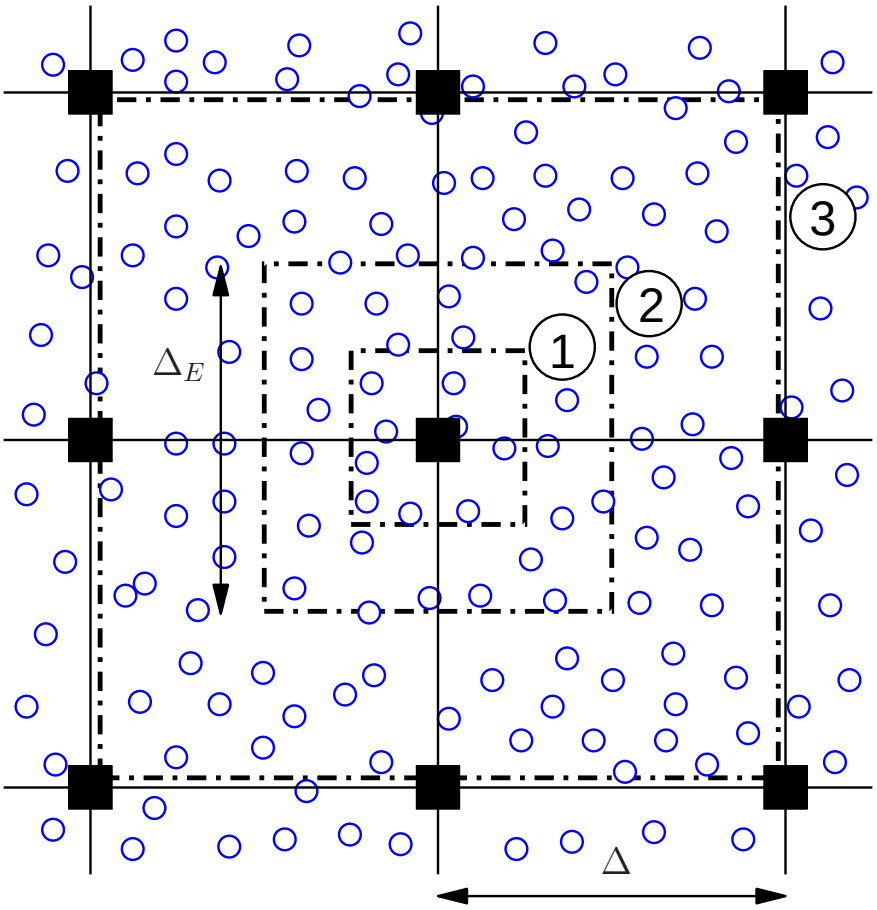

Figure 1: Element of computation as used in hybrid simulations. Solid squares denote grid locations of the FD or FV mesh, and the circles denote the MC particles. Also shown are three different ensemble domains.

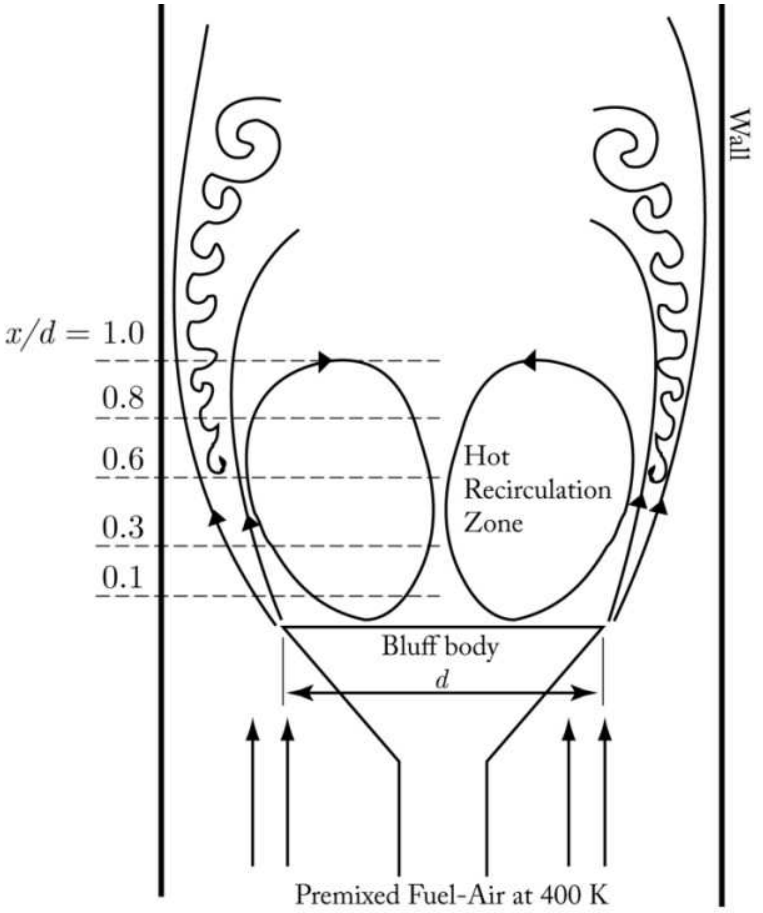

Figure 2: Schematic diagram of the bluff body configuration.[66] The x/d axial locations where experimental measurements are made are marked.

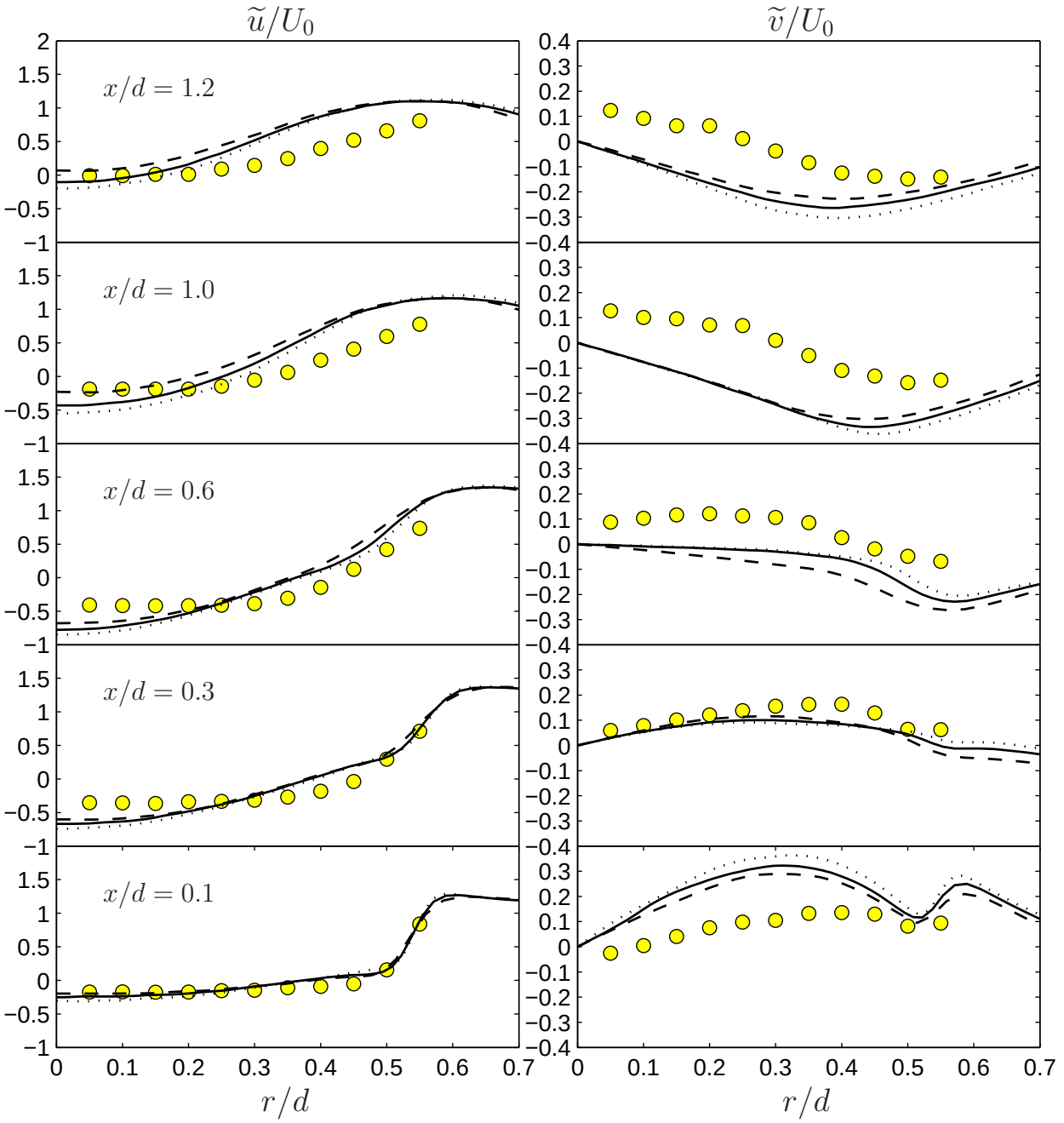

Figure 3: Bluff-body, cold flow: The radial profiles of the mean axial and radial velocity components on three FV-meshes: – – 80×40, — 140×70, and ···· 180×100, where $n_x \times n_r$ indicate number of FV cells in the axial and the radial directions. ○ Experiment.[66]

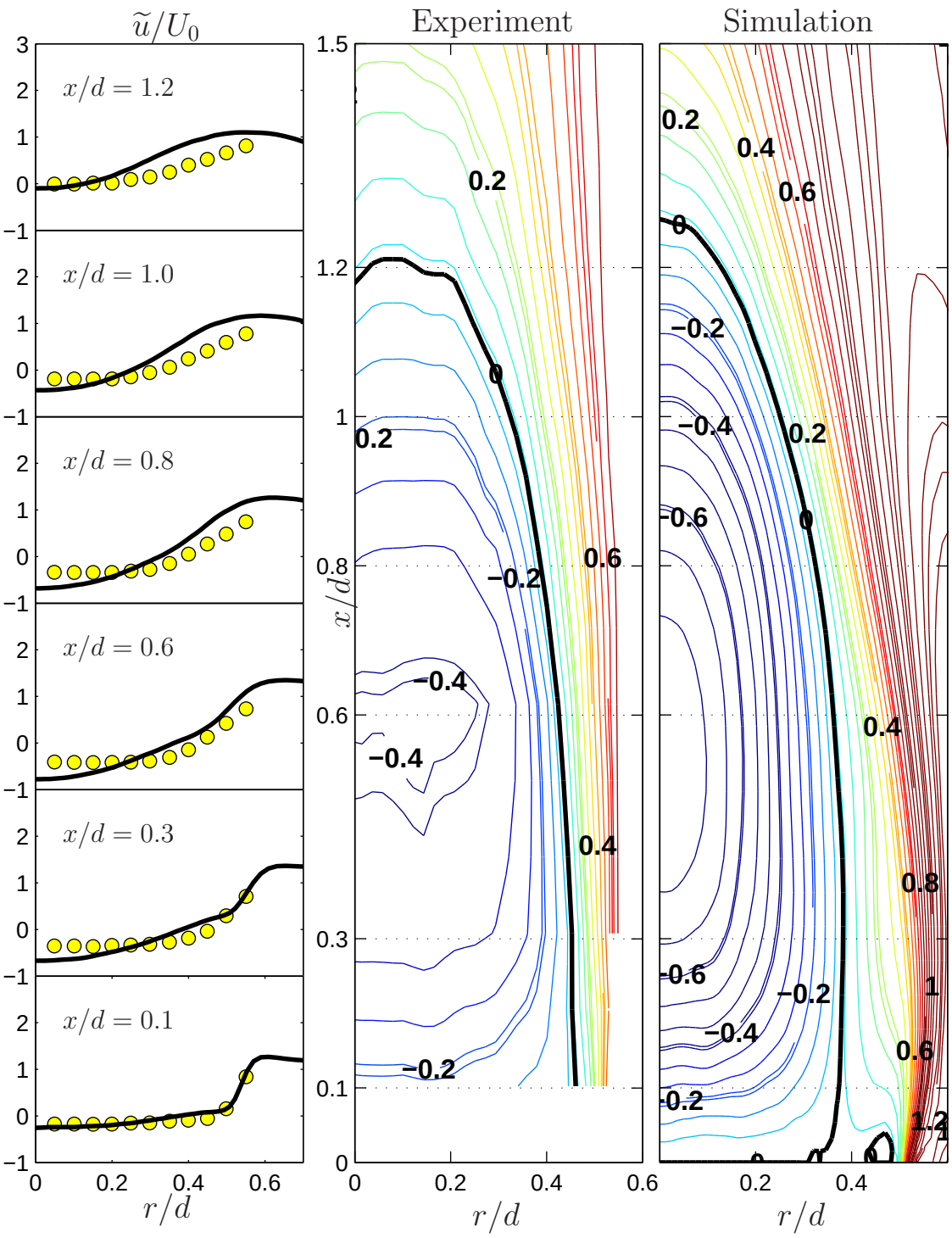

Figure 4: Bluff-body, cold flow: 2D axisymmetric contours of the mean axial velocity. The radial profiles are shown on the left at several axial locations which are indicated by dotted lines (····) over the contour plots. — RANS/PDF calculations, ○ Experiment.[66]

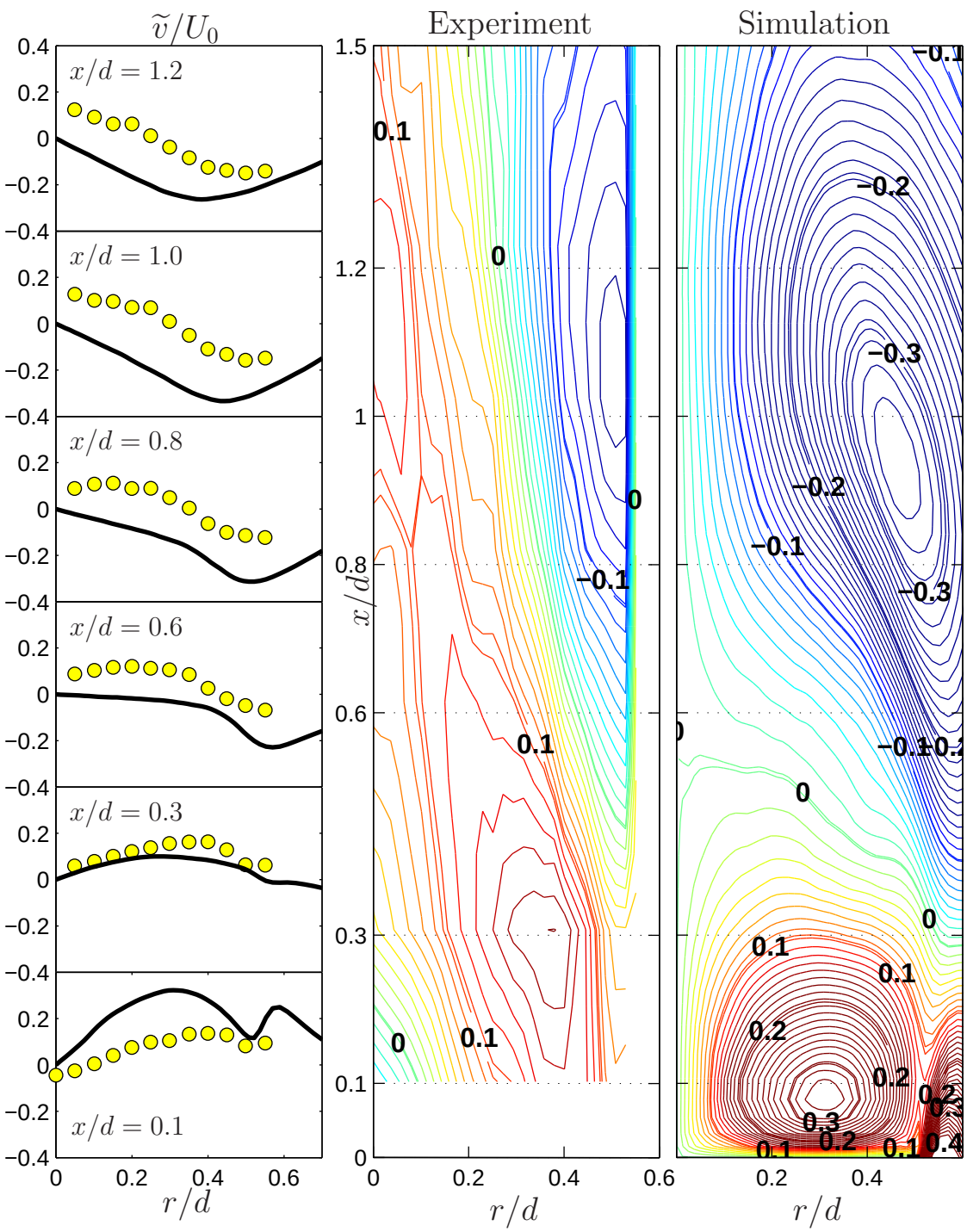

Figure 5: Bluff-body, cold flow: 2D axisymmetric contours of the mean radial velocity. The radial profiles are shown on the left at several axial locations which are indicated by dotted lines (····) over the contour plots. — RANS/PDF calculations, ○ Experiment.[66]

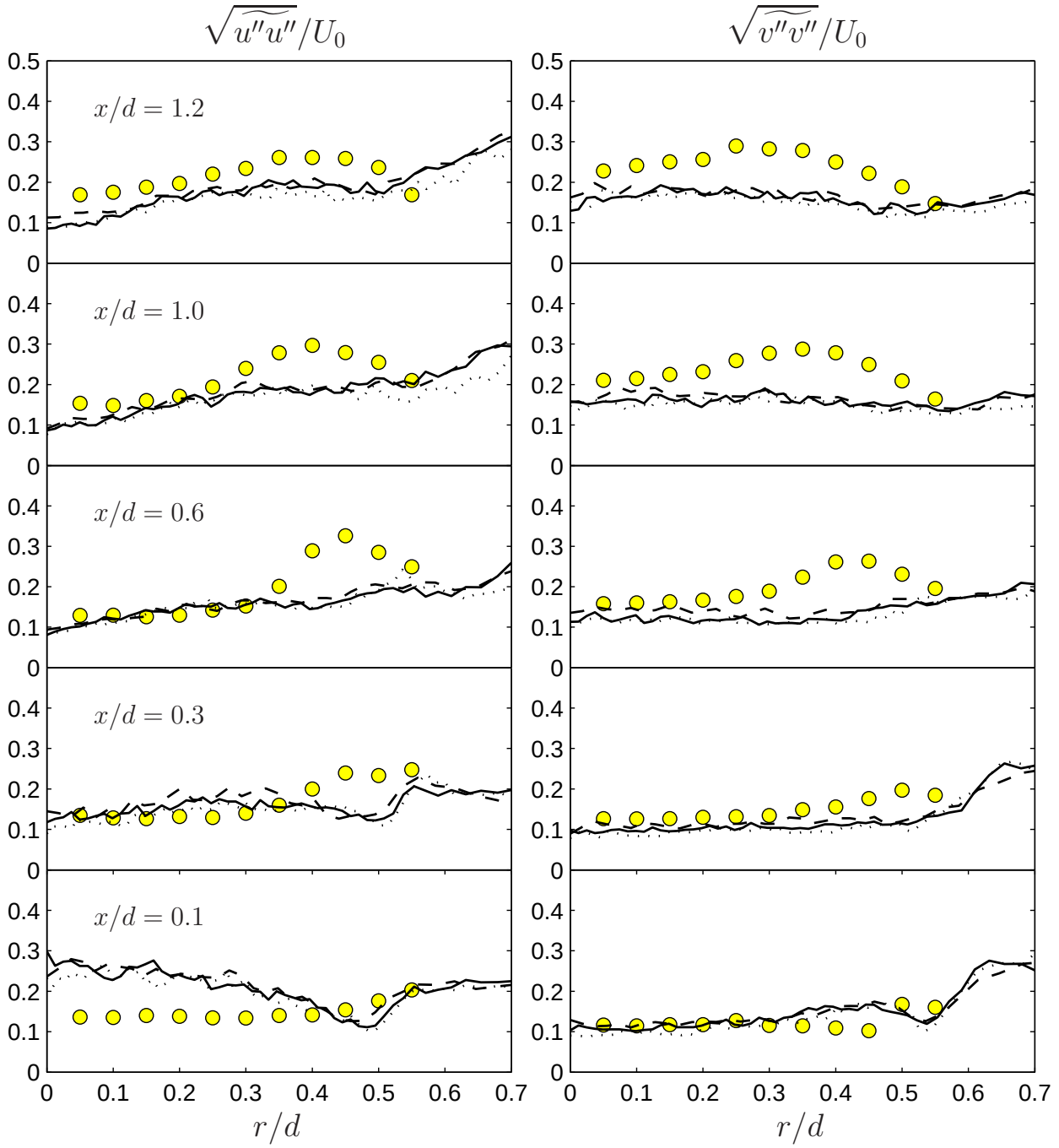

Figure 6: Bluff-body, cold flow: The radial profiles of the rms of the axial and the radial velocity components on three FV-meshes: – – 80×40, — 140×70, and ···· 180×100, where $n_x \times n_r$ indicate number of FV cells in the axial and the radial directions. ○ Experiment.[66]

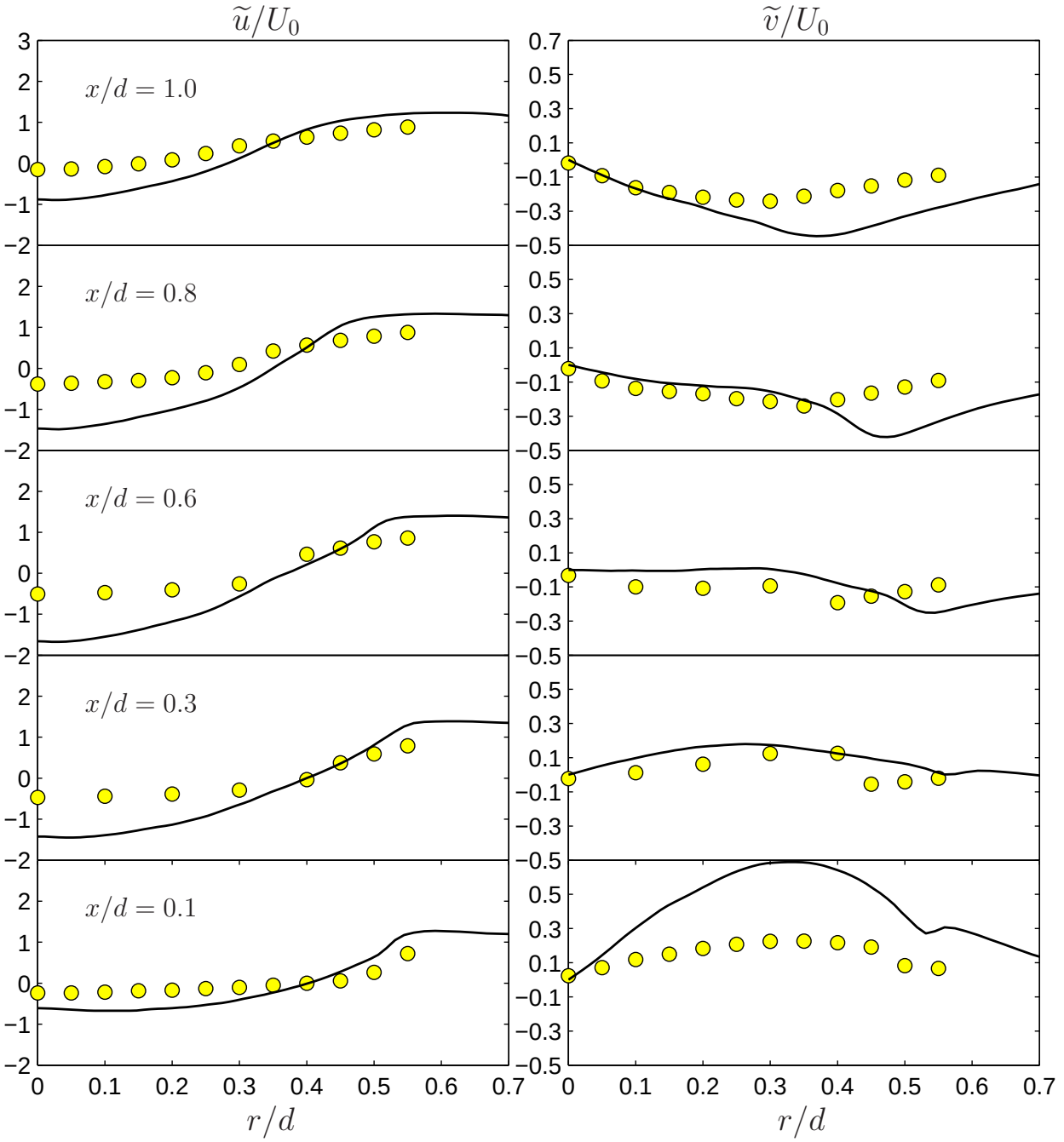

Figure 7: Bluff-body, reacting flow: The radial profiles of the mean axial and radial velocity components. — RANS/PDF calculations, ○ Experiment.[66]

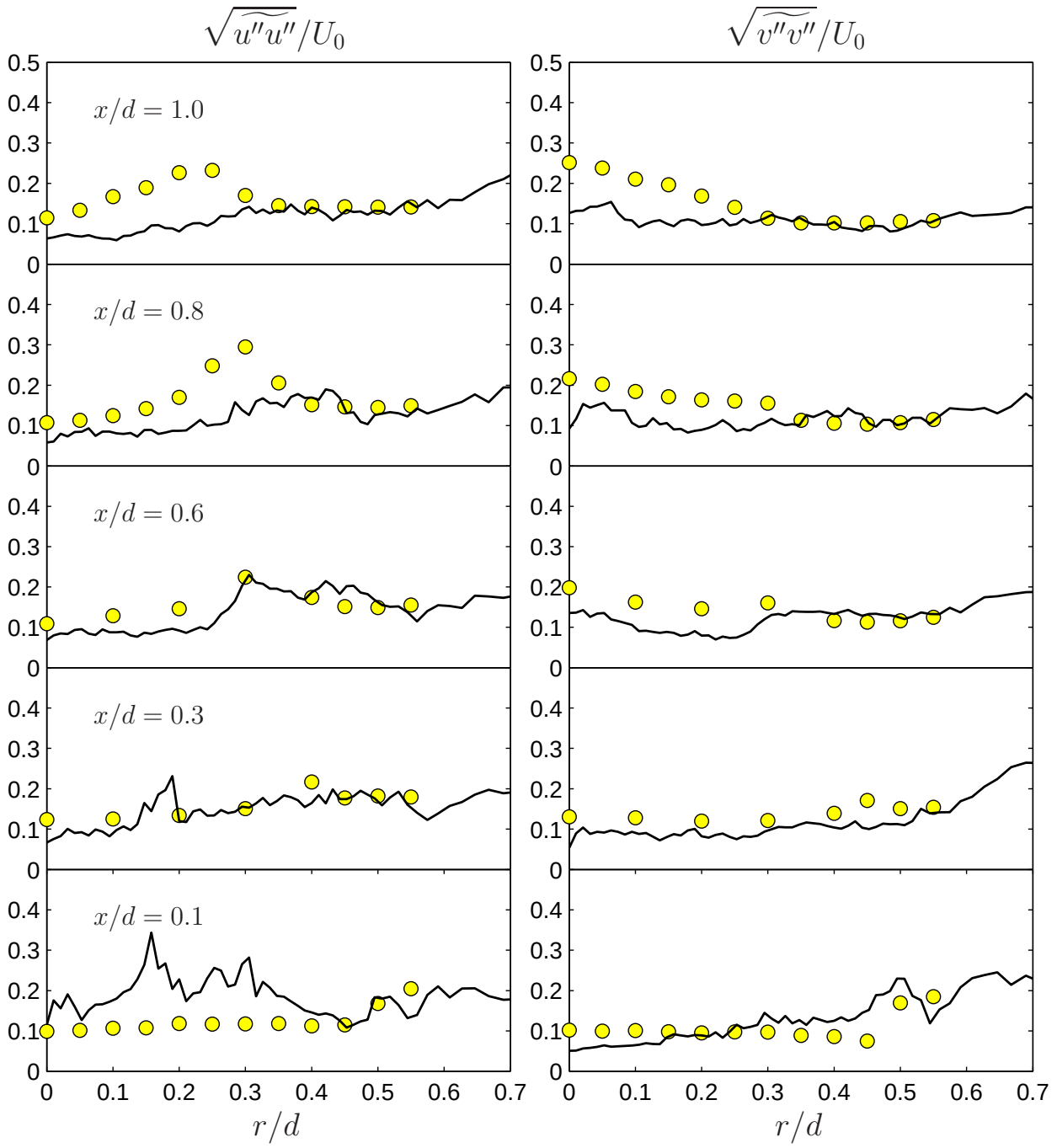

Figure 8: Bluff-body, reacting flow: The radial profiles of the rms of the axial and the radial velocity components. — RANS/PDF calculations, ○ Experiment.[66]

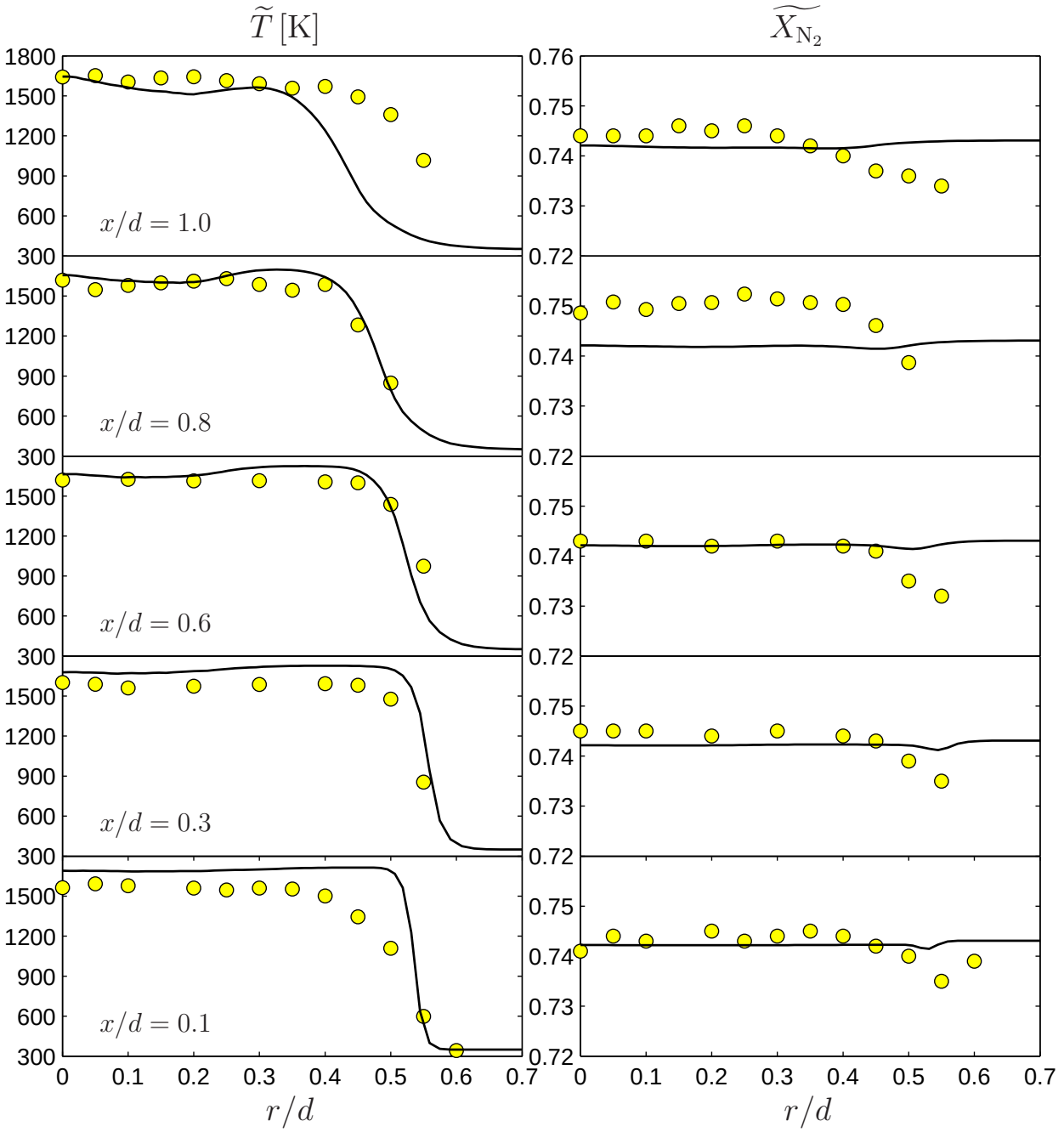

Figure 9: Bluff-body, reacting flow: The radial profiles of the mean temperature and N_2 mole fractions. — RANS/PDF calculations, ○ Experiment.[67]

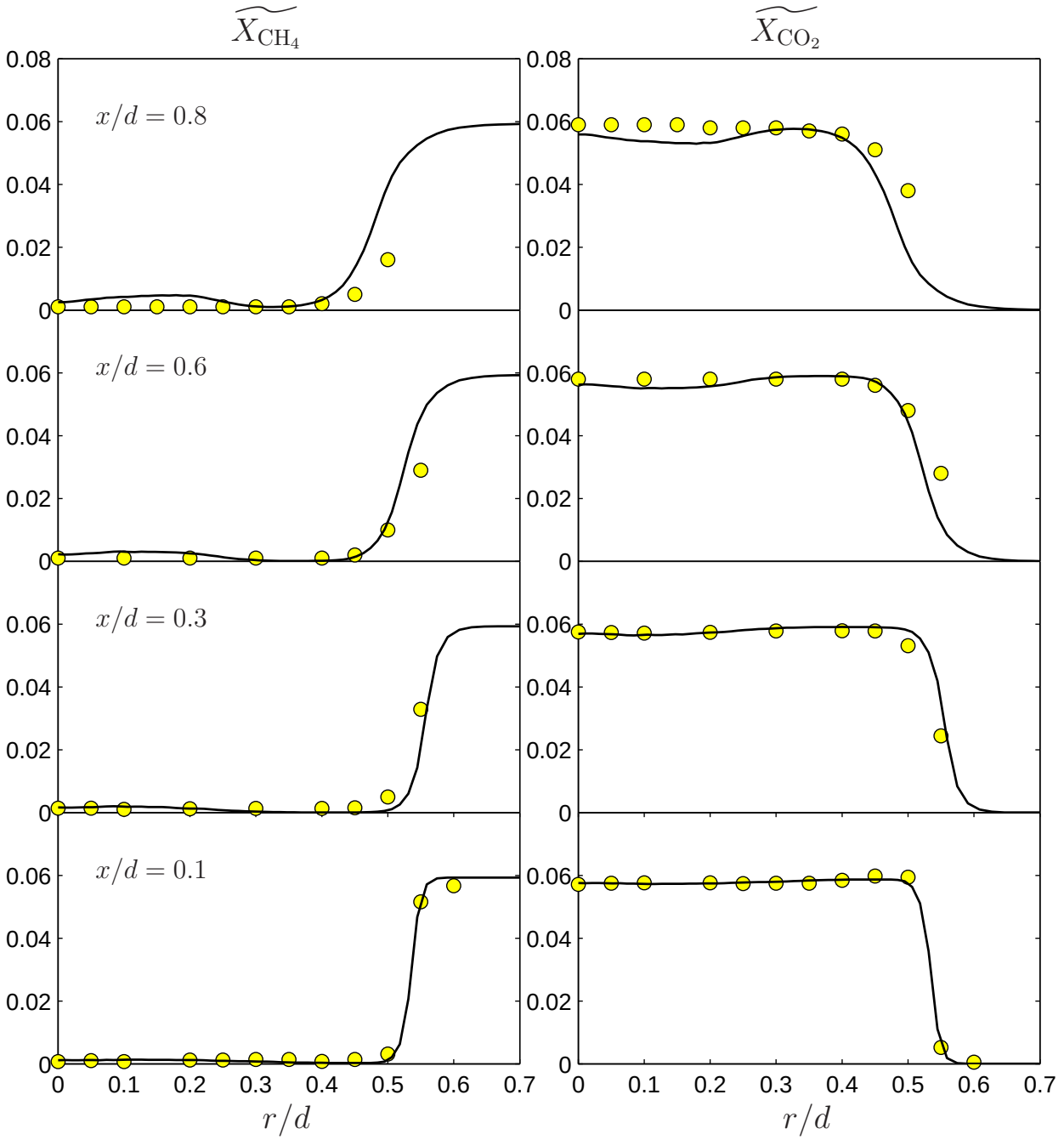

Figure 10: Bluff-body, reacting flow: The radial profiles of the mean CH_4 and CO_2 mole fractions. — RANS/PDF calculations, ○ Experiment.[67]

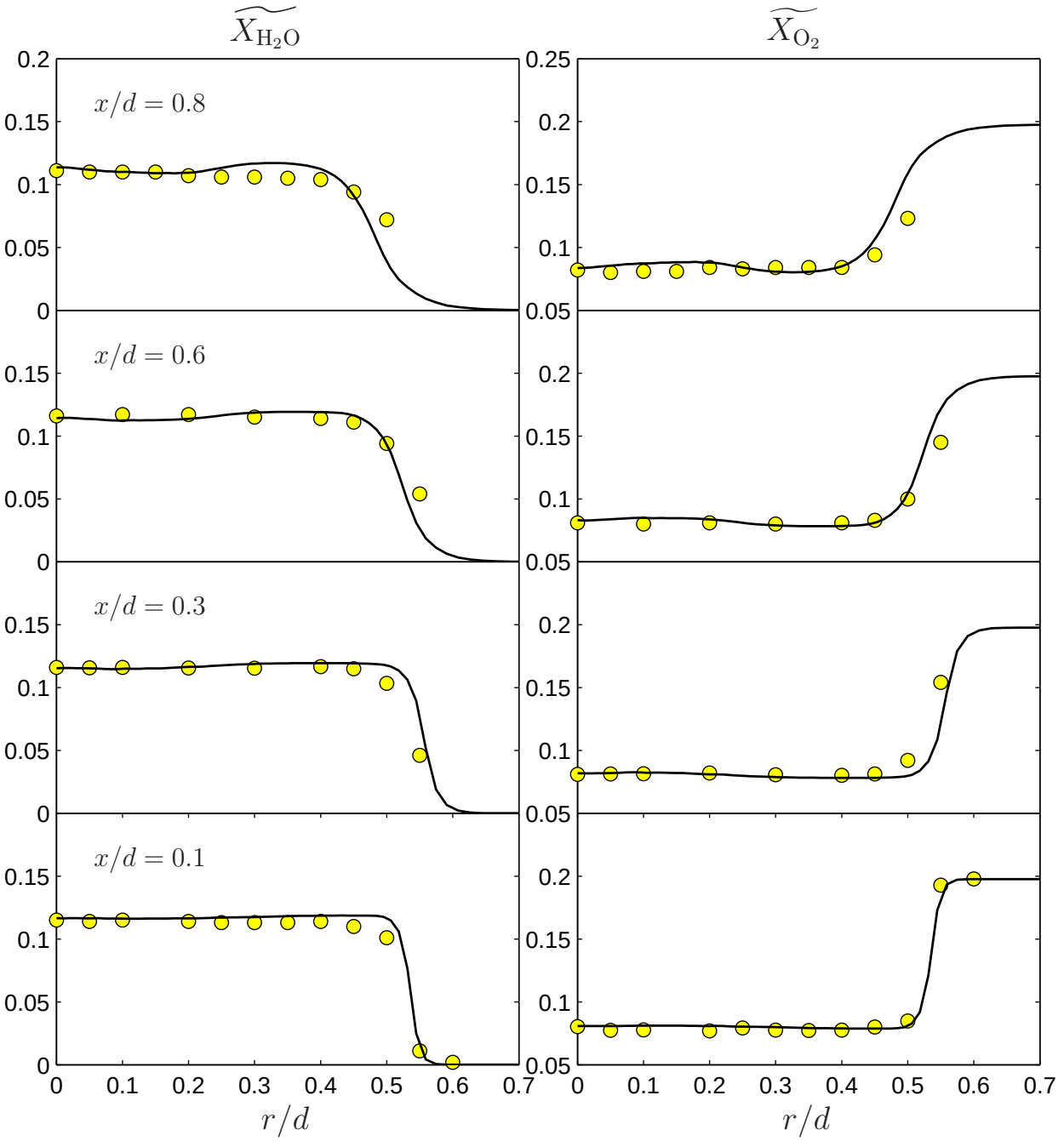

Figure 11: Bluff-body, reacting flow: The radial profiles of the mean H_2O and O_2 mole fractions. — RANS/PDF calculations, ○ Experiment.[67]

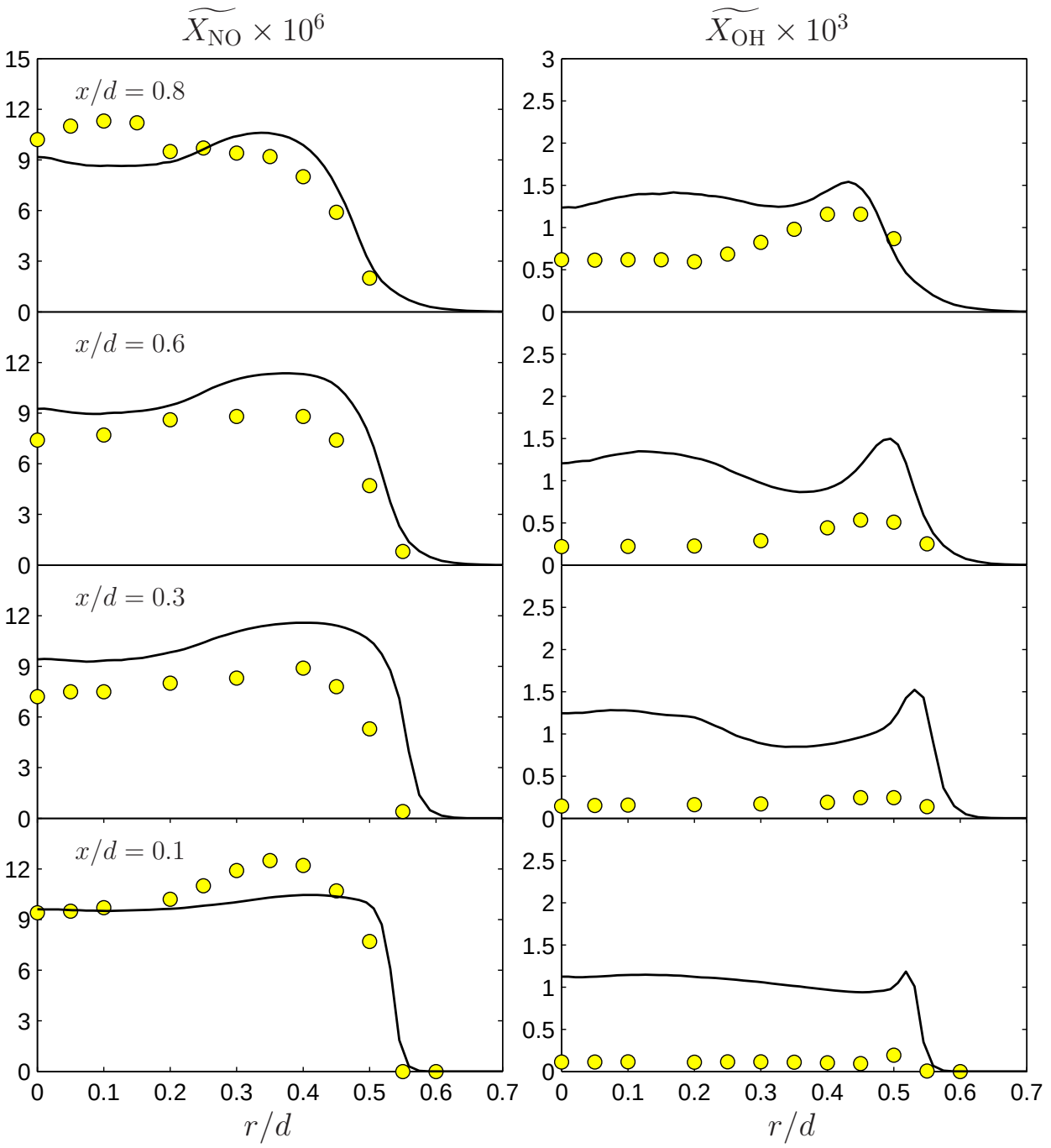

Figure 12: Bluff-body, reacting flow: The radial profiles of the mean NO and OH mole fractions. — RANS/PDF calculations, ○ Experiment.[67]

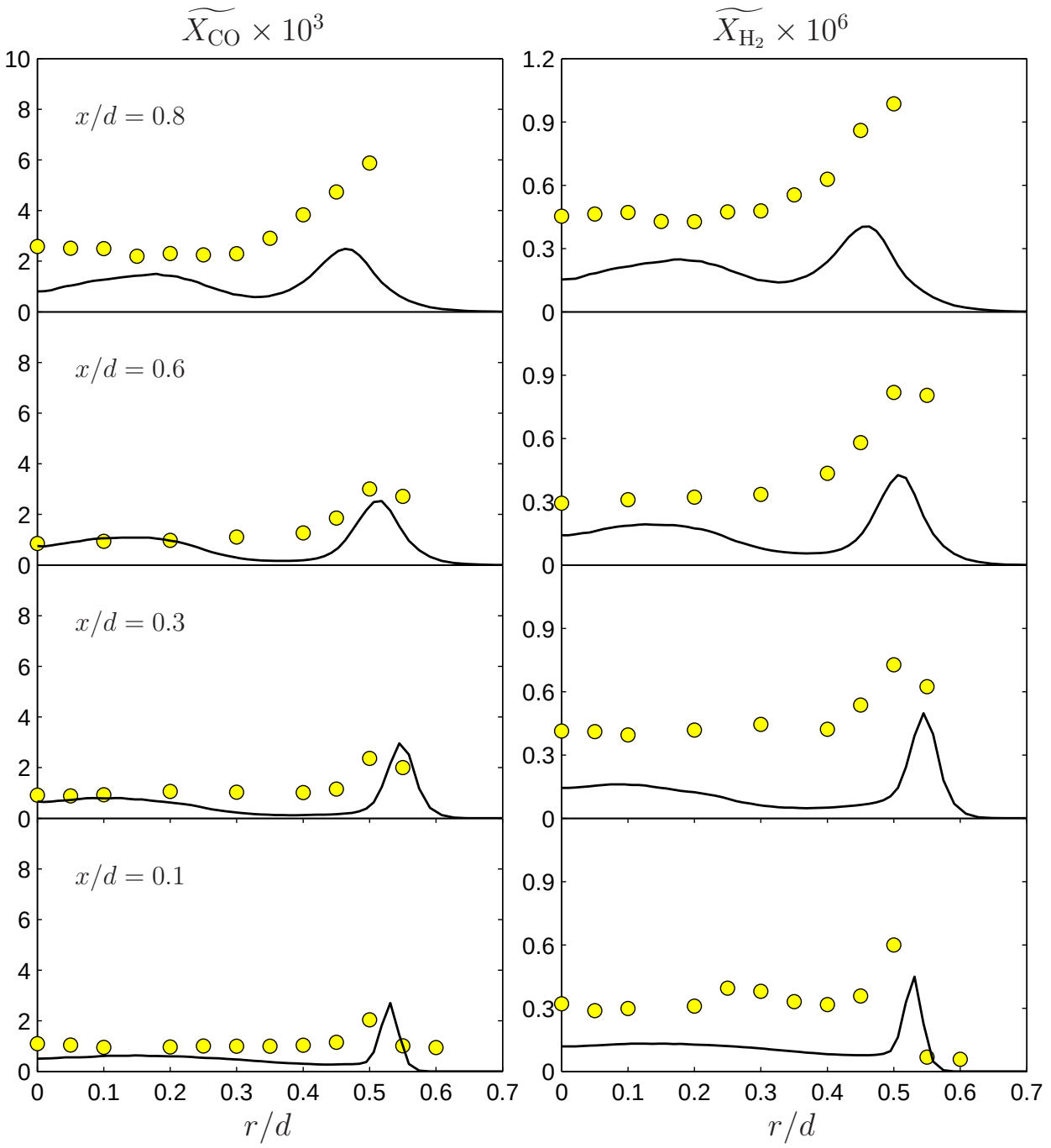

Figure 13: Bluff-body, reacting flow: The radial profiles of the mean CO and H_2 mole fractions. — RANS/PDF calculations, ○ Experiment.[67]

3.0 LES/FDF PREDICTION

In comparison to RANS, the LES/FDF methodology provides a more detailed description of turbulent reacting flows because it accounts for the large scale unsteady transport.[49] Jaberi *et al.*[95] provide the original formulation of FDF for LES of variable-density flows. Sheikhi *et al.*[49] employed FDF for LES of non-premixed flames. Drozda *et al.*[54] and Raman *et al.*[48] applied FDF for prediction of bluff-body stabilized non-premixed flames. A recent application to a complex dump combustor is given by Afshari *et al.*[100] Combustion chemistry is represented by either a flamelet model or global one or two step mechanisms in most of the previous studies.[54] While there are a wide variety of applications in which such chemistry models are appropriate,[44] most practical applications (such as lean premixed gas turbine combustion) require a more accurate representation of chemistry. In this work, LES/FDF with a comprehensive kinetics model is employed for prediction of turbulent premixed flames.

The flow considered is the piloted Bunsen burner configuration investigated experimentally by Chen *et al.*[68] They consider three stoichiometric premixed methane-air flames (F1-F3) featuring a range of Reynolds and Damköhler numbers. Flame F3 is considered here in which Re $\cong$ 22500 and Da $>$ 1. The significance of these flames are that they are dominated by the *distributed-reaction-zones* where the flame stretch by turbulence is important and local quenching effects are possible.[44,68] This is in contrast to the *flamelet-regime* where the chemical flame time is the shortest time scale in the flow.[101–104] The Bunsen burner has been the subject of a number of other numerical investigations. RANS simulations of Flame F3 was conducted by Prasad and Gore[105] using a flame surface density model. Herrmann[106] conducted RANS simulations of all three flames using a level-set flamelet model. LES prediction of the F3-flame is reported by Pitsch and de Lageneste.[107] Lindstedt and Vaos[40] employed a composition PDF model for 2D axisymmetric RANS/PDF predictions of flames

F1 and F3. The present work provides the first application of LES/FDF for a comprehensive study of this flame.

3.1 FORMULATION

We formulate the problem by using the compressible form of the continuity, Navier-Stokes, energy (enthalpy) and species mass conservation equations in a low Mach number flow, along with an equation of state for ideal gas, with negligible radiative heat transfer and viscous dissipation:[101]

$$\frac{\partial \rho}{\partial t} + \frac{\partial \rho u_i}{\partial x_i} = 0 \tag{3.1a}$$

$$\frac{\partial \rho u_i}{\partial t} + \frac{\partial \rho u_i u_j}{\partial x_j} = -\frac{\partial p}{\partial x_i} + \frac{\partial \tau_{ij}}{\partial x_j} \tag{3.1b}$$

$$\frac{\partial \rho \phi_\alpha}{\partial t} + \frac{\partial \rho \phi_\alpha u_j}{\partial x_j} = -\frac{\partial J_i^\alpha}{\partial x_i} + \rho S_\alpha \tag{3.1c}$$

$$p = \rho R T. \tag{3.1d}$$

These equations govern the space ($\boldsymbol{x} \equiv x_i, i = 1, 2, 3$) and time ($t$) variations of the fluid density ρ, the velocity vector $\boldsymbol{u}$, the pressure p, the specific enthalpy $h \equiv \phi_{N_s+1}$, and the species mass fractions $Y_\alpha \equiv \phi_\alpha, \alpha = 1, 2, \ldots, N_s$, where N_s is the number of species. $R = R^0 \sum_{\alpha=1}^{N_s} Y_\alpha / \mathcal{M}_\alpha$ is the mixture gas constant with the universal gas constant denoted by R^0, the molar mass of species by $\mathcal{M}_\alpha$, and T is the temperature. For a Newtonian fluid with zero bulk velocity and Fickian diffusion, the viscous stress tensor τ_{ij}, and the scalar (mass and heat) flux J_i^α are given by,

$$\tau_{ij} = \mu \left(\frac{\partial u_i}{\partial x_j} + \frac{\partial u_j}{\partial x_i} - \frac{2}{3} \frac{\partial u_k}{\partial x_k} \delta_{ij} \right) \tag{3.2a}$$

$$J_i^\alpha = -\gamma \frac{\partial \phi_\alpha}{\partial x_i}, \tag{3.2b}$$

where μ is the dynamic viscosity and $\gamma = \rho\Gamma$ denotes the thermal and the mass diffusivity coefficients for all species (assuming unity Lewis number). The chemical source terms, S_α for $\alpha = 1, \ldots, N_s$, are functions of the composition variables $\boldsymbol{\phi} = [Y_1, Y_2, \ldots, Y_{Ns}, h]$ and are

determined by the gas-phase reaction mechanism. Most of the reaction rate data for pure hydrocarbon fuels up to n-heptane and iso-octane are sufficiently detailed.[81] For example, the GRI-MECH 3.0 mechanism[82] accounts for methane oxidation by considering 325 reactions among 53 species. The rate of reaction k in a mechanism containing r chemical reactions is

$$W_k \equiv k_{fk} \prod_{\alpha=1}^{N_s} \left(\frac{\rho Y_\alpha}{\mathcal{M}_\alpha} \right)^{\nu'_{\alpha k}} - k_{bk} \prod_{\alpha=1}^{N_s} \left(\frac{\rho Y_\alpha}{\mathcal{M}_\alpha} \right)^{\nu''_{\alpha k}}, \tag{3.3}$$

where k_{fk} and k_{bk} are the rate coefficients of the forward and backward reaction, respectively. In general, they are temperature dependent and may also depend on pressure. The exponents $\nu'_{\alpha k}$ and $\nu''_{\alpha k}$ are the stoichiometric coefficients of reaction k in forward and backward direction, respectively. The mass production rate of species α per unit volume and unit time is the sum over all reactions in the mechanism:

$$\rho S_\alpha = \mathcal{M}_\alpha \sum_{k=1}^{r} \nu_{\alpha k} W_k \tag{3.4}$$

where $\nu_{\alpha k} = \nu''_{\alpha k} - \nu'_{\alpha k}$. The sum over all source terms vanishes:

$$\sum_{\alpha=1}^{N_s} \rho S_\alpha = 0 \tag{3.5}$$

Implementation of LES involves the use of the spatial filtering operation[16,108]

$$\langle Q(\boldsymbol{x},t) \rangle_l = \int_{-\infty}^{\infty} Q(\boldsymbol{x}',t)\, \mathcal{G}(\boldsymbol{x}',\boldsymbol{x})\, \mathrm{d}\boldsymbol{x}', \tag{3.6}$$

where $\mathcal{G}$ denotes the filter kernel of width Δ_L, and $\langle Q(\boldsymbol{x},t) \rangle_l$ represents the filtered value of the transport variable $Q(\boldsymbol{x},t)$. In variable density flows it is convenient to consider the Favré filtered quantity, $\langle Q(\boldsymbol{x},t) \rangle_L \equiv \langle \rho(\boldsymbol{x},t) Q(\boldsymbol{x},t) \rangle_l / \langle \rho(\boldsymbol{x},t) \rangle_l$. We consider spatially invariant and localized filter functions, $\mathcal{G}(\boldsymbol{x},\boldsymbol{x}') \equiv \mathcal{G}(\boldsymbol{x}'-\boldsymbol{x})$ with the properties[109] $\mathcal{G}(\boldsymbol{x}) = \mathcal{G}(-\boldsymbol{x})$, and $\int_{-\infty}^{\infty} \mathcal{G}(\boldsymbol{x}) \mathrm{d}\boldsymbol{x} = 1$. Moreover, we only consider "positive" filter functions[110] for which all the moments $\int_{-\infty}^{\infty} x^m \mathcal{G}(x) dx$ exist for $m > 0$.

The filtered form of Eqs. (3.1) is:

$$\frac{\partial \langle\rho\rangle_l}{\partial t} + \frac{\partial \langle\rho\rangle_l \langle u_i\rangle_L}{\partial x_i} = 0 \tag{3.7a}$$

$$\frac{\partial \langle\rho\rangle_l \langle u_j\rangle_L}{\partial t} + \frac{\partial \langle\rho\rangle_l \langle u_i\rangle_L \langle u_j\rangle_L}{\partial x_i} = -\frac{\partial \langle p\rangle_l}{\partial x_j} + \frac{\partial \langle\tau_{ij}\rangle_l}{\partial x_i} - \frac{\partial T_{ij}}{\partial x_i} \tag{3.7b}$$

$$\frac{\partial \langle\rho\rangle_l \langle\phi_\alpha\rangle_L}{\partial t} + \frac{\partial \langle\rho\rangle_l \langle u_i\rangle_L \langle\phi_\alpha\rangle_L}{\partial x_i} = -\frac{\partial \langle J_i^\alpha\rangle_l}{\partial x_i} - \frac{\partial M_i^\alpha}{\partial x_i} + \langle\rho S_\alpha\rangle_l \tag{3.7c}$$

$$\langle p\rangle_l = \langle\rho\rangle_l \langle RT\rangle_L \,, \tag{3.7d}$$

where $T_{ij} = \langle\rho\rangle_l (\langle u_i u_j\rangle_L - \langle u_i\rangle_L \langle u_j\rangle_L)$ and $M_i^\alpha = \langle\rho\rangle_l (\langle u_i\phi_\alpha\rangle_L - \langle u_i\rangle_L \langle\phi_\alpha\rangle_L)$ denote the subgrid scale (SGS) stress tensor and the SGS scalar fluxes, respectively. For non-reacting flows the SGS closure is associated with T_{ij} and M_i^α. In reacting flows, an additional model is required for the filtered reaction rate, $\langle\rho S_\alpha\rangle_l$.

The hydrodynamic SGS closure is based on models that are well established in non-reacting flows.[111–113] The following SGS closure is employed:

$$T_{ij} = -2\langle\rho\rangle_l \nu_t \left(\langle\mathcal{S}_{ij}\rangle_L - \frac{1}{3}\langle\mathcal{S}_{kk}\rangle_L \delta_{ij}\right) + \frac{2}{3} C_I \langle\rho\rangle_l \mathcal{E}\delta_{ij} \tag{3.8}$$

where the SGS viscosity is

$$\nu_t = C_R \Delta_L \mathcal{E}^{\frac{1}{2}}. \tag{3.9}$$

Here $\mathcal{E}$ is the *modified kinetic energy* given as,

$$\mathcal{E} \equiv \left|\langle u_i^*\rangle_L \langle u_i^*\rangle_L - \langle\langle u_i^*\rangle_L\rangle_{l'} \langle\langle u_i^*\rangle_L\rangle_{l'}\right| \tag{3.10}$$

where $u_i^* = u_i - \mathcal{U}_i$ with $\mathcal{U}_i$ being a reference velocity in the x_i direction. The subscript l' denotes a secondary filter level with characteristic filter width $\Delta_{l'} > \Delta_L$. This is the modified kinetic energy-viscosity (MKEV) model, based on the proposed closure by Bardina *et al.*[114] The SGS fluxes are modeled by a similar closure[115]

$$M_i^\alpha = -\langle\rho\rangle_l \gamma_t \frac{\partial \langle\phi_\alpha\rangle_L}{\partial x_i} \tag{3.11}$$

where $\gamma_t = \nu_t/\mathrm{Sc}_t$ is the subgrid diffusivity and Sc_t is the SGS Schmidt number.

The additional model for filtered reaction rates is provided by the *scalar filtered mass density function* (SFMDF). Let $\boldsymbol{\phi}(\boldsymbol{x},t)$ denote the scalar array. We define SFMDF, denoted by F_L, as:

$$F_L(\boldsymbol{\psi};\boldsymbol{x},t) \equiv \int_{-\infty}^{+\infty} \rho(\boldsymbol{x}',t)\,\zeta[\boldsymbol{\psi},\boldsymbol{\phi}(\boldsymbol{x}',t)]\,G(\boldsymbol{x}'-\boldsymbol{x})\,\mathrm{d}\boldsymbol{x}' \tag{3.12}$$

$$\zeta[\boldsymbol{\psi},\boldsymbol{\phi}(\boldsymbol{x},t)] \equiv \delta(\boldsymbol{\psi}-\boldsymbol{\phi}(\boldsymbol{x},t)) \equiv \prod_{\alpha=1}^{N_s+1} \delta(\psi_\alpha-\phi_\alpha(\boldsymbol{x},t)) \tag{3.13}$$

where δ denotes the delta function and $\boldsymbol{\psi}$ denotes the composition domain of the scalar array. The term $\zeta[\boldsymbol{\psi},\boldsymbol{\phi}(\boldsymbol{x},t)]$ is the *fine-grained density*,[18] and Eq. (3.12) implies that the SFMDF is the *mass-weighted spatially filtered* value of the fine-grained density. The integral property of the SFMDF is such that

$$\int_{-\infty}^{+\infty} F_L(\boldsymbol{\psi};\boldsymbol{x},t)\,\mathrm{d}\psi = \int_{-\infty}^{+\infty} \rho(\boldsymbol{x}',t)\,G(\boldsymbol{x}'-\boldsymbol{x})\,\mathrm{d}\boldsymbol{x}' = \langle\rho(\boldsymbol{x},t)\rangle_l\,. \tag{3.14}$$

For further developments, the mass-weighted conditional filtered mean of the variable $Q(\boldsymbol{x},t)$ is defined as

$$\langle Q(\boldsymbol{x},t)\mid\boldsymbol{\psi}\rangle_l \equiv \frac{\int_{-\infty}^{+\infty}\rho(\boldsymbol{x}',t)\,Q(\boldsymbol{x}',t)\,\zeta[\boldsymbol{\psi},\boldsymbol{\phi}(\boldsymbol{x}',t)]\,G(\boldsymbol{x}'-\boldsymbol{x})\,\mathrm{d}\boldsymbol{x}'}{F_L(\boldsymbol{\psi};\boldsymbol{x},t)} \tag{3.15}$$

Equation (3.15) implies the following:

$$\text{(i)} \quad \text{For } Q(\boldsymbol{x},t)=c,\ \ \langle Q(\boldsymbol{x},t)\mid\boldsymbol{\psi}\rangle_l = c, \tag{3.16a}$$

$$\text{(ii)} \quad \text{For } Q(\boldsymbol{x},t)=\hat{Q}(\boldsymbol{\phi}(\boldsymbol{x},t))\,,\ \ \langle Q(\boldsymbol{x},t)\mid\boldsymbol{\psi}\rangle_l = \hat{Q}(\boldsymbol{\psi})\,, \tag{3.16b}$$

$$\text{(iii)} \quad \int_{-\infty}^{+\infty}\langle Q(\boldsymbol{x},t)\mid\boldsymbol{\psi}\rangle_l\,F_L(\boldsymbol{\psi};\boldsymbol{x},t)\,\mathrm{d}\boldsymbol{\psi} = \langle\rho\rangle_l\,\langle Q(\boldsymbol{x},t)\rangle_L \tag{3.16c}$$

where c is a constant, and $\hat{Q}(\boldsymbol{x},t)=Q(\boldsymbol{x},t)$ denotes the case where the variable Q can be completely described by the compositional variable $\boldsymbol{\phi}(\boldsymbol{x},t)$. From Eqs. (3.16), it follows that the filtered value of any function of the scalar variable is obtained by integration over the scalar sample space

$$\int_{-\infty}^{+\infty}\hat{Q}(\boldsymbol{\psi})\,F_L(\boldsymbol{\psi};\boldsymbol{x},t)\,\mathrm{d}\boldsymbol{\psi} = \langle\rho\rangle_l\,\langle Q(\boldsymbol{x},t)\rangle_L\,. \tag{3.17}$$

The transport equation for SFMDF is developed by considering a time derivative of the fine-grained density function:[19,23,116]

$$\frac{\partial \zeta\left(\boldsymbol{\psi},\boldsymbol{\phi}\right)}{\partial t}=\frac{\partial \phi_\alpha\left(\boldsymbol{x},t\right)}{\partial t}\frac{\partial \zeta\left(\boldsymbol{\psi},\boldsymbol{\phi}\right)}{\partial \phi_\alpha}=-\frac{\partial \phi_\alpha\left(\boldsymbol{x},t\right)}{\partial t}\frac{\partial \zeta\left(\boldsymbol{\psi},\boldsymbol{\phi}\right)}{\partial \psi_\alpha}. \tag{3.18}$$

Substituting the scalar transport equation, Eq. (3.1c), for the first derivative on the RHS of Eq. (3.18), we obtain the transport equation for the fine-grained density function

$$\frac{\partial \hat{\rho}\left(\boldsymbol{\phi}\right)\zeta\left(\boldsymbol{\psi},\boldsymbol{\phi}\right)}{\partial t}+\frac{\partial \hat{\rho}\left(\boldsymbol{\phi}\right)u_i\left(\boldsymbol{x},t\right)\zeta\left(\boldsymbol{\psi},\boldsymbol{\phi}\right)}{\partial x_i}=-\left(-\frac{\partial J_i^\alpha}{\partial x_i}+\hat{\rho}\left(\boldsymbol{\phi}\right)\hat{S}\left(\boldsymbol{\phi}\right)\right)\frac{\partial \zeta\left(\boldsymbol{\psi},\boldsymbol{\phi}\right)}{\partial \psi_\alpha} \tag{3.19}$$

Filtering this equation according to Eq. (3.6) yields the transport equation for $F_L\left(\boldsymbol{\psi};\boldsymbol{x},t\right)$. The final result after some algebraic manipulation is,

$$\begin{aligned}\frac{\partial F_L\left(\boldsymbol{\psi};\boldsymbol{x},t\right)}{\partial t} &+ \frac{\partial \left\langle u_i\right\rangle_L F_L\left(\boldsymbol{\psi};\boldsymbol{x},t\right)}{\partial x_i}=-\frac{\partial \hat{S}_\alpha\left(\boldsymbol{\psi}\right)F_L\left(\boldsymbol{\psi};\boldsymbol{x},t\right)}{\partial \psi_\alpha}\\ &- \frac{\partial}{\partial x_i}\left[\left(\left\langle u_i \mid \boldsymbol{\psi}\right\rangle_l-\left\langle u_i\right\rangle_L\right)F_L\left(\boldsymbol{\psi};\boldsymbol{x},t\right)\right]\\ &+ \frac{\partial}{\partial \psi_\alpha}\left[\left\langle \frac{1}{\hat{\rho}\left(\boldsymbol{\phi}\right)}\frac{\partial J_i^\alpha}{\partial x_i}\,\middle|\,\boldsymbol{\psi}\right\rangle_l F_L\left(\boldsymbol{\psi};\boldsymbol{x},t\right)\right].\end{aligned} \tag{3.20}$$

This is an exact transport equation for the SFMDF. The first term on the RHS of this equation is due to chemical reaction and is in a closed form. The unclosed nature of SGS convection and mixing is manifested by the last two conditional filtered terms, modeling of which is discussed in the next subsection.

3.2 MODELING AND SIMULATION

3.2.1 SGS Closure

Intimately related to the FDF methodology is the procedure by which its transport equation is solved. The coupling between numerics and SGS modeling is important in all LES,[117] but is particularly noticeable in FDF. The simulation procedure is similar to that followed in numerical simulation of most other stochastic phenomena. This involves consideration of a set of stochastic differential equations (SDEs).[86–88] All of the modeling in the FDF transport equation is via selection of the parameters of the SDEs. The diffusion process[89,118] has proven effective for this purpose. The coefficients in the Langevin equation governing this process are set in such a way that the resulting Fokker-Planck equation[90] defines the modeled FDF transport equation. In addition to providing the closure, the SDEs are much more amenable to numerical simulations than are the high-dimensional Fokker-Planck or the actual FDF transport equation, Eq. (3.20). The diffusion process considered to model this equation is,

$$\mathrm{d}X_i^+(t) = D_i\left(\boldsymbol{X}^+(t),t\right)\mathrm{d}t + E\left(\boldsymbol{X}^+(t),t\right)\mathrm{d}W_i(t) \tag{3.21a}$$

$$\mathrm{d}\phi_i^+ = \left[-\Omega_m\left(\phi_\alpha^+ - \langle\phi_\alpha\rangle_L\right) + S_\alpha\left(\boldsymbol{\phi}^+\right)\right]\mathrm{d}t \tag{3.21b}$$

where X_i^+ and ϕ_α^+ are probabilistic representations of position and scalar variables, respectively. D_i is the *drift* and E is the *diffusion* coefficient given as,

$$D_i\left(\boldsymbol{X}(t),t\right) = \langle u\rangle_L + \frac{1}{\langle\rho\rangle_l}\frac{\partial\langle\rho\rangle_l(\gamma+\gamma_t)}{\partial x_i} \tag{3.22a}$$

$$E\left(\boldsymbol{X}(t),t\right) = \sqrt{2(\gamma+\gamma_t)/\langle\rho\rangle_l} \tag{3.22b}$$

The $\boldsymbol{W}$ term denote the Wiener-Lévy process[89] in the physical space. The equation proposed for evolution of ϕ_α^+ is known as the *linear mean square estimation* (LMSE) model,[22] where Ω_m is the frequency of SGS mixing modeled as

$$\Omega_m = C_\Omega\frac{\gamma+\gamma_t}{\Delta_L^2} \tag{3.23}$$

The Fokker-Planck corresponding to SDEs in Eqs. (3.21a) and (3.21b) is,[54]

$$\begin{aligned}\frac{\partial F_L}{\partial t} &+ \frac{\partial \langle u_i\rangle_L F_L}{\partial x_i} = -\frac{\partial S_\alpha F_L}{\partial \psi_\alpha} \\ &+ \frac{\partial}{\partial x_i}\left[(\gamma+\gamma_t)\frac{\partial F_L/\langle\rho\rangle_l}{\partial x_i}\right] + \frac{\partial}{\partial \psi_\alpha}\left[\Omega_m\left(\psi_\alpha - \langle\phi_\alpha\rangle_L\right)F_L\right]\end{aligned} \tag{3.24}$$

This is the model equation for SFMDF transport. A one-to-one comparison with exact transport Eq. (3.20), implies the following closure:

$$\begin{aligned}\frac{\partial}{\partial x_i}\left[\left(\langle u_i \mid \boldsymbol{\psi}\rangle_l - \langle u_i\rangle_L\right)F_L\right] &+ \frac{\partial}{\partial \psi_\alpha}\left[\left\langle -\frac{1}{\rho}\frac{\partial}{\partial x_i}\left(\gamma\frac{\partial \phi_\alpha}{\partial x_i}\right)\,\middle|\,\boldsymbol{\psi}\right\rangle_l F_L\right] \\ &\approx +\frac{\partial}{\partial x_i}\left[(\gamma+\gamma_t)\frac{\partial F_L/\langle\rho\rangle_l}{\partial x_i}\right] + \frac{\partial}{\partial \psi_\alpha}\left[\Omega_m\left(\psi_\alpha - \langle\phi_\alpha\rangle_L\right)F_L\right].\end{aligned} \tag{3.25}$$

The modeled transport equation Eq. (3.24) can be multiplied by ψ^n and integrated in the composition space ψ to obtain a modeled transport equation for the Favré moments. For example, for the first Favré moment,

$$\frac{\partial \langle\rho\rangle_l \langle\phi_\alpha\rangle_L}{\partial t} + \frac{\partial \langle\rho\rangle_l \langle u_i\rangle_L \langle\phi_\alpha\rangle_L}{\partial x_i} = \frac{\partial}{\partial x_i}\left(\langle\rho\rangle_l (\gamma+\gamma_t)\frac{\partial \langle\phi_\alpha\rangle_L}{\partial x_i}\right) + \langle\rho\rangle_l \langle S_\alpha\rangle_L . \tag{3.26}$$

Note that this equation is fully consistent with the filtered scalar transport equation Eq. (3.7c).

3.2.2 Solution Procedure

Numerical solution of the equations governing the resolved field is based on a hybrid scheme in which the hydrodynamic Favré filtered equations Eqs. (3.7) are integrated by a finite difference (FD) method, and the filtered scalar field is simulated by the Monte Carlo (MC) solution of the SFMDF transport equation, Eq. (3.24). The FD is based on a fourth order *compact parameter* scheme.[119] A second order symmetric predictor-corrector sequence is employed for temporal integration of Eqs. (3.7). In addition to Favré filtered quantities, the solution of these equations also provide the SGS eddy viscosity ν_t, and the SGS eddy diffusivity γ_t. The filtered pressure, $\langle p\rangle_l$, is obtained from the filtered equation of state, Eq. (3.7d). Standard characteristic boundary conditions[120,121] are implemented for the continuity, momentum and energy transport equations. All FD operations are conducted on

a uniform and fixed mesh with grid points separated by length Δx, Δy and Δz in three coordinate directions, respectively.

The SFMDF is represented by an ensemble of particles, each attributed with a set of scalars $\phi_\alpha^{(n)}(t)$ and Lagrangian position vector, $\boldsymbol{X}^{(n)}(t)$. Initially, the particles are uniformly distributed in the solution domain with scalar values assigned in accord with the initial filtered FD fields. This information is updated via temporal integration of the modeled SDEs given in Eqs. (3.21). The particle position is integrated via the Euler-Maruyamma approximation:[92]

$$X_i^{(n)}\left(t_{k+1}\right) = X_i^{(n)}\left(t_k\right) + D_i^{(n)}\left(t_k\right)\Delta t + E_i^{(n)}\left(t_k\right)\Delta t^{1/2}\xi_i^{(n)}\left(t_k\right) \tag{3.27}$$

where Δt is the computational time increment between two consecutive time levels, $\xi^{(n)}$ is a random number with normal distribution, and $D_i^{(n)}$ and $E_i^{(n)}$ are, respectively, the drift and diffusion coefficients in Eqs. (3.22) evaluated at the particle location $\boldsymbol{X}^{(n)}$ at time t.

3.2.3 Chemistry

The scalar equation contains the reaction source terms and the mixing term. A comprehensive description of the gas phase kinetics is provided by elementary reaction mechanisms, where reaction source terms are obtained by Eq. (3.4). However, the use of such detailed mechanisms in full scale combustion simulations is computationally prohibitive. In order to overcome this problem a whole range of methods have been developed; see Law and Lu[122] for a recent review. These include mechanism reduction techniques through time-scale analysis and stiffness elimination (steady-state and partial equilibrium assumptions,[123] intrinsic low-dimensional manifold,[124] computational singular perturbation[125]), removal of unimportant reactions and species (skeletal reduction), combination of species and reaction pathways (lumping[126]), and other techniques such as artificial neural network,[127,128] self-organizing map,[129] genetic algorithm,[130] graph theory[131,132] and tabulation.[133] In this work, a systematically reduced mechanism[97] is used which is obtained by steady-state approximation applied to GRI-MECH 2.11 elementary methane mechanism.[98] The reduced mechanism is described by 5 global reaction steps containing 9 solved and 38 steady state species. The

solved species are CH_4, O_2, H_2O, CO_2, N_2, OH, NO, H_2 and CO. The global reactions steps are:

$$\begin{aligned}
&\text{R1}: && 3H_2 + O_2 + CO_2 \Longleftrightarrow 3H_2O + CO \\
&\text{R2}: && H_2 + 2OH \Longleftrightarrow 2H_2O \\
&\text{R3}: && 3H_2 + CO \Longleftrightarrow H_2O + CH_4 \\
&\text{R4}: && H_2 + CO_2 \Longleftrightarrow H_2O + CO \\
&\text{R5}: && 3H_2 + CO_2 + 2NO \Longleftrightarrow 3H_2O + CO + N_2
\end{aligned} \tag{3.28}$$

Even with the reduction the source terms in Eq. (3.21b) contain contributions from reactions of different time scales, which vary by several orders of magnitude. Also, the mixing time scale is determined by SGS mixing frequency, and is generally different from the reaction time scales. Therefore, the scalar equation Eq. (3.21b) is a stiff non-linear ordinary differential equation. Solution of this equation is obtained via the stiff ODE solver VODE,[134] with Ω_m and $\langle \phi_\alpha \rangle_L$ updated at each flow time step.

To understand the operational procedures of the hybrid configuration, the elements of the computation are shown, in two dimensions, in Fig. 14. This figure shows the MC particles randomly distributed and freely moving within the domain. This transport is Lagrangian, thus the solution is free of constraints associated with typical convection on fixed grid points. Statistical information is obtained by considering an ensemble of N_E particles residing within an ensemble domain of characteristic length Δ_E and centered around a FD grid point. The ensemble approach is necessary as the probability of finding any particle at the exact location of a given finite-difference grid point is zero.[25] The Favré filter of a given scalar, $\langle Q(\phi(\boldsymbol{x},t)) \rangle_L$, is obtained by taking an average of the values attributed to each particle in the ensemble domain, $Q\left(\phi^{(n)}\right)$. Specification of the size of the ensemble domain is an important issue. The ideal condition for accurate statistics requires $\Delta_E \to 0$ and $N_E \to \infty$. With a finite number of particles, if Δ_E is small there may not be enough particles to construct reliable statistics. A larger ensemble domain decreases the statistical error, but increases the spatial error which manifests itself in artificially diffused statistical results. This compromise between the statistical accuracy and dispersive accuracy as pertaining to Lagrangian MC schemes implies that the optimum magnitude of Δ_E cannot, in general, be

specified *a priori*.[20,135] This does not diminish the capability of the scheme, but exemplifies the importance of the parameters which govern the statistics.

To reduce the computational cost and maintain a nearly uniform particle *number* distribution in a variable density flow, a procedure involving non-uniform particle *weights* is used. This allows a smaller number of particles to be imposed in regions where a low degree of variability is expected. Conversely, in regions of high varying character, a larger number of particles is allowed. This strictly numerical treatment is analogous to grid compression in FD schemes. Figure 15 shows a sample instantaneous contour of the instantaneous ensemble particle weights (*i.e.*, $\sum_{n\in(\Delta_E)^3} w^{(n)}$) and the particle number density (*i.e.*, $\sum_{n\in(\Delta_E)^3}(1)$) at each FD grid points. Operationally, the particles evolve with a discrete SFMDF,

$$F_N\left(\boldsymbol{\psi};\boldsymbol{x},t\right)=\Delta m\sum_{n=1}^{N}w^{(n)}\delta\left(\boldsymbol{\psi}-\boldsymbol{\phi}^{(n)}\right)\delta\left(\boldsymbol{x}-\boldsymbol{X}^{(n)}\right) \tag{3.29}$$

where $w^{(n)}$ is the weight of the n-th particle and Δm is the mass of a particle with unit weight. The SFMDF is the expectation of the discrete SFMDF

$$\begin{aligned} F_L\left(\boldsymbol{\psi};\boldsymbol{x},t\right) &= \Delta m\sum_{n=1}^{N}\left\langle w^{(n)}\delta\left(\boldsymbol{\psi}-\boldsymbol{\phi}^{(n)}\right)\delta\left(\boldsymbol{x}-\boldsymbol{X}^{(n)}\right)\right\rangle \\ &= \Delta m\left\langle w^{(n)}\delta\left(\boldsymbol{\psi}-\boldsymbol{\phi}^{(n)}\right)\delta\left(\boldsymbol{x}-\boldsymbol{X}^{(n)}\right)\right\rangle \text{ for any } n=1,\ldots,N \end{aligned} \tag{3.30}$$

where $\langle\ \rangle$ indicates ensemble averaging. With integration of this expression over the composition domain within an infinitesimal volume, it can be shown that

$$\left\langle\rho\right\rangle_l\approx\frac{\Delta m}{\Delta V}\sum_{n\in\Delta_E}w^{(n)}, \tag{3.31}$$

where ΔV is the volume of the ensemble domain. The Favré-filtered value of a transport quantity $\hat{Q}(\boldsymbol{\phi})$ is constructed from the weighted average

$$\left\langle Q\right\rangle_L\approx\frac{\sum_{n\in\Delta_E}w^{(n)}\hat{Q}\left(\boldsymbol{\phi}^{(n)}\right)}{\sum_{n\in\Delta_E}w^{(n)}} \tag{3.32}$$

The approximations in Eqs. (3.31) and (3.32) are exact in the limit $\Delta_E\to 0$ and $N_E\to\infty$.[20] Equation (3.31) implies that the filtered fluid density is directly proportional to the sum of the weight in the ensemble domain. With uniform weights, $\left\langle\rho\right\rangle_l\approx(\Delta m/\Delta V)N_E$ and

$\langle Q \rangle_L \approx (1/N_E) \sum Q^{(n)}$. Hence, with uniform weights, the particle number density decreases significantly in regions of low density. The implementation of variable weights allows the increase of the particle number density without a need to increase the number density outside the reaction zone. The process of ensemble averaging of a MC variable is further illustrated in Fig. 16. This figure shows different representations of a turbulent quantity in the hybrid scheme.

3.2.4 Parallelization

In a typical simulation, millions of MC particles are required for accurate extraction of statistics. The MC solver typically consumes more than 95% of the total computation time. The CPU requirements of LES/FDF computations under various conditions are given in Table 2. Clearly, sequential execution of an LES/FDF solver is not very efficient and scalable parallelization at the particle level is required

At any time during the flow evolution, different regions of the flame undergo different stages of the combustion process with varying levels of computation intensity. Consequently, even with a uniform particle number density, computational load from one ensemble domain to another varies significantly. The primary reason for this imbalance is the varying level of stiffness due to chemistry. For some state of the chemical composition, the integration of chemistry over the flow time-step can be done quickly via a few explicit sub-steps. However, for some other states, *e.g.* near extinction/reignition regions, implicit stepping over many smaller sub-steps is required. This is particularly expensive due to calculations of the Jacobian matrix corresponding to Eq. (3.21b). The computational load variation is illustrated in Fig. 17. On the left, the instantaneous filtered CO mass fraction field is shown. It is representative of the combustion process and somewhat indicates the variations in stiffness. On the right, the total computation time for integration of the particle equations inside each ensemble domain is shown. It is observed that the computational requirement very much non-uniform throughout the domain and is a function of proximity to the flame region. Vir-

tually no time is spent during calculations near the cold jet or the cold surrounding air, and most of the computational load is concentrated at the shear layer regions around the hot pilot.

A popular parallelization strategy in structured FD/FV is the uniform and fixed-in-time block domain decomposition.* With this technique, the mesh is partitioned into equally sized domains and each partition assigned to different processors at the onset of the simulation. In most cases, this provides an effective parallelization and is relatively easy to implement. However, it can lead to extremely poor load distribution in LES. This is illustrated in Fig. 18 where the domain is uniformly decomposed, and each CPU is assigned equal number of grid points and (approximately) equal number of particles. As shown, the computational load is *not* equally distributed, and processors with less amount of load complete their part of the job and remain idle until the synchronization at the end of each time step. To remedy the problem, an *adaptive* decomposition procedure is developed. The decomposition represents the uniform Eulerian mesh as a weighted undirected graph of grids points. That is, as far as the decomposition of the MC solver, the grid is assumed to be unstructured. A *weight* is attributed to each grid point based on the total computational requirements for particles inside the ensemble domain around the grid point. The grids are then decomposed via a weighted-graph partitioning algorithm[136] which partitions the domain into clusters of ensemble domains, which in general, do not have a structured shape. Figure 19 illustrates this decomposition technique. In contrast with Fig. 18, the idle CPU time is greatly reduced.

As the simulation proceeds, the computational requirements change in a transient manner, and the load becomes imbalanced again. When the imbalance reaches to a certain threshold, the partitioning procedure is repeated and the data in previous partition are migrated to the new partition. Depending on the communication requirements and the computational cost of computing the metric, the frequency of the load redistribution can be adjusted.

*Domain decomposition is used to mean *Data Decomposition*, not to be confused with domain decomposition in preconditioning methods for solution of linear systems.

Table 2: CPU and run time requirements of 3D LES/FDF

	Case-1	Case-2	Case-3
Number of grids	10^6	10^6	5×10^6
Number of particles	6×10^6	6×10^6	50×10^6
Number of species/reactions[a]	5/9	15/19	15/19
Required memory (GBs)	1.69	2.48	24.0
GFLOP[b] per iteration	29.5	90.7	544.7
Number of iterations[c]	60,000	60,000	220,000
Run-time with 1 GFLOP per second[d]	20.5 days	63.0 days	3.8 years

[a] An additional chemical mechanism with 15 solved species and 19 reduced reactions[137] is considered only for the purpose of estimating computational requirements. This mechanism is not used in actual flame simulations.

[b] 10^9 floating point operations.

[c] Based on several residence times on the same domain size and flow conditions.

[d] Flop/s rate based on a highly optimized sequential code for the Cray-XT3 system at the Pittsburgh Supercomputing Center.

3.3 FLAME CONFIGURATION AND MODEL PARAMETERS

The schematic diagram of the Bunsen burner that is considered in the experiments of Chen *et al.*[68] is shown in Fig. 20. The nozzle diameter for the jet stream, d, is 1.2 cm and the pilot stream issues through a perforated plate around the central nozzle with an outer diameter of 6.8 cm. Both the pilot and the jet contain stoichiometric methane-air mixtures, *i.e.*, equivalence ratio is $\phi = 1.0$. The mean exit velocities are 3000 cm/s at the nozzle and 22 cm/s at the pilot (84 cm/s through each one of 1175 perforations of 1-mm diameter). The Reynolds number based on the jet diameter is $22,400$.

Table 3 lists the values of some of the simulation parameters and reference quantities. The magnitude of the mean and the rms-velocity imposed at the inlet are those measured by Chen *et al.*[68] and are shown in Fig. 21. The flow is excited by superimposing oscillating axial and helical perturbations at the inlet plane. The procedure is similar to that of Danaila and Boersma.[138] The amplitude of the perturbations is adjusted to match the inlet mean and the rms velocity values as obtained experimentally. The pilot flame and the perforated plate are represented by issuing stoichiometric hot burnt gas at the mean pilot velocity. The jet composition is a stoichiometric methane-air at 300K. The pilot composition and enthalpy are calculated using chemical equilibrium with 10% heat-loss to the burner ($T = 2000K$), which corresponds to the experimentally reported temperature at the pilot exit. Partially reflecting characteristic boundary conditions[120] are implemented at the outlet, and non-reflecting characteristics[139] are imposed at the lateral boundaries allowing for cold air entrainment. The computational domain spans a region of $12d \times 10d \times 10d$ in the stream-wise (x) and the two lateral (y, z) directions, respectively. The number of grid points is $101 \times 91 \times 91$ in the x, y and z directions, respectively. The filter size is set equal to $\Delta_L = 2(\Delta x \Delta y \Delta z)^{1/3}$, where Δx, Δy and Δz are grid spacings in the corresponding directions. The size of the ensemble domain is set to twice the filter size. There are approximately 48 particles per ensemble domain. These selections for MC simulation is made based on previous studies,[47,54,95,135,140] where it is shown to be sufficient to yield statistical accuracy with minimal dispersive errors.

Table 3: Summary of the simulation parameters and reference quantities.

Parameter	Value	Description
$\Delta x, \Delta y, \Delta z$	(0.125,0.111,0.111)	FD grid spacing
Δ_L	$(\Delta x \Delta y \Delta z)^{1/3}$	Characteristic filter size
C_I	0	MKEV model parameter
C_R	0.1	MKEV model parameter
$\boldsymbol{\mathcal{U}}$	(0.8,0,0)	MKEV reference velocity
$\Delta_{l'}$	$3\Delta_L$	Characteristic secondary filter size
$\mathrm{Sc_t}$	0.75	SGS Schmidt number
C_Ω	8.0	SGS mixing frequency
r_{tol}	10^{-6}	Relative tolerance for ODE solver
a_{tol}	10^{-9}	Absolute tolerance for ODE solver
L_{ref}	1.2 cm	Reference length (integral length scale)
U_{ref}	3000 cm/s	Reference speed
t_{ref}	4×10^{-4} s	Reference time
T_{ref}	300 K	Reference temperature
p_{ref}	1 atm	Reference pressure
γ_{ref}	1.387	Reference specific heat ratio
ρ_{ref}	1.1125×10^{-3} g/cm^3	Reference density
μ_{ref}	1.1805×10^{-4} g/cm s	Reference viscosity
Re	22,400	Reynolds number
Ma	0.085	Mach number

3.4 RESULTS

The predictive capability of LES/FDF is demonstrated by comparing flow statistics with the available experimental data. These statistics are obtained by time averaging of the filtered field over 3 flowthrough (residence) times. A total of 30,000 samples of each of the variables are collected in this recording period. The notation $\overline{Q}$ denote the time-averaged mean value of the variable Q. Note that time-averaged mean fields extracted as such from the filtered fields are equivalent to the time-averaged results reported in the experiments given that the filter is generic and that the filter size Δ_L remains small.

3.4.1 Cold Flow

The predictive capability of the solver is demonstrated via comparisons of the cold flow statistics with laboratory data. Chen *et al.*[68] reports cold flow measurements for the mean axial velocity, $\overline{u}$, and the turbulent kinetic energy, $k = \overline{u_i'' u_i''/2}$. Variation of the mean axial velocity and the turbulent kinetic energy along the axial direction at the centerline of the burner is shown in Fig. 22. The radial profiles are shown at several axial locations in Fig. 23. The contribution of the SGS kinetic energy is ignored since it cannot be estimated accurately via the MKEV model. The measurements indicate the spreading of the mean axial velocity corresponding to open jet flows. The potential core extends approximately to $x/d = 4.5$, where the maximum mean velocity decreasing at a faster rate as the jet expands in the radial direction. These are captured reasonably well.

3.4.2 Consistency Assessments

The objective of this section is to demonstrate the consistency of the hybrid algorithm used for LES/FDF. For this purpose, comparison is made of the $\langle \rho \rangle_l$ and $\langle RT \rangle_L$ fields as obtained from both the MC and FD solvers. Also considered is a conserved passive scalar variable f. This variable is governed by the scalar transport equation, Eq. (3.7c), and by the stochastic equation, Eq. (3.21b), both with $S = 0$. The inlet profile for $\langle f \rangle_L$ is taken as that of the

streamwise velocity in Fig. 21 normalized to the range $[0, 1]$. Equation (3.32) is used in MC for $\langle RT \rangle_L$, $\langle f \rangle_L$ and the MC density, defined as

$$\langle \rho \rangle^{\mathrm{MC}} \equiv \left(\frac{\sum_{n \in \Delta_E} w^{(n)} \langle p \rangle_l / RT^{(n)}}{\sum_{n \in \Delta_E} w^{(n)}} \right) \tag{3.33}$$

Also considered for $\langle \rho \rangle_l$ is the particle weight density given by Eq. (3.31).

The simplest consistency check is via flow visualization. Contours of the instantaneous $\langle \rho \rangle_l$, $\langle RT \rangle_L$ and $\langle f \rangle_L$ fields are shown in Figs. 24, 26 and 28, respectively. The central jet lies in the middle along the streamwise coordinate, surrounded by the high temperature pilot where $\langle RT \rangle_L$ is the highest and $\langle \rho \rangle_l$ the lowest, and encircled by the entraining air. Due to the presence of helical instabilities, the instantaneous flow is asymmetric. The consistency is portrayed in these figures and is also observed at all other times. Contours of the time averaged fields are shown in Figs. 25, 27 and 29. The effects of numerical oscillations in FD and localized statistical error in MC are diminished by time averaging. Therefore, the averaged fields are in a closer agreement. The consistency is further assessed via comparisons of the radial profiles as shown at several axial locations in Fig. 30 for instantaneous fields, and in Fig. 31 for time averaged fields.

Complementary consistency assessments are made by constructing the scatter plots of the instantaneous and the time averaged values. These are shown at four adjacent segments of the computational domain. The instantaneous MC density, $\langle \rho \rangle^{\mathrm{MC}}$, is highly correlated with the fluid filtered density, as Fig. 32 shows. This figure also shows close correlation of $\langle RT \rangle_L$ and $\langle f \rangle_L$ from the FD and the MC solvers. Note that, due to numerical oscillations, the FD passive scalar violates the realizability (unless an artificial limiter is employed), but the MC predictions always remain bounded. Scatter plots of the time averaged values are shown in Fig. 33. The increase in coherence of the time averaged quantities is obvious.

3.4.3 Reacting Flow

The centerline mean velocity and turbulent kinetic energy are compared with experimental data in Fig. 34. Compared to the non-reacting case, the turbulent kinetic energy is nearly constant along the axial direction and so is the maximum velocity at the centerline. This

indicates that the potential core is significantly longer in the reacting case and the flow is not excited until further downstream. As Fig. 35 shows, the radial profiles of the axial velocity are much broader in comparison with that in the cold-flow (see Fig. 23), and the shear layer spreads further. This is due to the effects of volumetric expansion due to exothermicity. LES/FDF capture these effects well, as the predicted values are in good agreement with data, except that the potential core as estimated by LES/FDF is somewhat longer than that in the measurements.

The radial distribution of the mean temperature is shown to compare well with data in Fig. 36. The overprediction at the near field by ≈ 150K is due to the neglect of heat losses to the burner surface. As the measured profiles indicate, the centerline mean temperature increases starting at roughly $x/d = 4.5$. This is due to the fact that the unsteady flame crosses the centerline at certain instants resulting in the increase in the mean temperature. Herrman[106] points out that in the RANS approach, such large scale fluctuations are not adequately taken into account, and in fact the centerline temperature is predicted to be constant at the unburnt temperature. LES/FDF is able to resolve these instabilities, and reproduce the correct behavior.

The statistics of the mass fractions of species for which measurements are available are compared with data. Figure 37 shows radial profiles of the mean CH_4 and O_2 mass fractions. The near field predicted results compare well with the data. At $x/d = 4.5$, the estimated location of the shear layer where the hot pilot and cold reactants mix is offset by $0.1d$, but the gradient is captured well. Due to the large velocity difference between the jet and pilot streams, there is a strong entrainment of hot pilot gas into the main jet. This is observed via the radial expansion of the reactant profiles along the streamwise direction, an effect which is portrayed well by the predictions. The outer air is also entrained into the flame above an axial position called the mixing layer height between pilot and air, L_i. Detailed measurements are not available for $r/d > 1.2$, but it is reported in the experiments[68] that $L_i = 5d$ and it is suggested that entrainment of cool air can be excluded below this axial location. This entrainment effect and the mixing layer height are captured by the computations where the O_2 profile is flat at $x/d = 2.5$ and outer layer profiles slightly increase downstream. The CO_2 and H_2O mass fraction profiles are shown in Fig. 38. The shear layer offset at $x/d = 4.5$ is

more pronounced in the predicted mass fractions of CO_2 and H_2O, and the CO_2 values are slightly underpredicted at $x/d = 6.5$, but the overall agreement is good.

Figure 39 shows the comparison of the CO and OH mass fraction profiles with data. At the jet/pilot mixing layer, the CO levels are overpredicted by a factor of 2 in the nearfield and 1.5 downstream. After an initial maximum, the CO levels decrease strongly until $x/d = 4.5$ then the radial profiles assume smaller gradients. This effect is captured well by the simulation. The OH levels are strongly influenced by the temperature, and the apparent overprediction of temperature upstream at $x/d = 2.5$ is responsible for the OH profiles with higher peak at this location. Further downstream the temperature levels are predicted correctly, thus the simulated OH profiles agree favorably with the measurements.

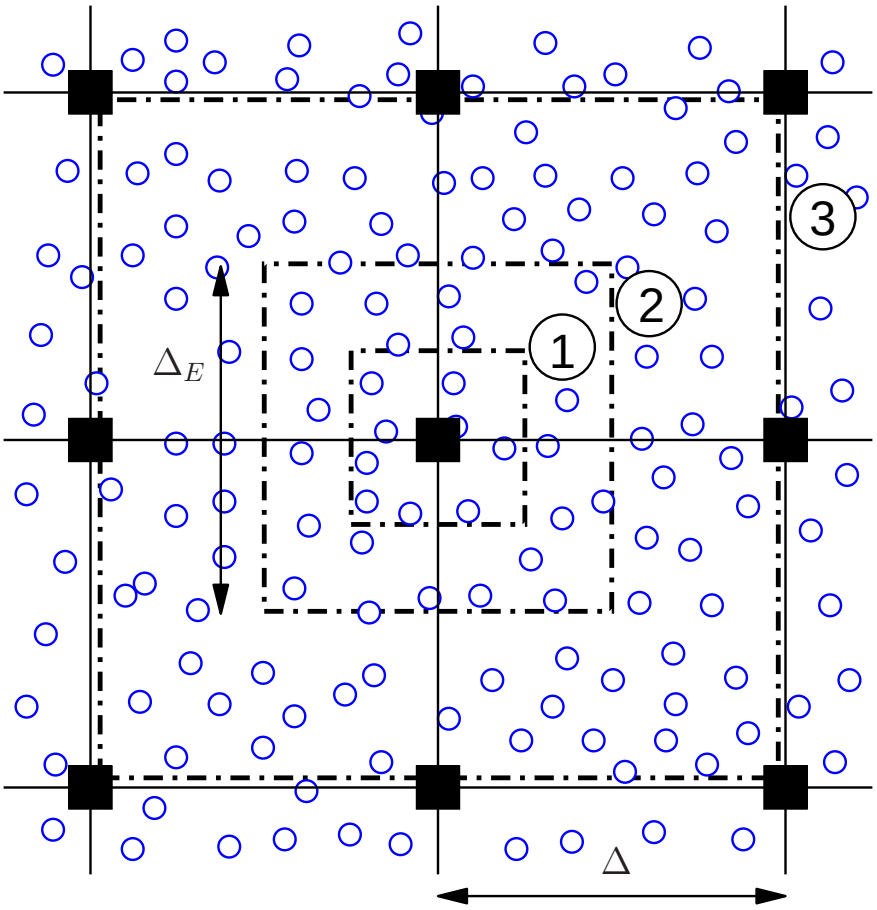

Figure 14: Element of computation as used in hybrid simulations. Solid squares denote grid locations of the FD or FV mesh, and the circles denote the MC particles. Also shown are three different ensemble domains.

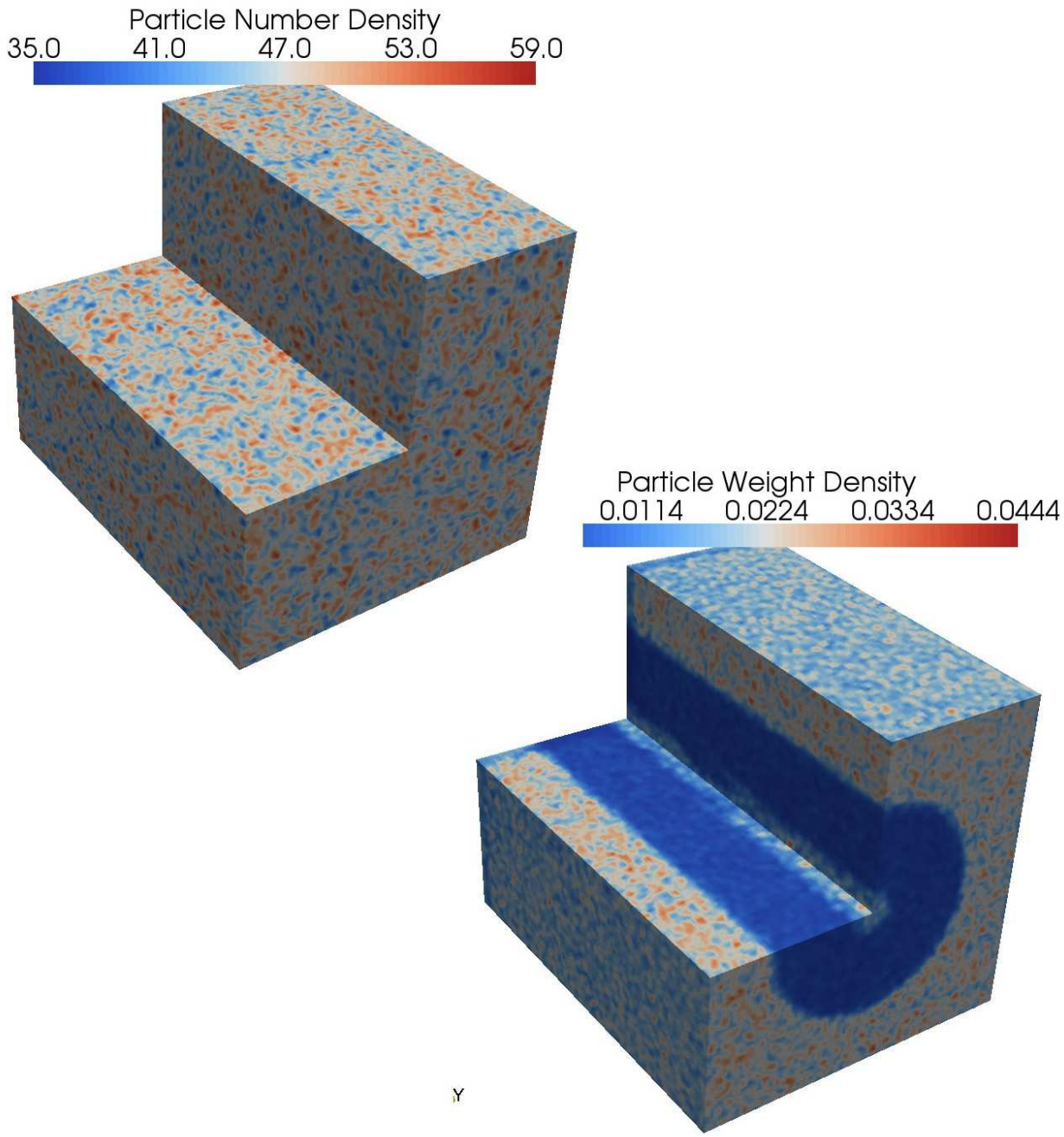

Figure 15: Contours of the instantaneous particle number density (top-left) and ensemble particle weights (bottom-right) in the MC solver.

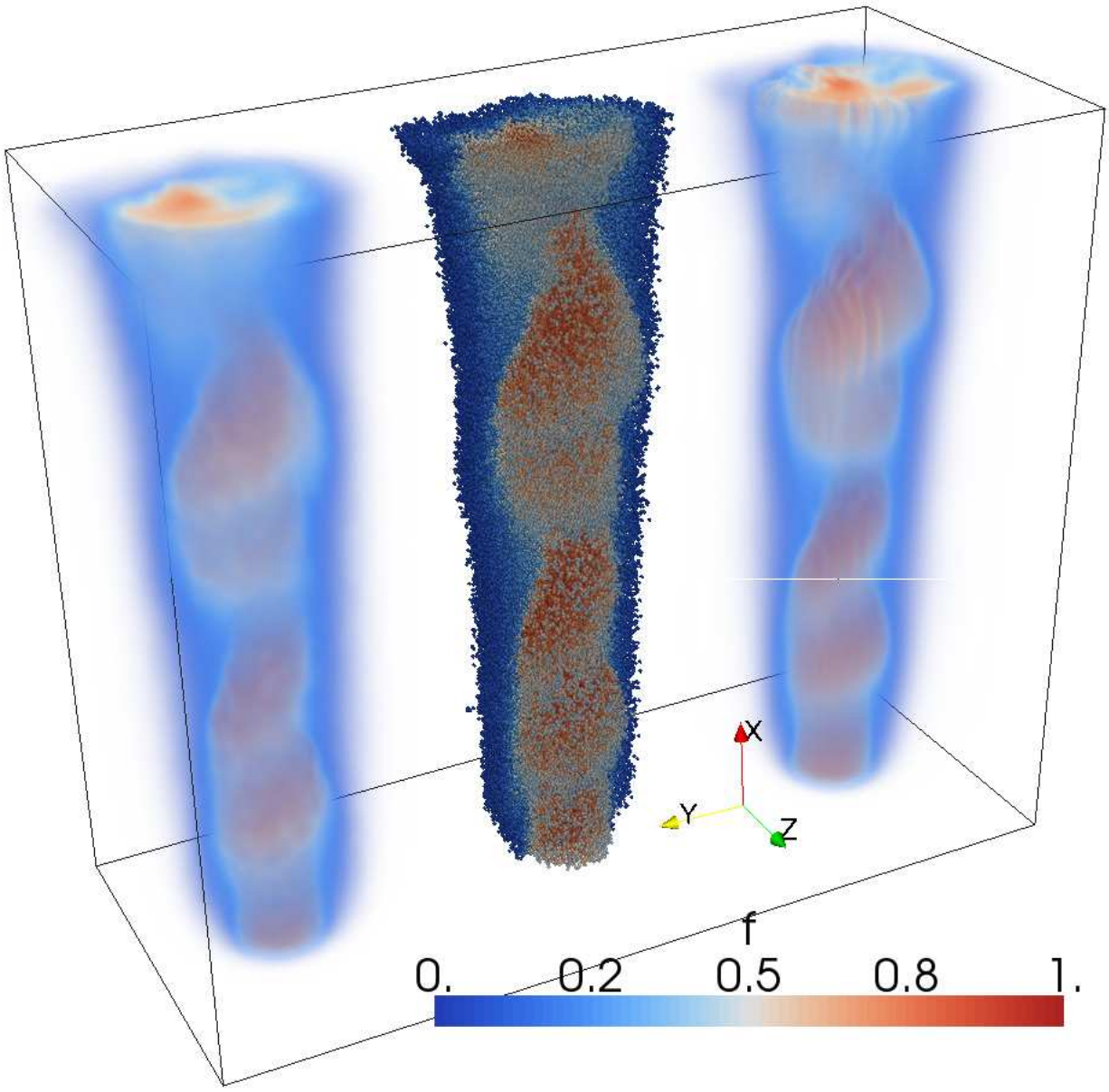

Figure 16: Conserved scalar fields obtained by (left) ensemble averaged MC, (middle) MC particles (colored according to f^+), (right) FD.

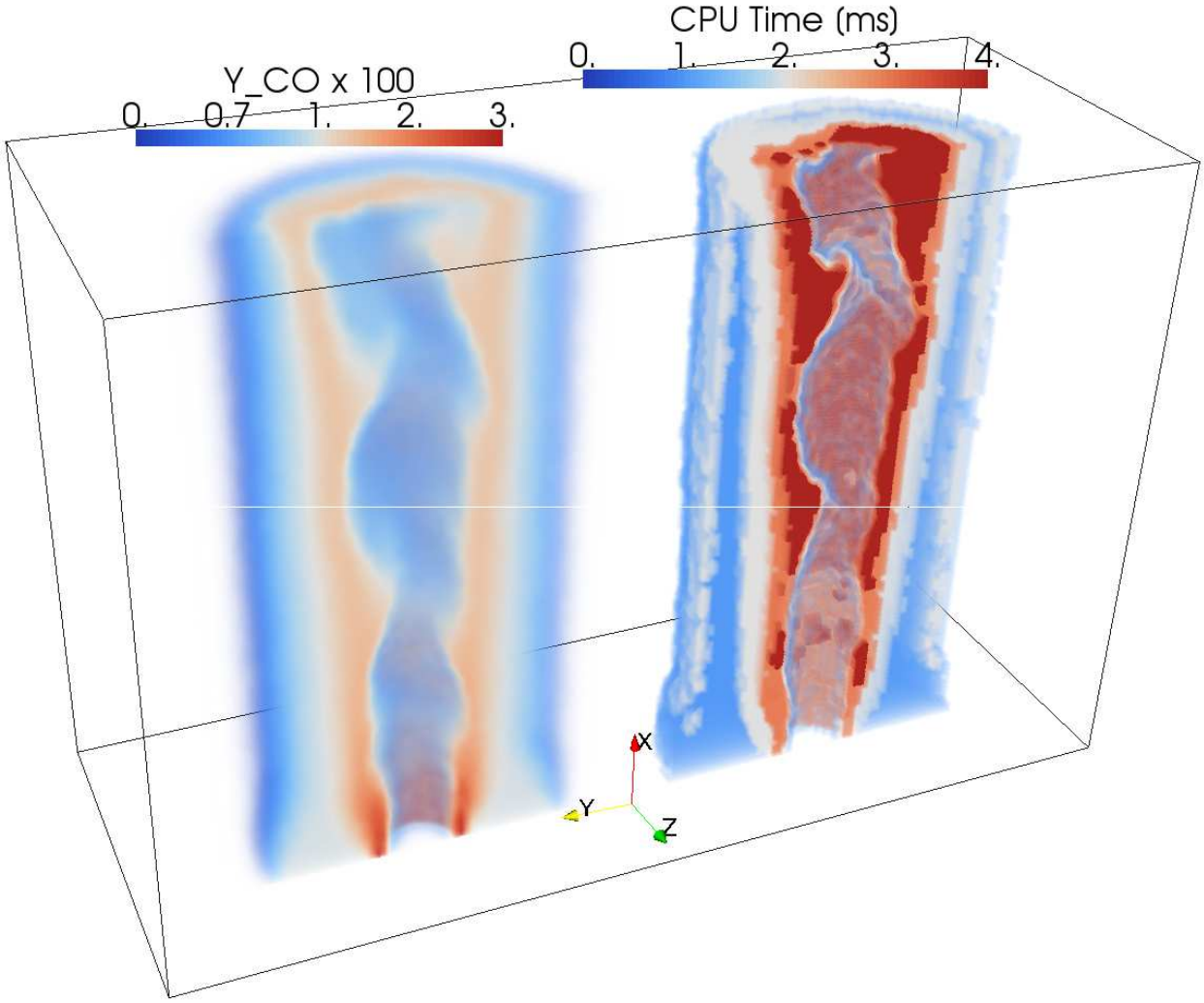

Figure 17: Instantaneous distribution of CPU requirements in the LES/FDF solver. (Left) filtered CO mass fraction field, (right) CPU time in milliseconds spent during particle computations. Transparent regions (no colors) indicate negligible computation.

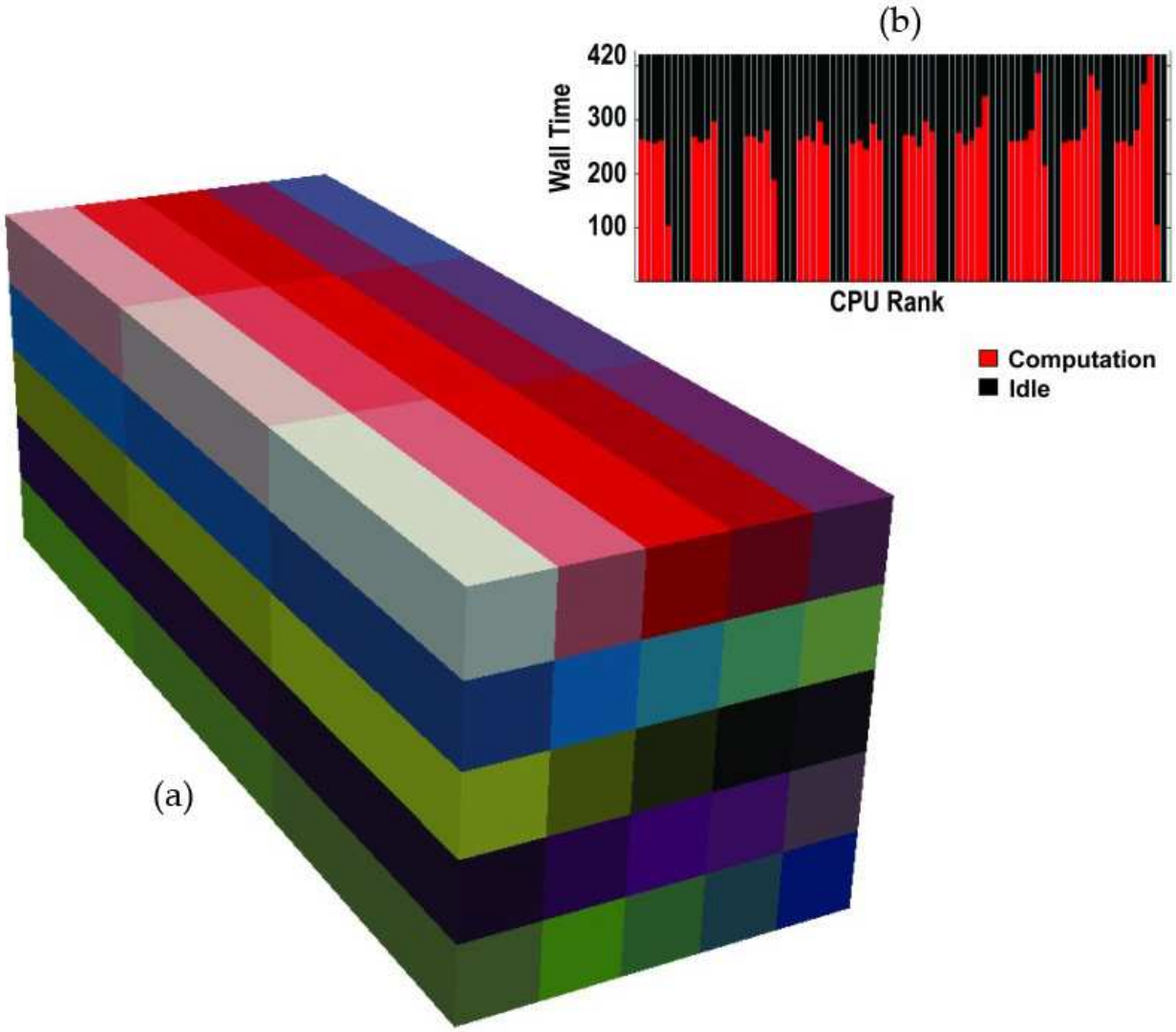

Figure 18: (a) Domain boundaries in the uniform decomposition. Each color indicates a separate domain. (b) Total computational time per CPU. Red color indicates active computation, black color indicates idle time.

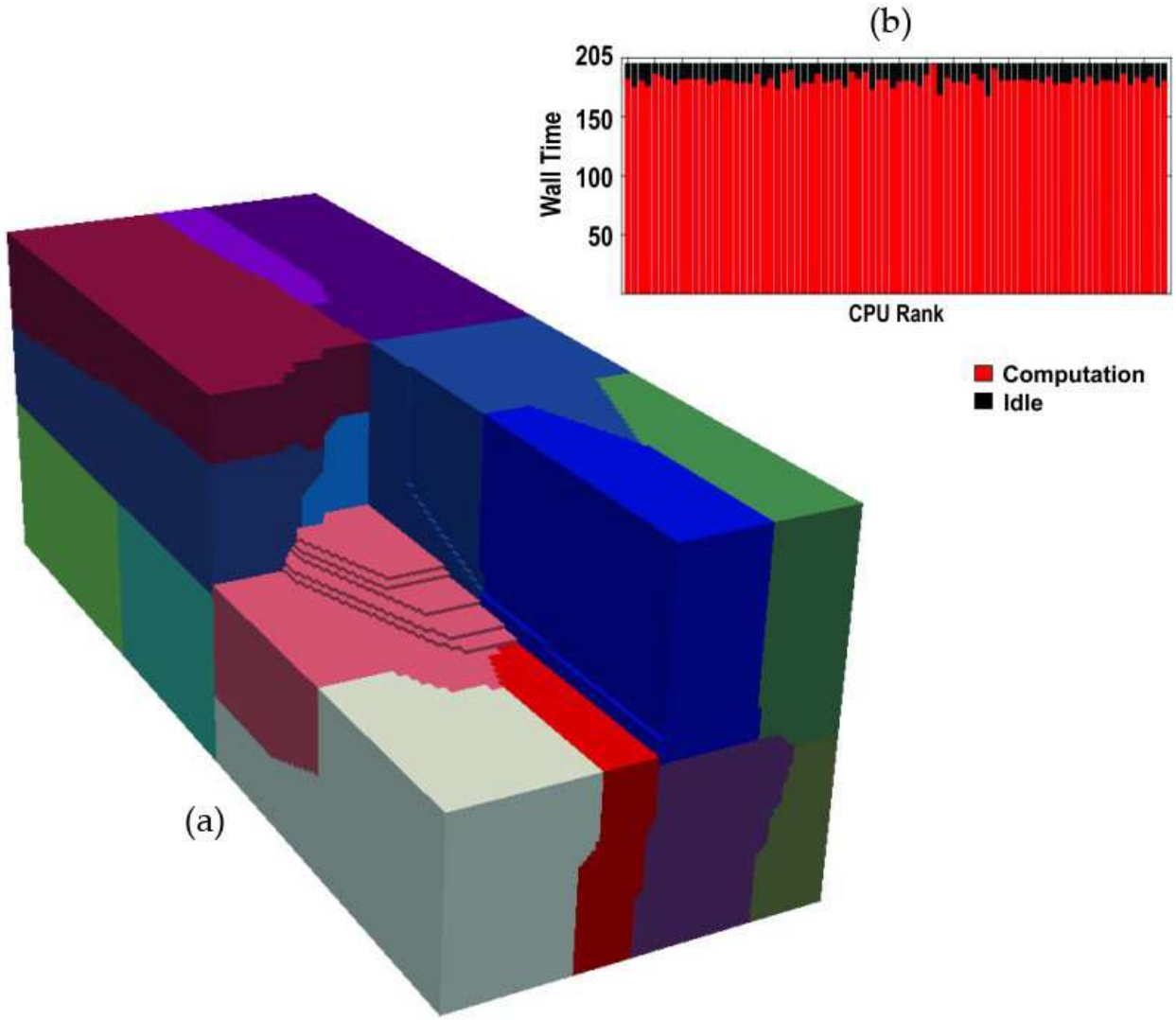

Figure 19: (a) Domain boundaries in the adaptive decomposition. (b) Total computational time per domain. Red color indicates active computation, black color indicates idle time.

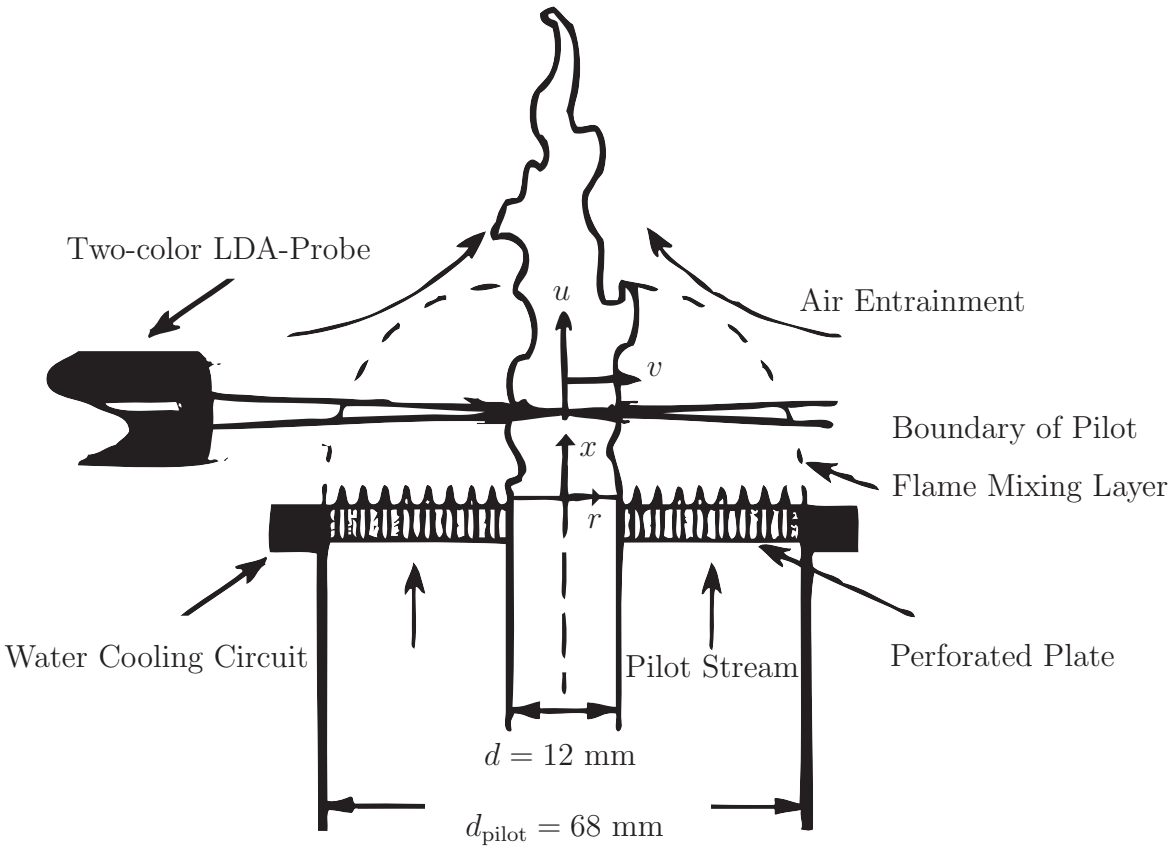

Figure 20: Schematic diagram of the Bunsen burner configuration.[68]

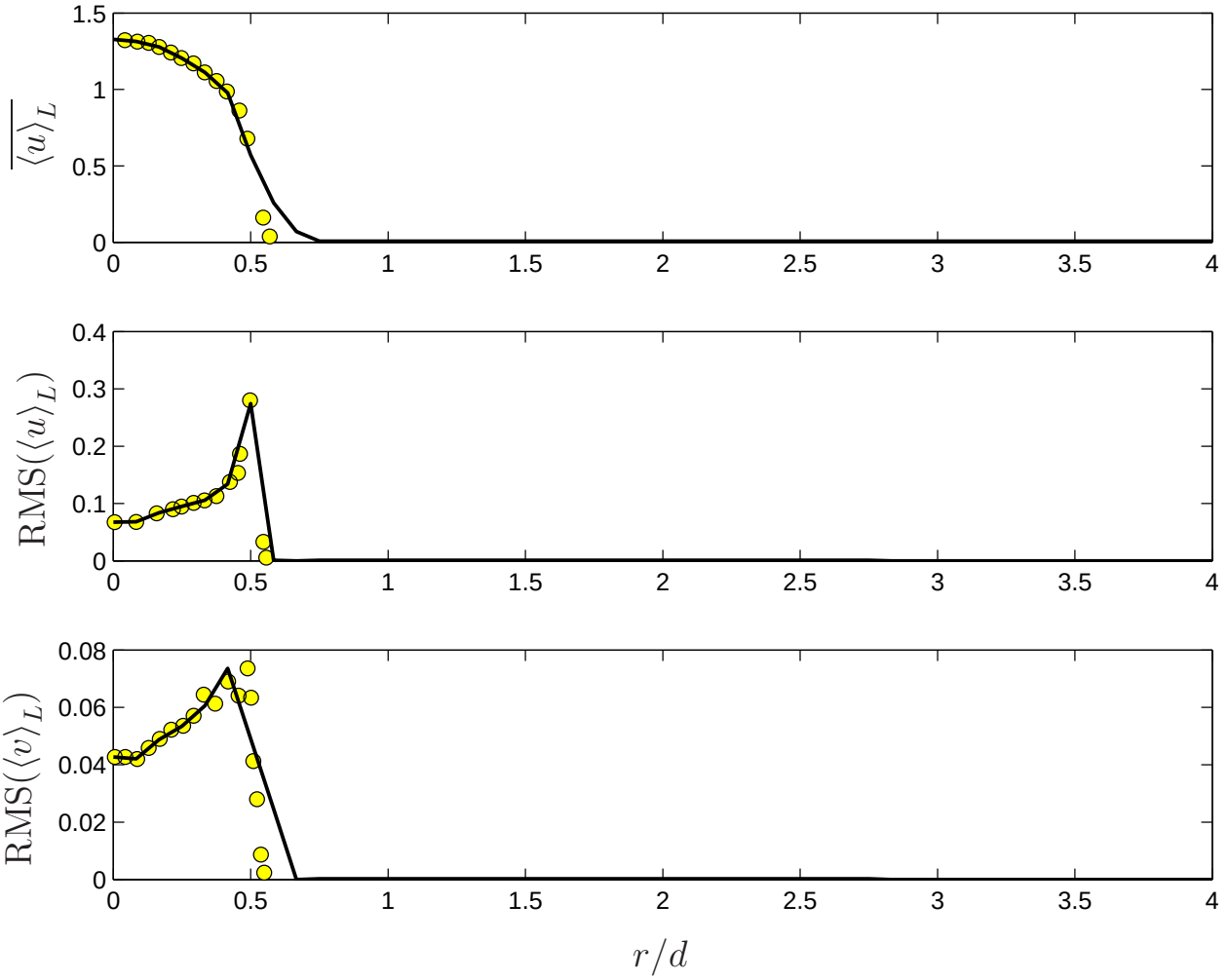

Figure 21: Bunsen burner: Radial profiles of the mean and the rms axial velocity at the inlet.

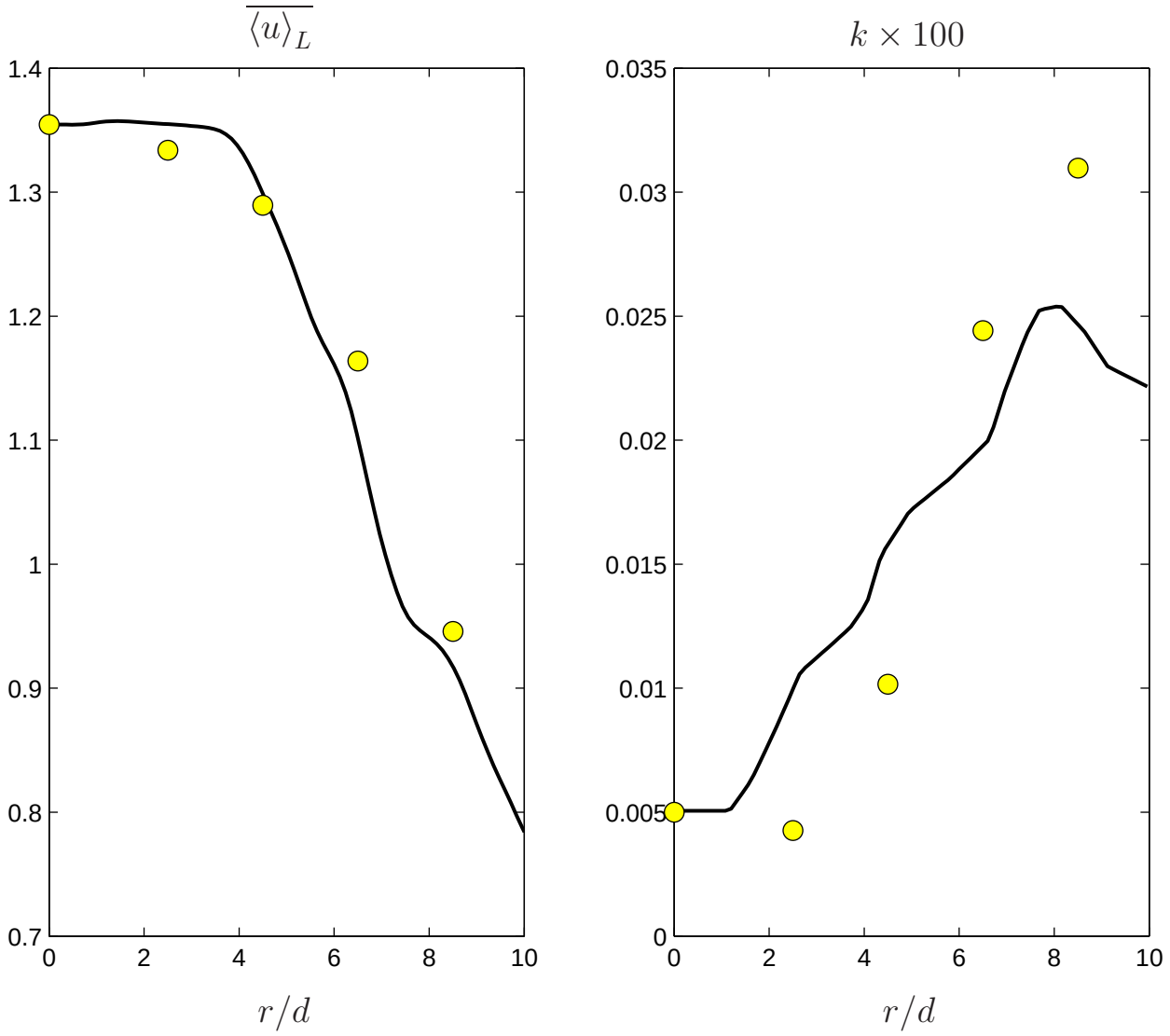

Figure 22: Bunsen burner, cold flow: Variation of the mean axial velocity and the turbulent kinetic energy along the axial direction at the centerline. — LES, ○ Experimental measurements.[68]

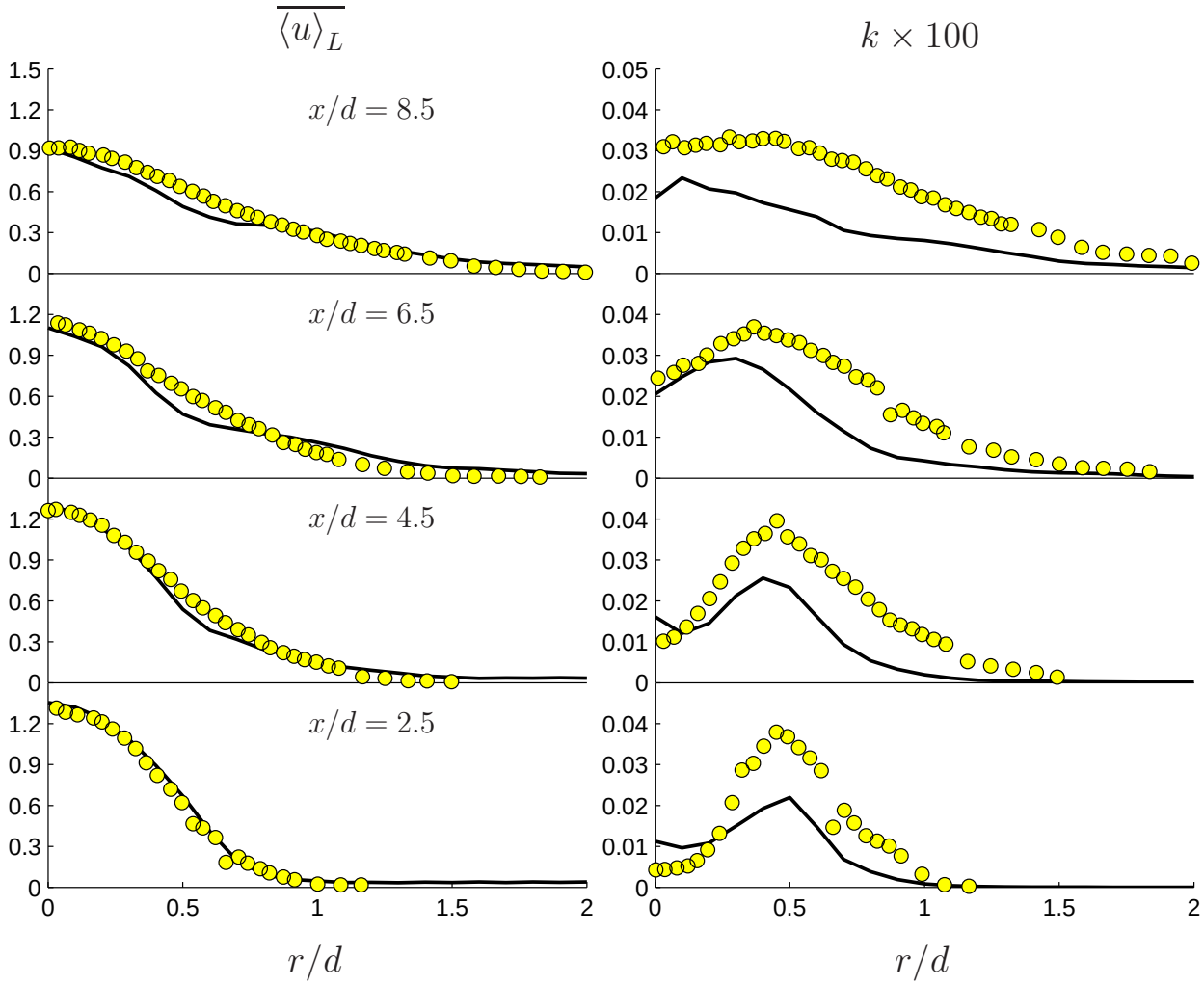

Figure 23: Bunsen burner, cold flow: Radial profiles of the mean axial velocity and the turbulent kinetic energy. — LES, ○ Experimental measurements.[68]

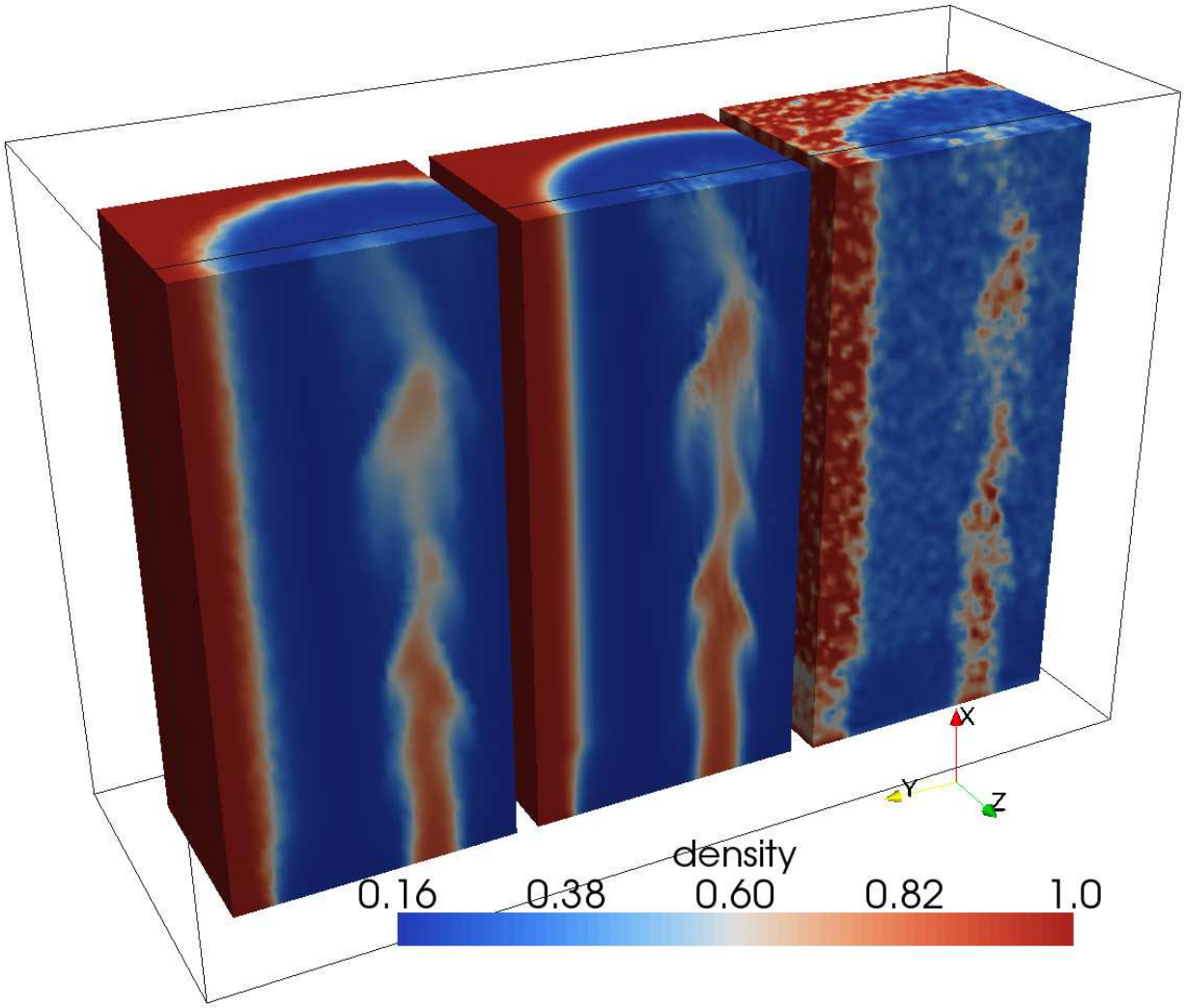

Figure 24: Bunsen burner, reacting flow: Contours of the instantaneous $\langle \rho \rangle_l$ field as obtained from (left) MC density as given by Eq. (3.33), (middle) FD, and (right) MC particle weight density as given by Eq. (3.31).

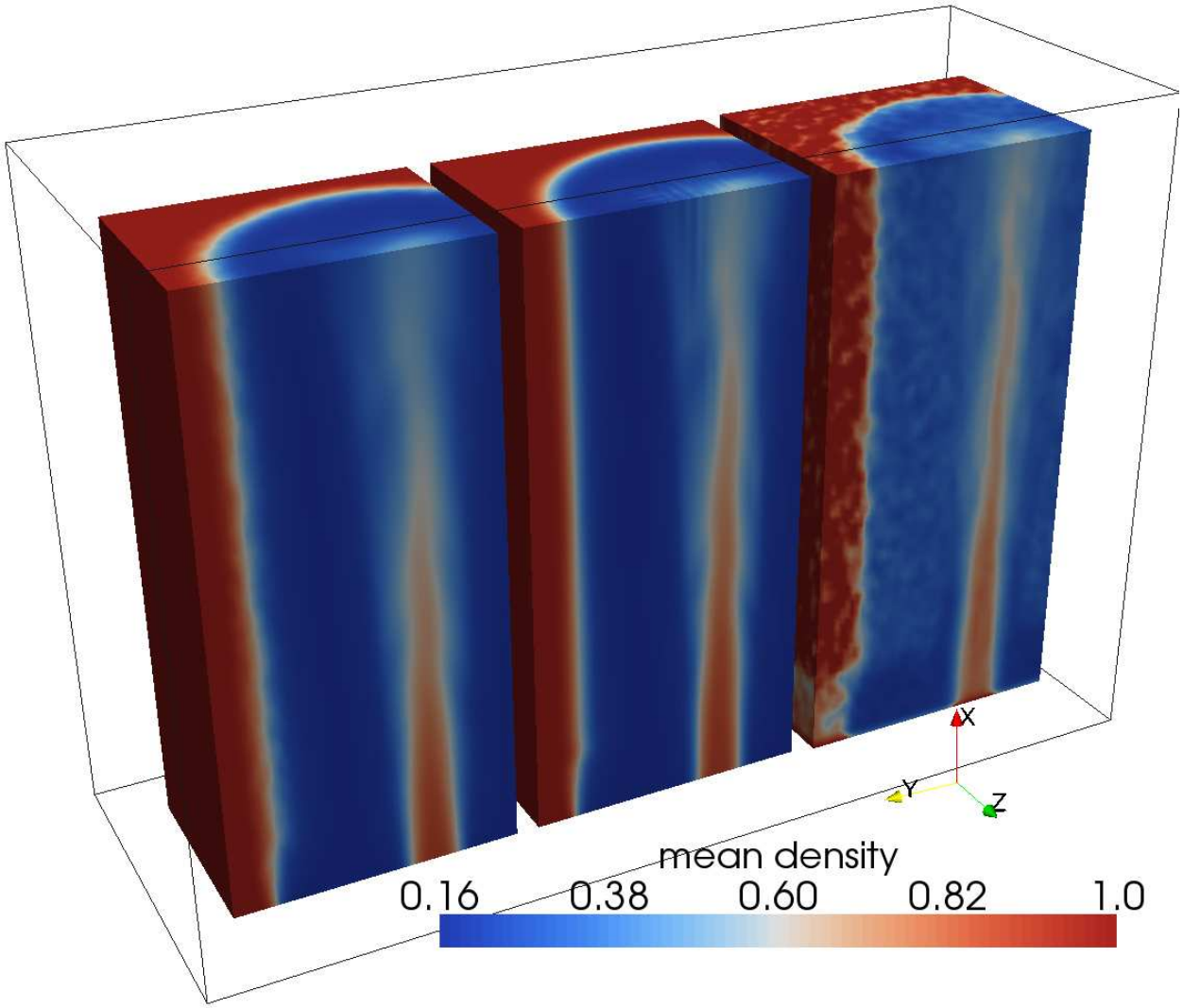

Figure 25: Bunsen burner, reacting flow: Contours of the time averaged $\overline{\langle \rho \rangle_l}$ field as obtained from (left) MC density as given by Eq. (3.33), (middle) FD, and (right) MC particle weight density as given by Eq. (3.31).

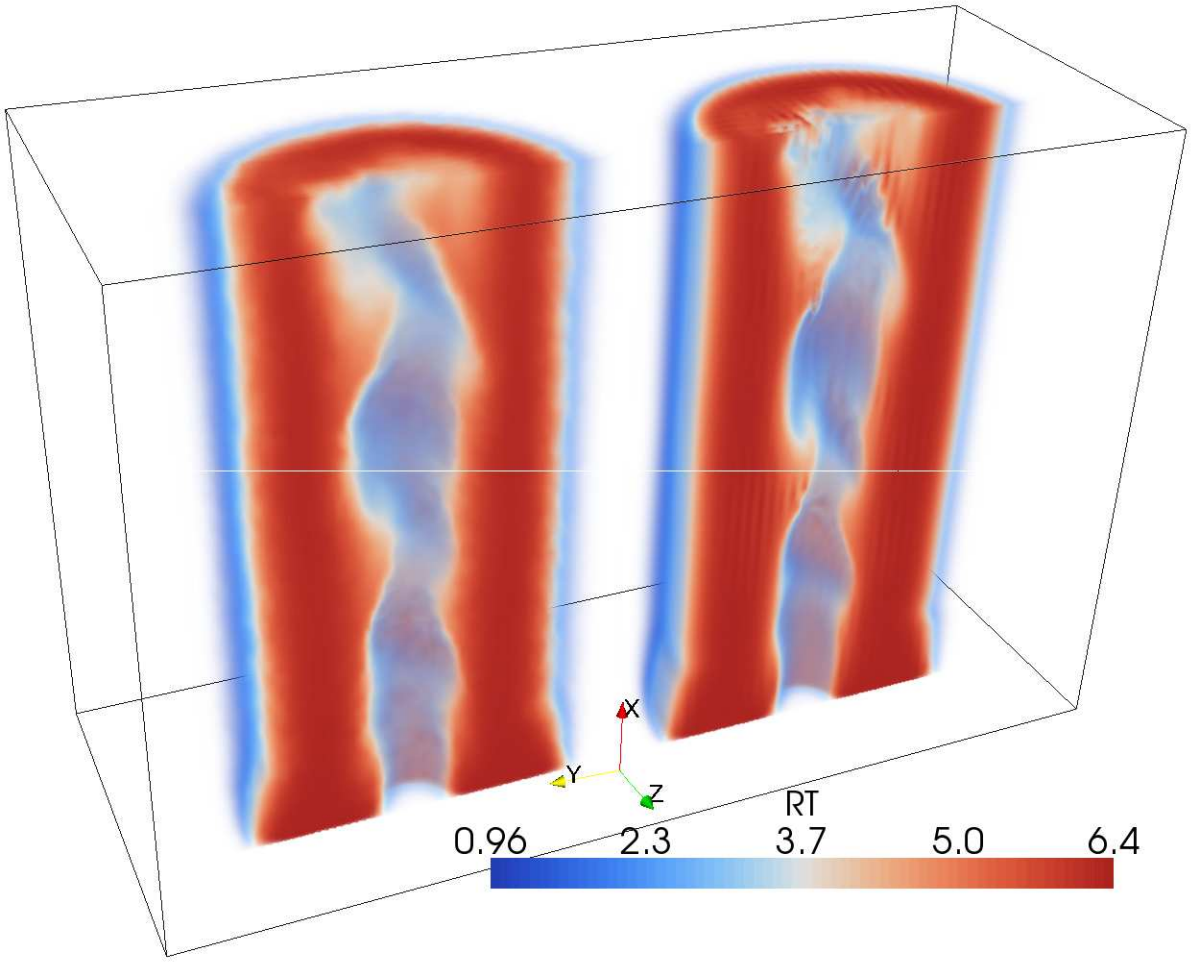

Figure 26: Bunsen burner, reacting flow: The instantaneous $\langle RT \rangle_L$ field as obtained from MC (left) and FD (right).

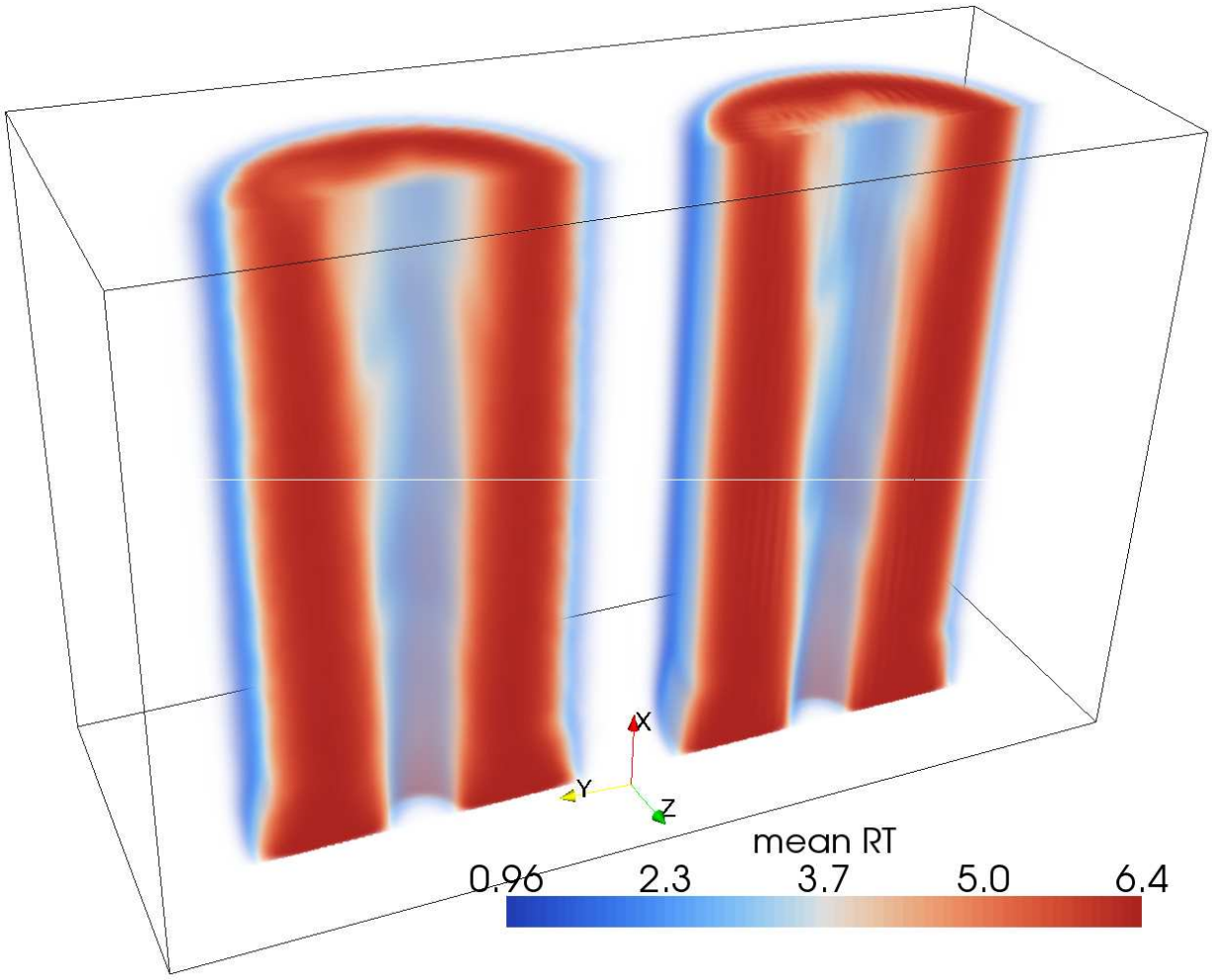

Figure 27: Bunsen burner, reacting flow: The time averaged $\overline{\langle RT \rangle_L}$ field as obtained from MC (left) and FD (right).

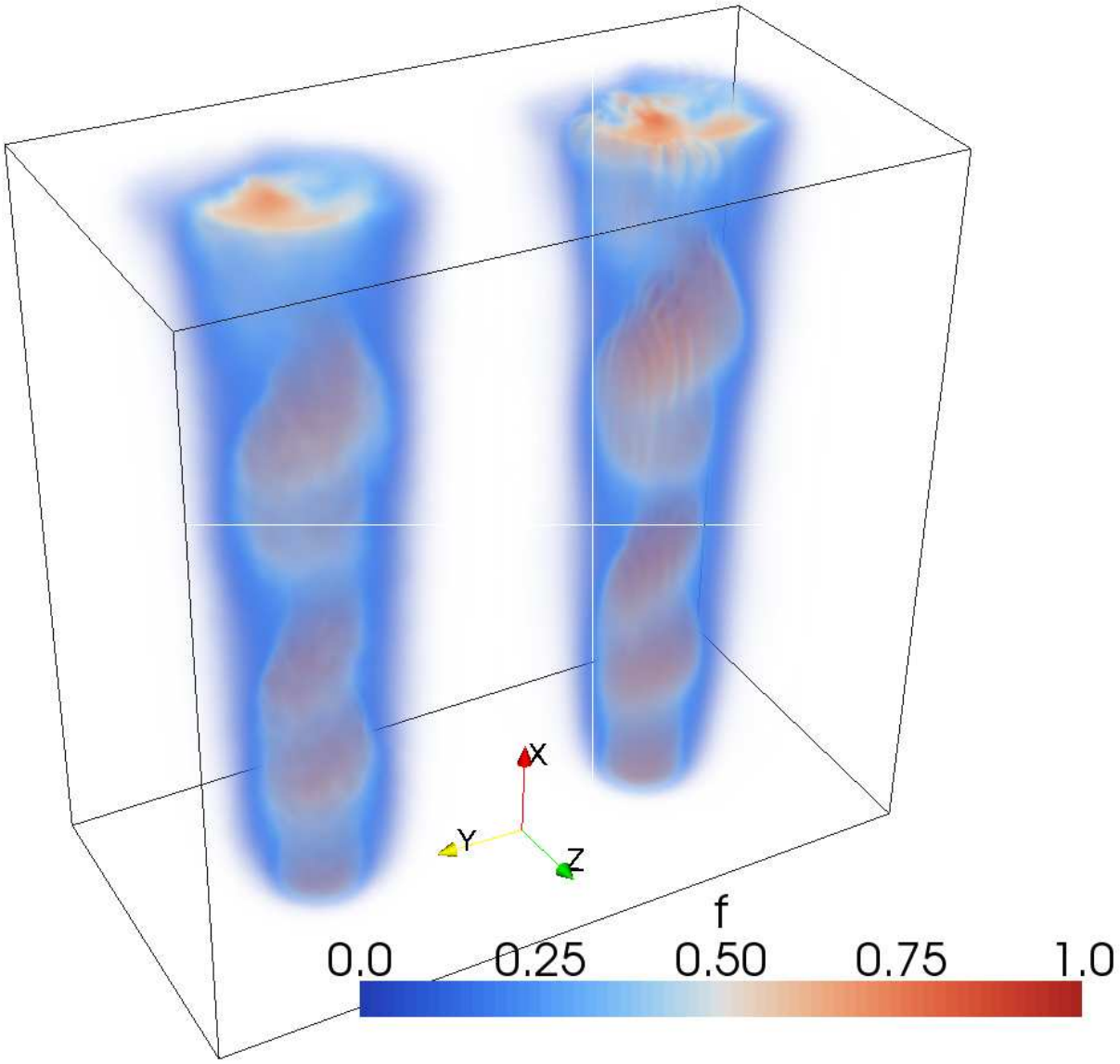

Figure 28: Bunsen burner, reacting flow: The instantaneous $\langle f \rangle_L$ field as obtained from MC (left) and FD (right).

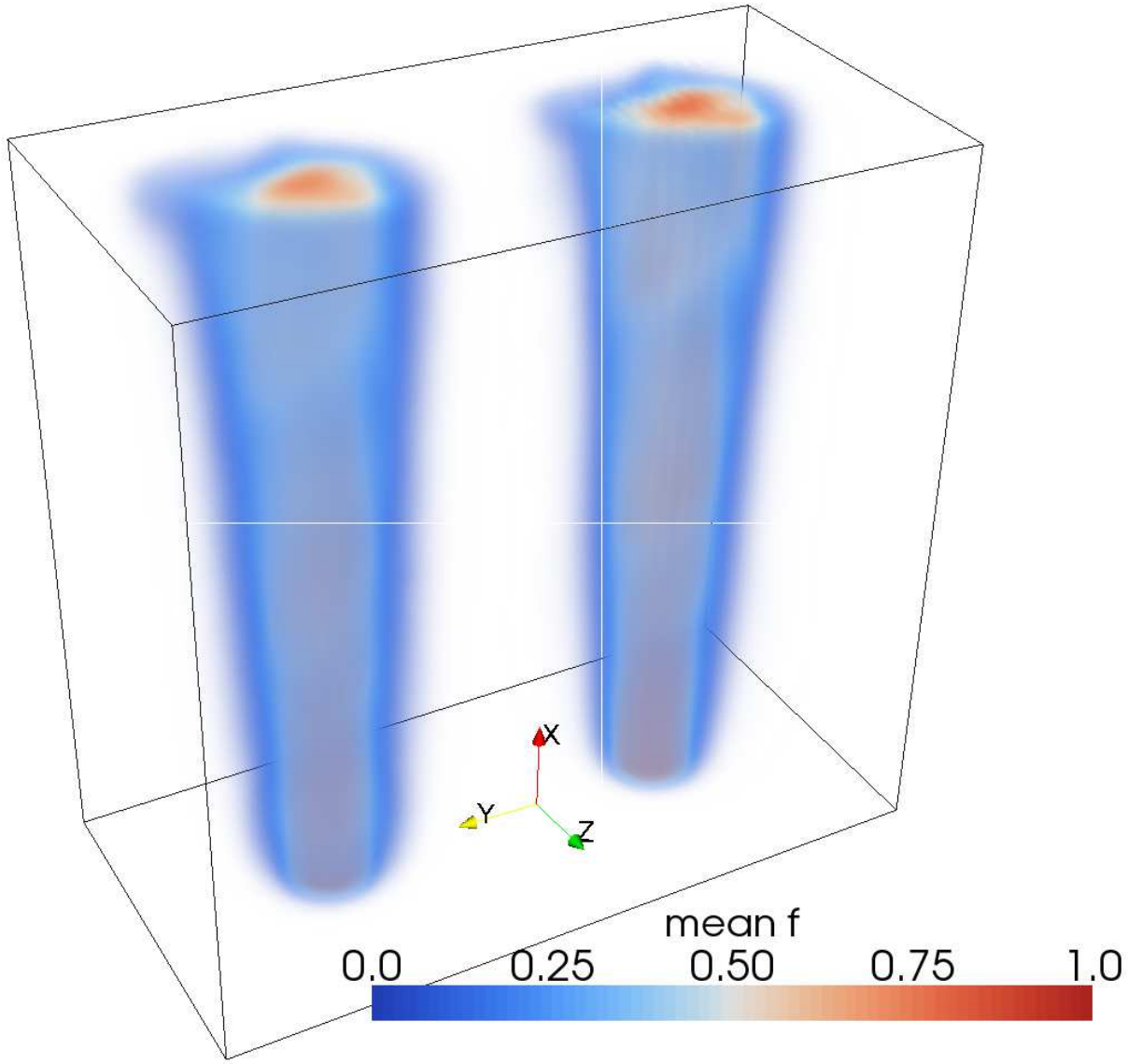

Figure 29: Bunsen burner, reacting flow: Contours of the time averaged $\overline{\langle f \rangle_L}$ field as obtained from MC (left) and FD (right).

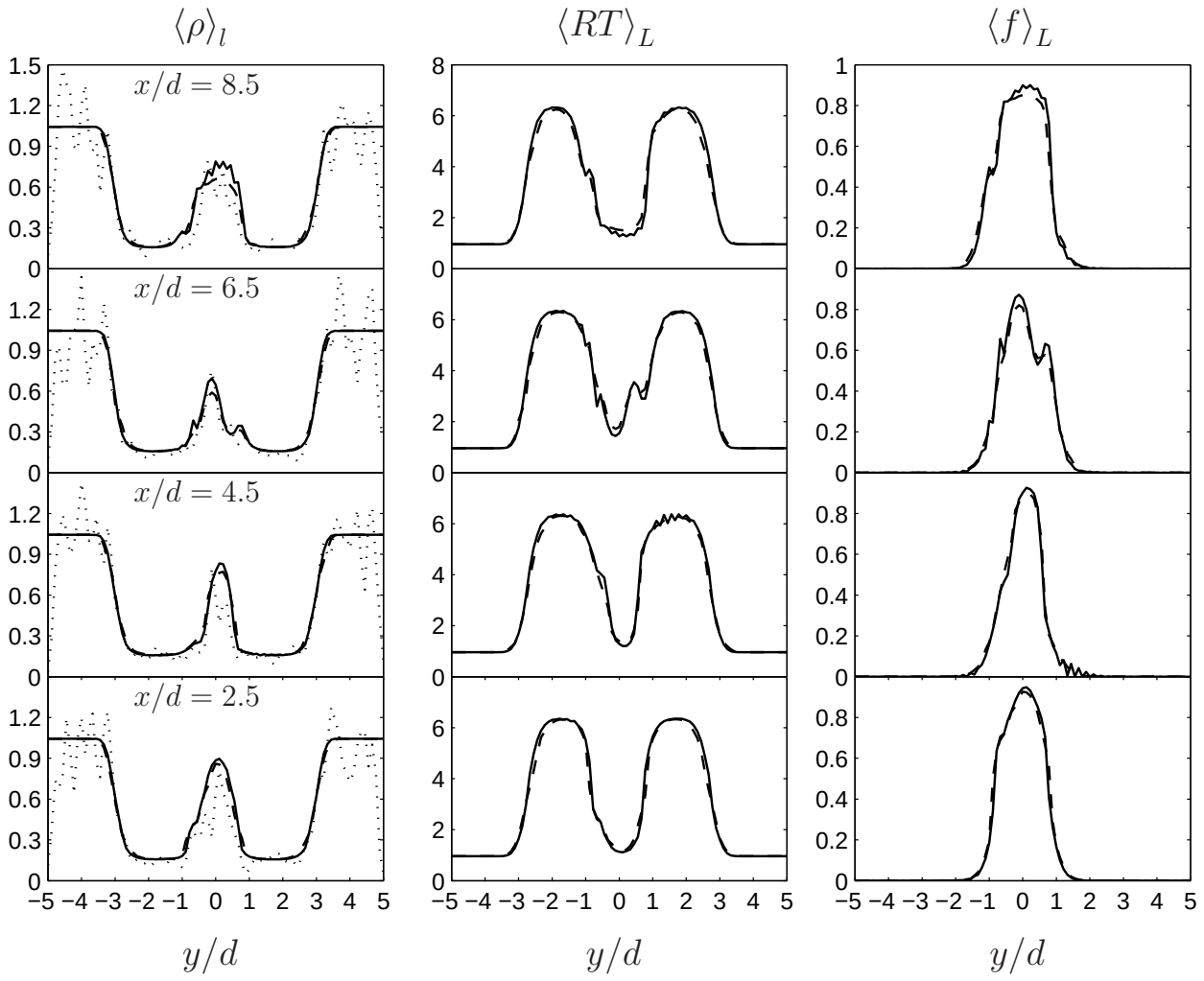

Figure 30: Bunsen burner, reacting flow: Radial profiles of the instantaneous $\langle\rho\rangle_l$, $\langle RT\rangle_L$ and $\langle f\rangle_L$ fields as obtained from FD and MC solvers. — FD, – – MC, ····MC density as given in Eq. (3.33)

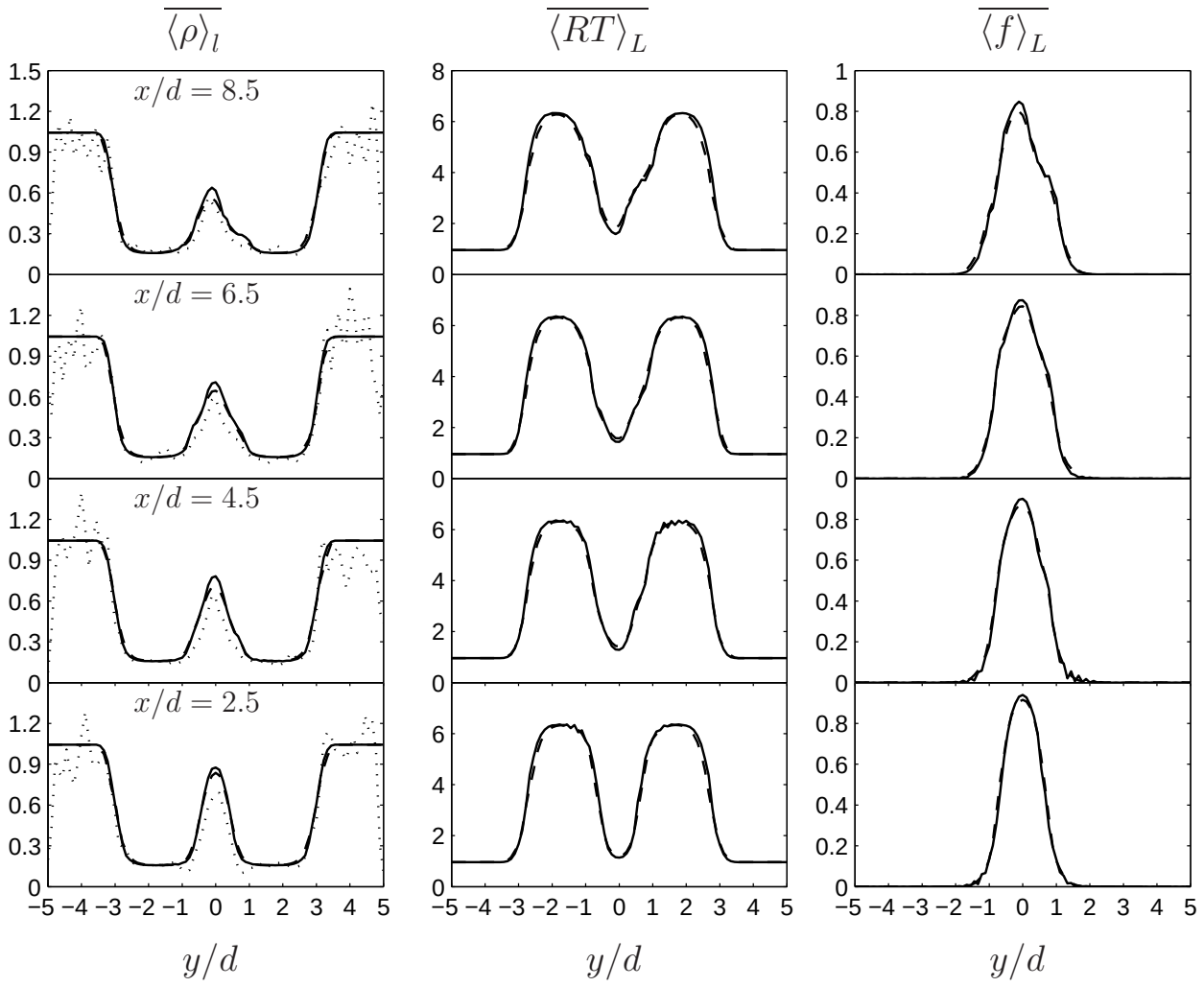

Figure 31: Bunsen burner, reacting flow: Radial profiles of the time averaged $\overline{\langle\rho\rangle_l}$, $\overline{\langle RT\rangle_L}$ and $\overline{\langle f\rangle_L}$ fields as obtained from FD and MC solvers. — FD, – – MC, ····MC density as given in Eq. (3.33)

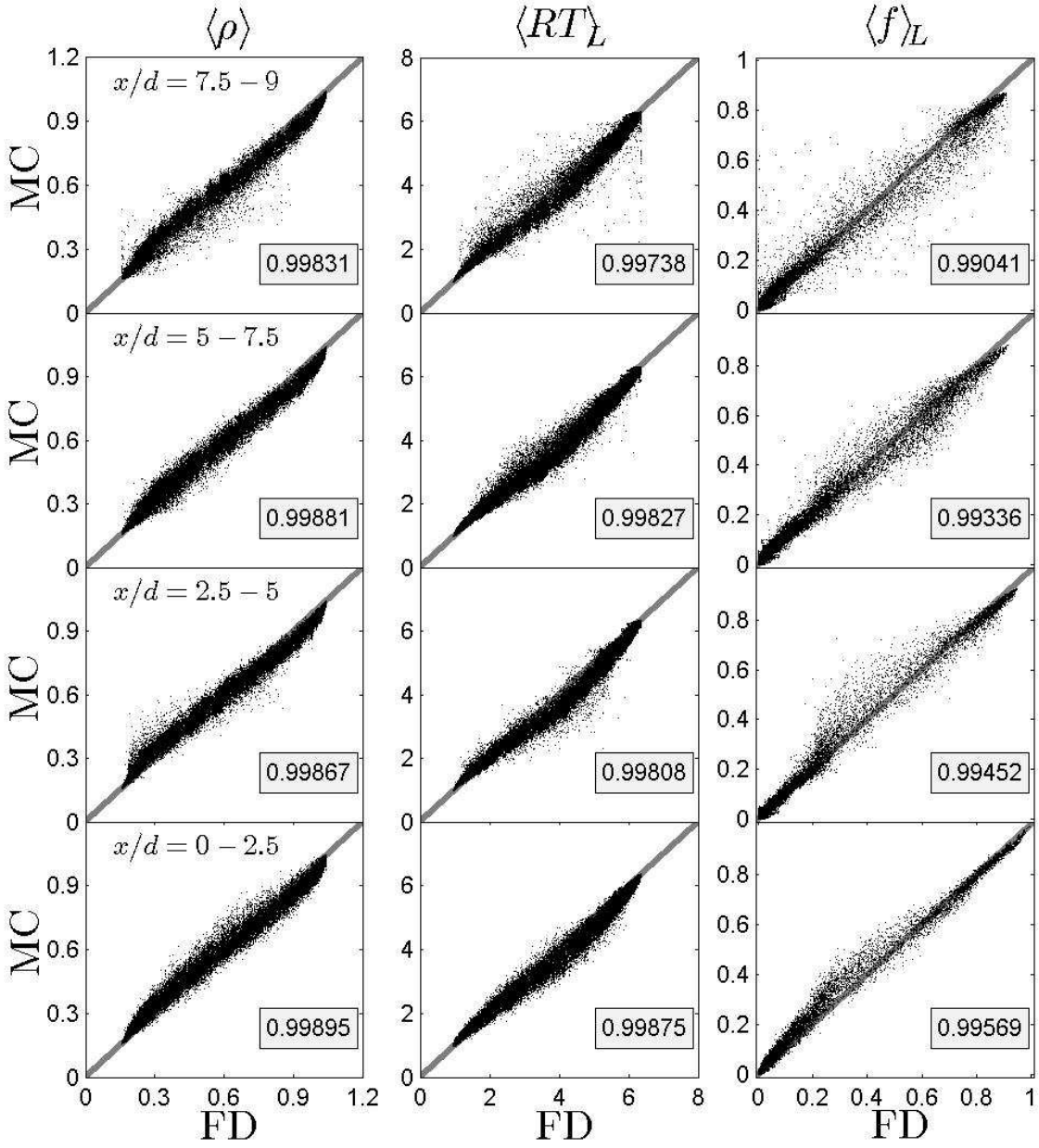

Figure 32: Bunsen burner, reacting flow: Scatter plots of the instantaneous $\langle\rho\rangle_l$, $\langle RT\rangle_L$ and $\langle f\rangle_L$ fields as obtained from FD and MC solvers. The correlation coefficient is displayed on bottom right of each figure.

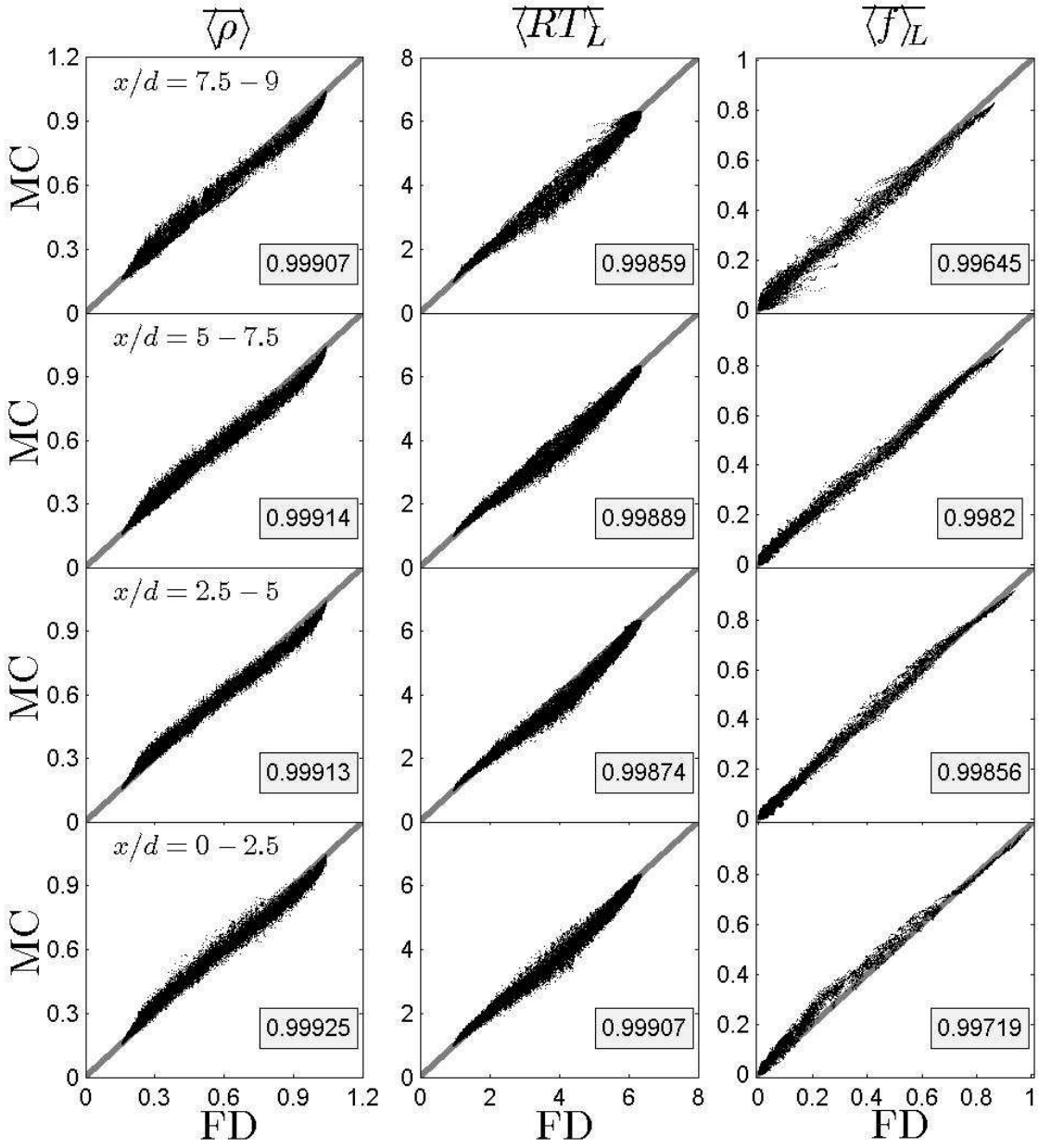

Figure 33: Bunsen burner, reacting flow: Scatter plots of the time averaged $\overline{\langle\rho\rangle_l}$, $\overline{\langle RT\rangle_L}$ and $\overline{\langle f\rangle_L}$ fields as obtained from FD and MC solvers. The correlation coefficient is displayed on bottom right of each figure.

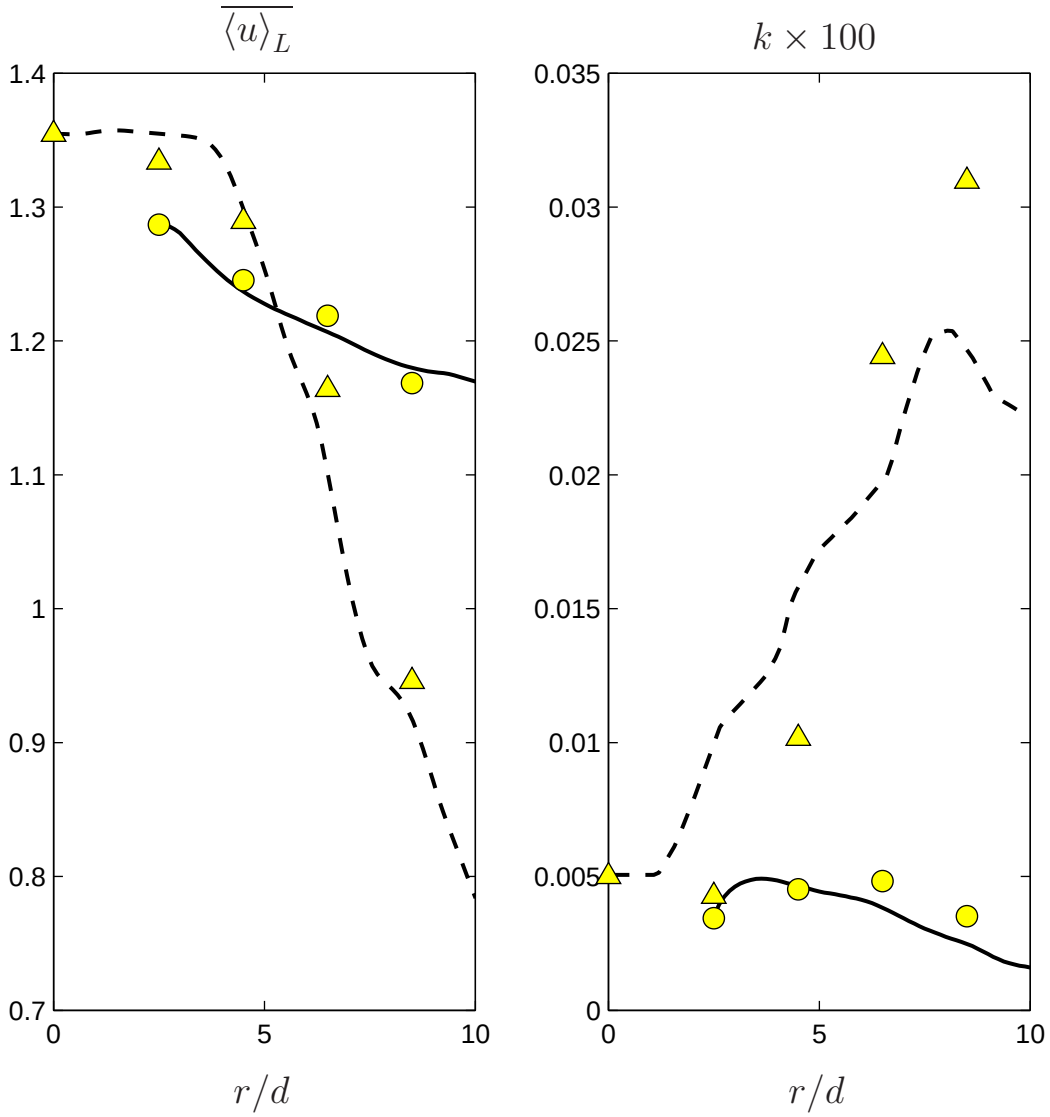

Figure 34: Bunsen burner: Streamwise variation of the mean axial velocity and the turbulent kinetic energy at the centerline. Also shown are the results from the cold flow in Fig. 22. — LES/FDF, ○ Experimental measurements.[68] – – LES of the cold flow, △ Experimental measurements of the cold flow.[68]

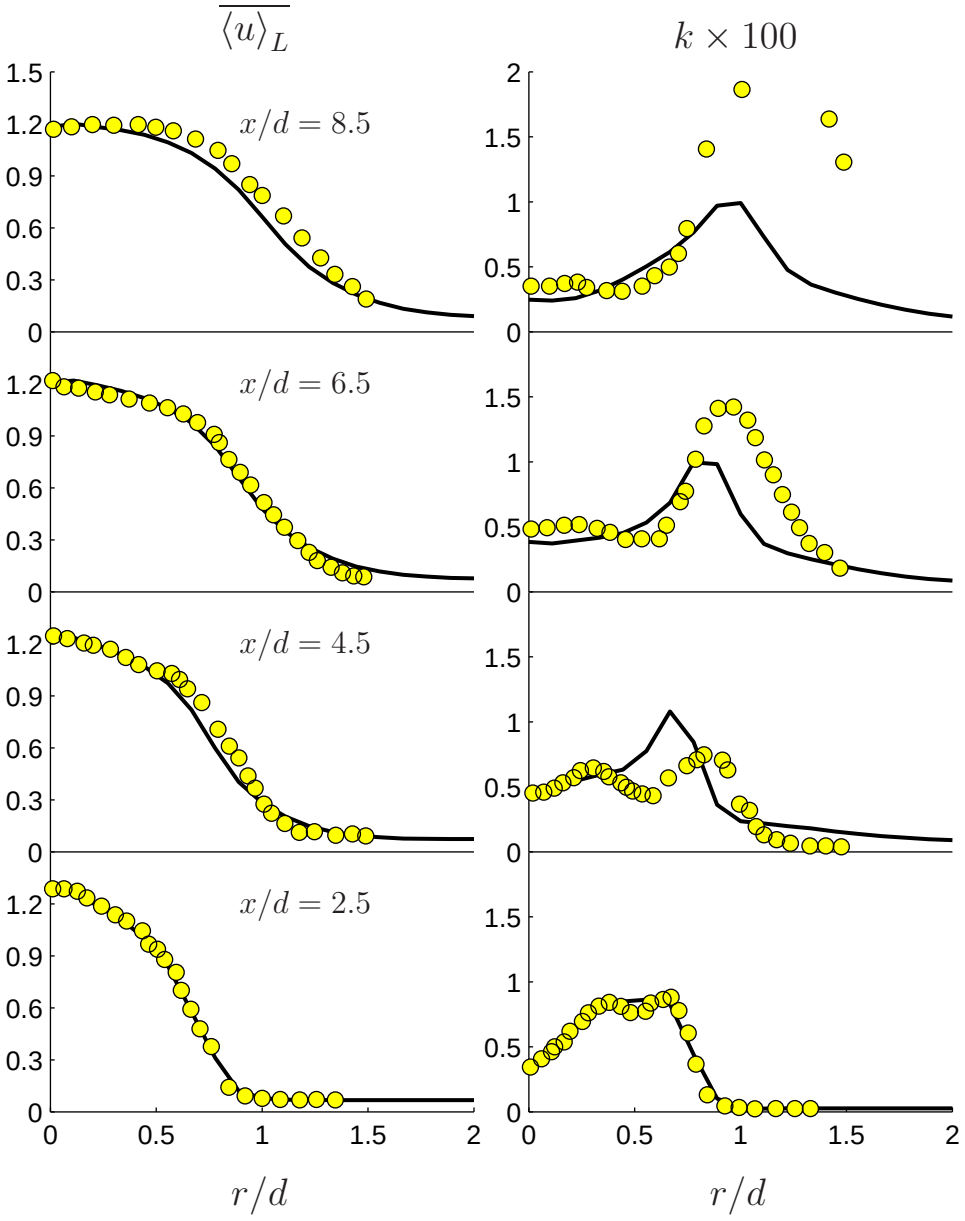

Figure 35: Bunsen burner, reacting flow: The radial profiles of the mean axial velocity and the turbulent kinetic energy. — LES/FDF, ● Experimental measurements.[68]

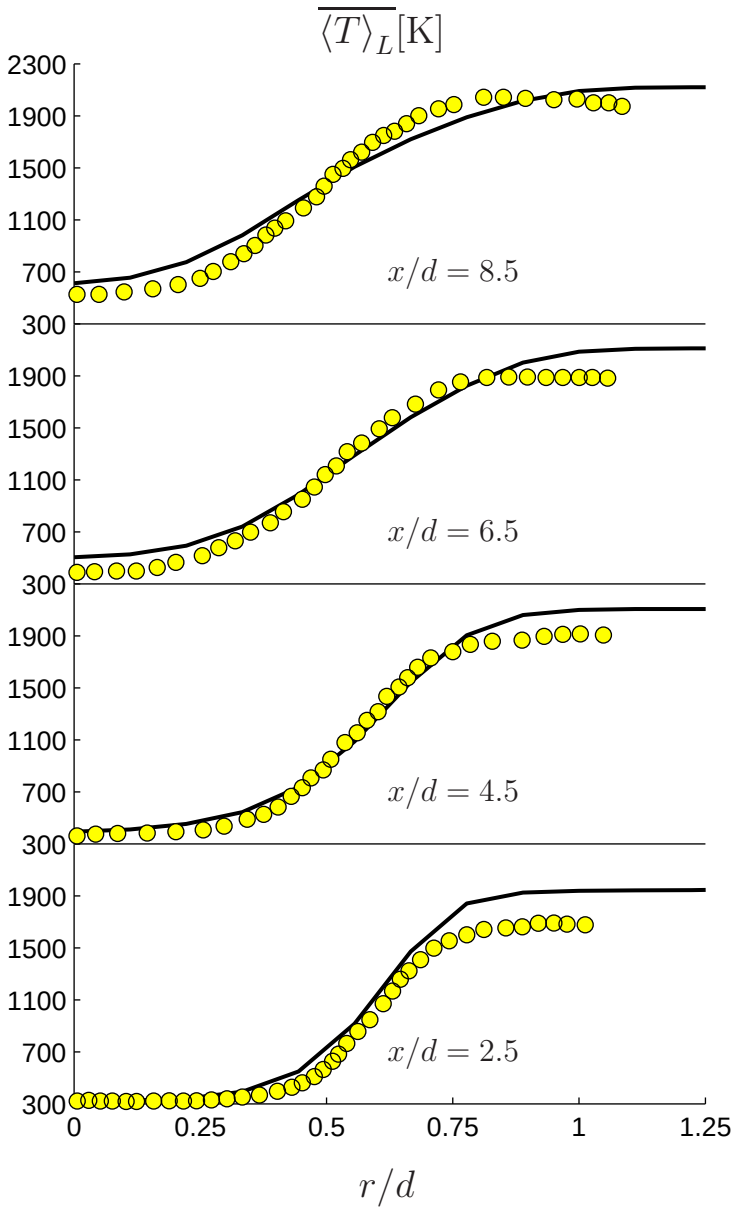

Figure 36: Bunsen burner, reacting flow: The radial profiles of the mean temperature. — LES/FDF, ● Experimental measurements.[68]

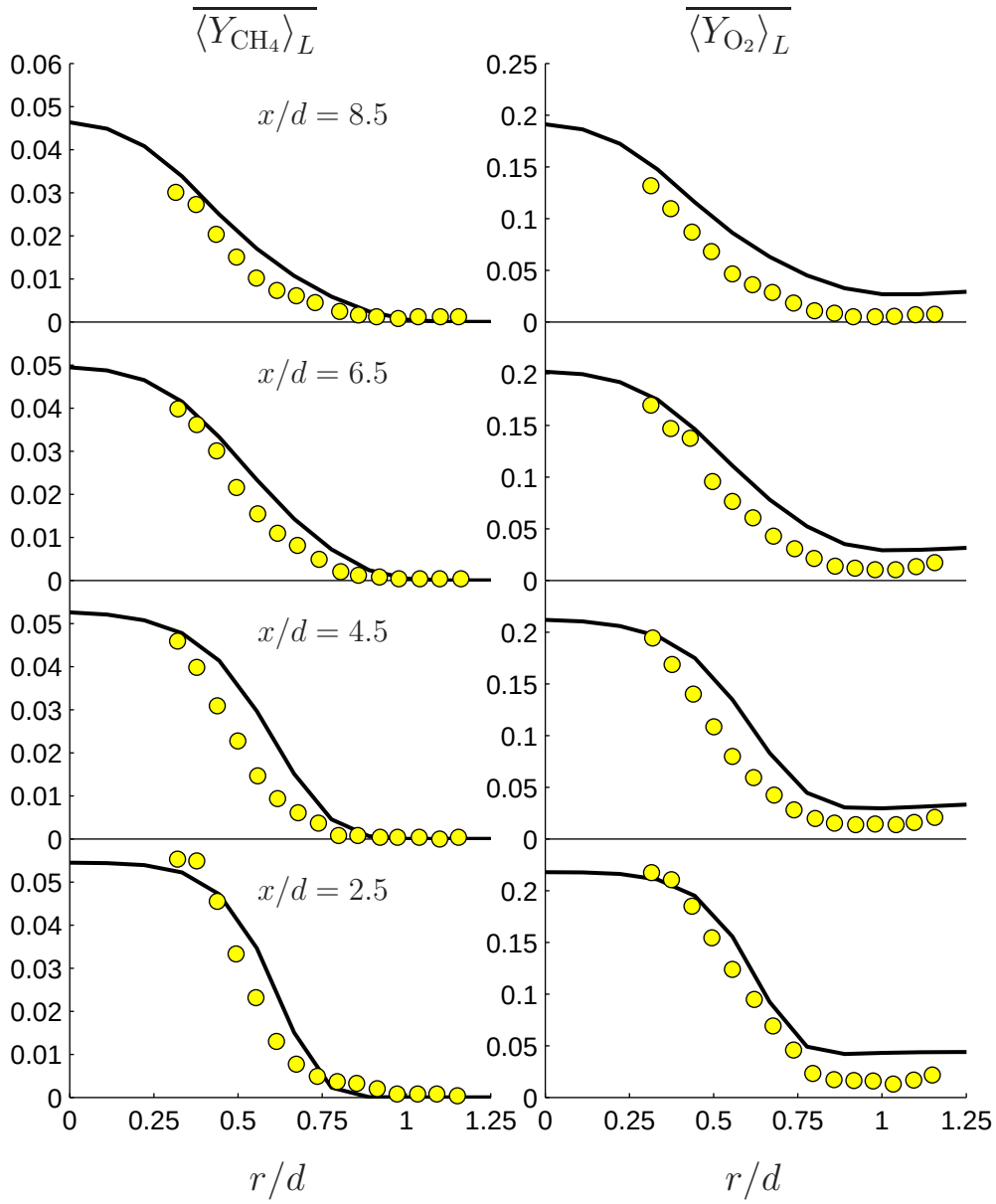

Figure 37: Bunsen burner, reacting flow: The radial profiles of the mean CH_4 and O_2 mass fractions. — LES/FDF, ○ Experimental measurements.[68]

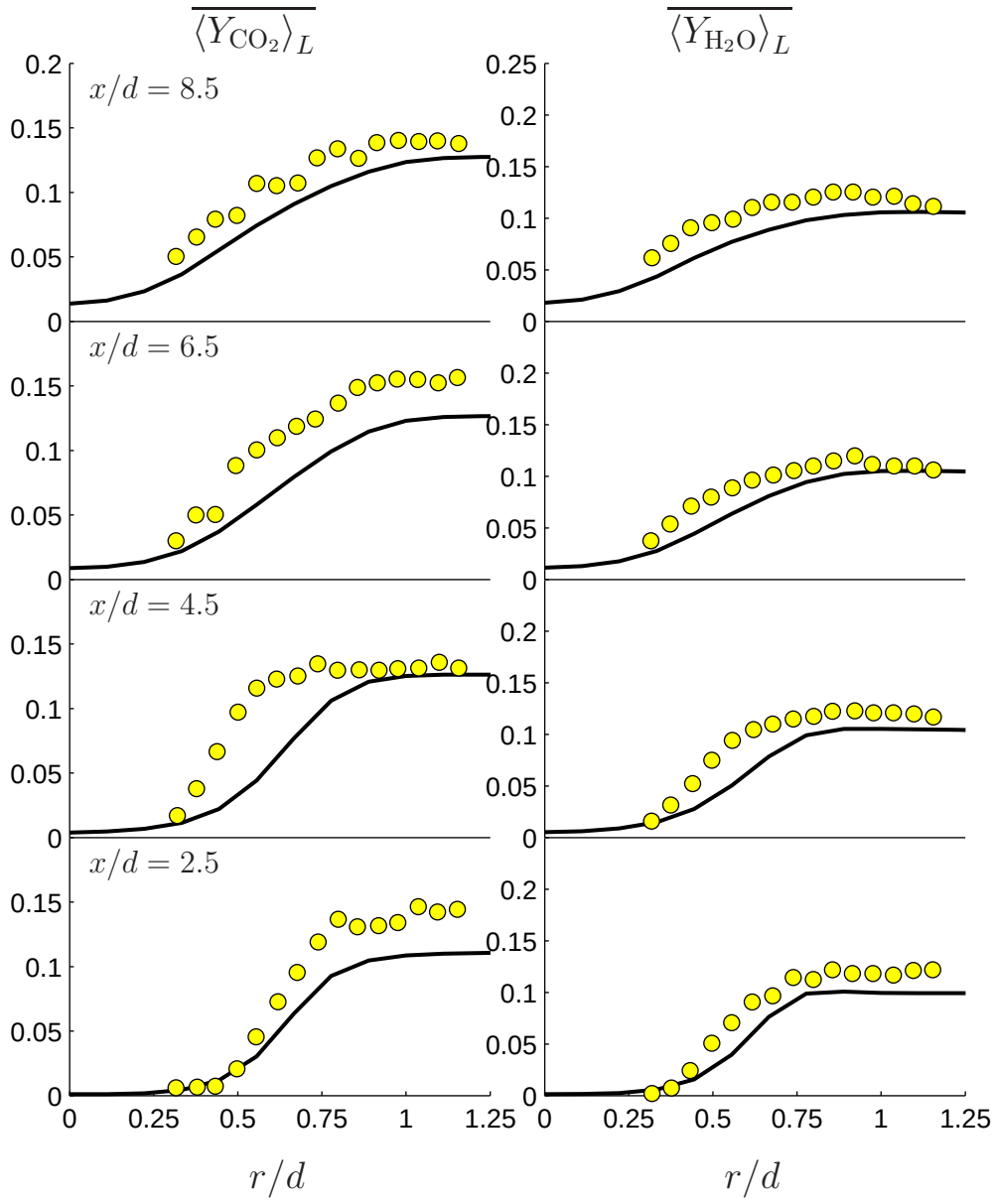

Figure 38: Bunsen burner, reacting flow: The radial profiles of the mean CO_2 and H_2O mass fractions. — LES/FDF, ○ Experimental measurements.[68]

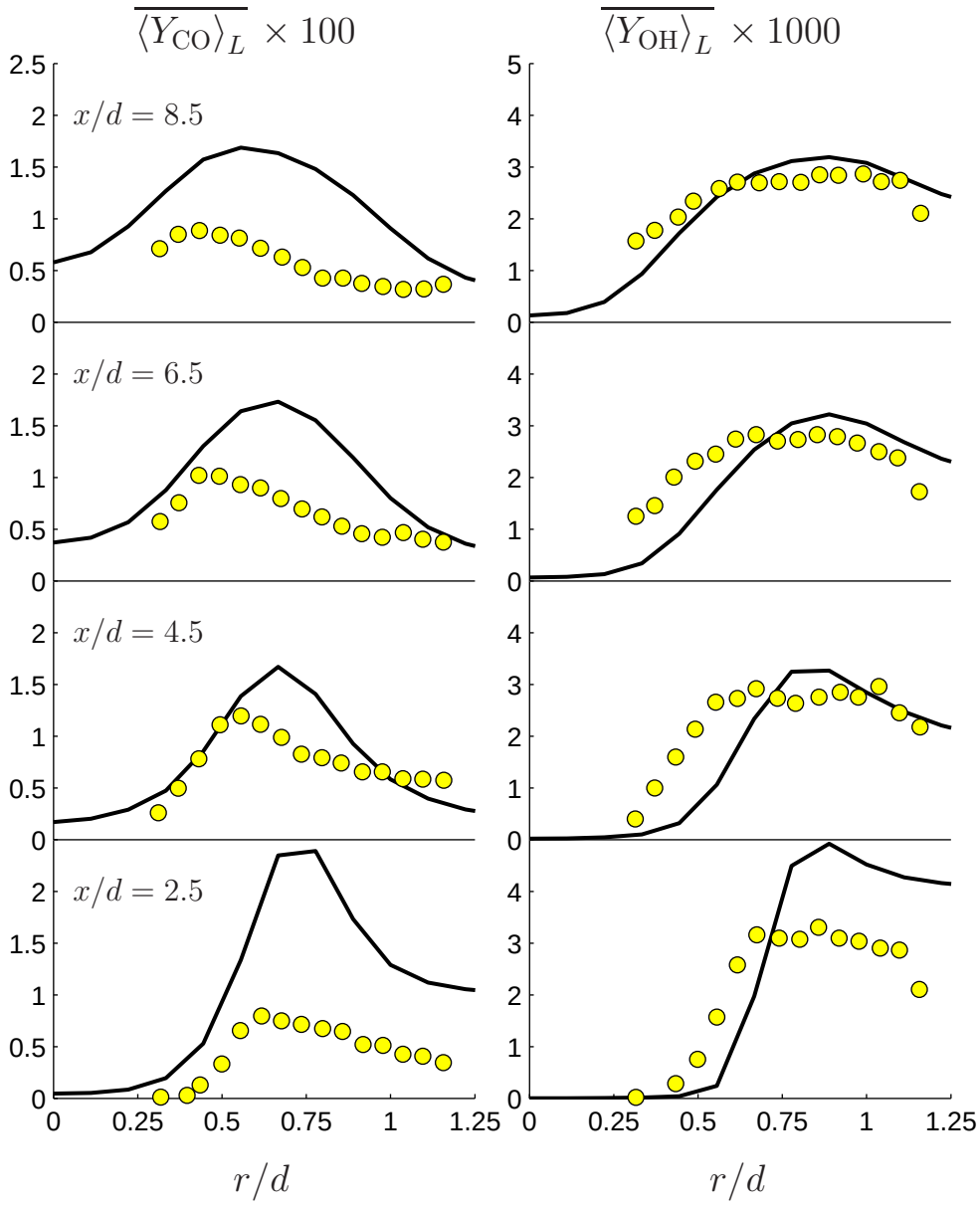

Figure 39: Bunsen burner, reacting flow: The radial profiles of the mean CO and OH mass fractions. — LES/FDF, ○ Experimental measurements.[68]

4.0 CONCLUDING REMARKS

RANS via PDF, and LES via FDF are at a stage that can be used for affordable, reliable and systematic prediction of turbulent reacting flows. This Dissertation demonstrates some of the applicabilities of these methodologies for simulation of turbulent premixed flames.

The velocity-scalar-frequency PDF is employed for prediction of a lean-premixed bluff body flame and the results are appraised via comparison with experimental data. In these simulations, methane oxidation is represented with a systematically reduced 5 step, 9 solved species reaction mechanism. Predictions are able to reproduce the location and the extent of the recirculation zone, and the mean values of the major species and temperature are in good agreements with data. Some of the minor species are not predicted well. For example, the simulated OH levels are much higher than the measured values close to the bluff body surface. But the NO levels are in a very close agreement at most locations inside recirculation zone and at the flame surface.

The scalar FDF methodology is employed for LES of a premixed Bunsen burner. Chemistry is represented via a systematically reduced 5 step, 9 solved species reaction mechanism. To enhance the efficiency of the LES/FDF computations a scalable parallelization algorithm is developed. This algorithm takes into account the variability of computational requirements throughout the domain, and decomposes the load accordingly. The FDF simulations are performed with significantly reduced turn-around times using this new methodology. After establishing the consistency of the hybrid solver, the predictions are compared with experimental data. The mean values of the mass fractions of the major and the minor species and temperature are predicted well, and unsteady effects are captured by the model. The CO levels are higher by almost a factor of 2 at the downstream region, where the predicted OH profiles are in good agreements with data.

There are several ways by which this work can be continued:

- Assessment of various chemistry mechanisms. Several parametric studies have been conducted for RANS/PDF predictions non-premixed flames.[141] Similar studies should be conducted for premixed flames via both RANS and LES.
- Use of more comprehensive FDF models for premixed flames. A more accurate account of turbulence-chemistry in LES can be made by the joint velocity-scalar FDF,[54,55,142] and the joint velocity-scalar-frequency FDF.[143]
- Inclusion of the effects of radiation and surface heat flux. Near the stabilizer, such effects are particularly important. Proper account for the heat loss would remedy this situation.
- Study of configurations with solid wall boundaries, and applications to more complex flames within realistic geometries.
- Extension of the FDF methodology to account for differential diffusion effects.[144–150] The models employed in this Dissertation are limited to flows with unity Lewis number. Proper account of such effects would improve the accuracy of minor species predictions, and is required in prediction of H_2/O_2 flames.

BIBLIOGRAPHY

[1] Dunn-Rankin, D., editor, *Lean Combustion: Technology and Control*, Academic Press, New York, NY, 2008.

[2] Richards, G. A., McMillian, M. M., Gemmen, R. S., Rogers, W. A., and Cully, S. R., Issues for Low-Emission, Fuel-Flexible Power Systems, *Prog. Energy Combust. Sci.*, **27**(2):141–169 (2001).

[3] Sidwell, T., Richards, G., Casleton, K., Straub, D., Maloney, D., Strakey, P., Ferguson, D., Beer, S., and Woodruff, S., Optically Accessible Pressurized Research Combustor for Computational Fluid Dynamics Model Validation, *AIAA J.*, **44**(3):434–443 (2006).

[4] Hack, R. L. and McDonell, V. G., Impact of Ethane, Propane, and Diluent Content in Natural Gas on the Performance of a Commercial Microturbine Generator, *J. Eng. Gas Turb. Power*, **130**(1):011509 (2008).

[5] Flores, R. M., Miyasato, M. M., McDonell, V. G., and Samuelsen, G. S., Response of a Model Gas Turbine Combustor to Variation in Gaseous Fuel Composition, *J. Eng. Gas Turb. Power*, **123**:824–831 (2001).

[6] Strakey, P. A., Sidwell, T., and Ontko, J., Investigation of the Effects of Hydrogen Addition on Lean Extinction in a Swirl Stabilized Combustor, *Proc. Combust. Inst.*, **31**(2):3173–3180 (2007).

[7] Strakey, P. A., Woodruff, S. D., Williams, T. C., and Schefer, R. W., OH-PLIF Measurements of High-Pressure, Hydrogen Augmented Premixed Flames in the SIMVAL Combustor, AIAA Paper 2007-980, AIAA, 2007.

[8] Schefer, R. W., Wicksall, D. M., and Agrawal, A. K., Combustion of Hydrogen-Enriched Methane in a Lean Premixed Swirl-Stabilized Burner, *Proc. Combust. Inst.*, **29**(1):843–851 (2002).

[9] Wicksall, D. M., Agrawal, A. K., Schefer, R. W., and Keller, J. O., Influence of Hydrogen Addition on Flow Structure in Confined Swirling Methane Flame, *J. Propul. Power.*, **21**(1):16–24 (2005).

[10] Givi, P., Spectral and Random Vortex Methods in Turbulent Reacting Flows, in Libby, P. A. and Williams, F. A., editors, *Turbulent Reacting Flows*, Chapter 8, pp. 475–572, Academic Press, London, UK, 1994.

[11] Pope, S. B., Computations of Turbulent Combustion: Progress and Challenges, *Proc. Combust. Inst.*, **23**:591–612 (1990).

[12] Poinsot, T., Candel, S., and Trouve, A., Applications of Direct Numerical Simulation to Premixed Turbulent Combustion, *Prog. Energy Combust. Sci.*, **21**:531–576 (1996).

[13] Vervisch, L. and Poinsot, T., Direct Numerical Simulation of Non-Premixed Turbulent Flames, *Annu. Rev. Fluid Mech.*, **30**:655–691 (1998).

[14] Pope, S. B., Advances in PDF Methods for Turbulent Reactive Flows, in Andersson, H. I. and Krogstad, P. A., editors, *Advances in Turbulence X*, CIMNE, pp. 529–536, 2004.

[15] Givi, P., Filtered Density Function for Subgrid Scale Modeling of Turbulent Combustion, *AIAA J.*, **44**(1):16–23 (2006).

[16] Pope, S. B., *Turbulent Flows*, Cambridge University Press, Cambridge, UK, 2000.

[17] Givi, P., Model Free Simulations of Turbulent Reactive Flows, *Prog. Energy Combust. Sci.*, **15**:1–107 (1989).

[18] Lundgren, T. S., Distribution Functions in the Statistical Theory of Turbulence, *Phys. Fluids*, **10**(5):969–975 (1967).

[19] O'Brien, E. E., The Probability Density Function (PDF) Approach to Reacting Turbulent Flows, in Libby, P. A. and Williams, F. A., editors, *Turbulent Reacting Flows*, *Topics in Applied Physics*, Vol. 44, Chapter 5, pp. 185–218, Springer-Verlag, Heidelberg, 1980.

[20] Pope, S. B., PDF Methods for Turbulent Reactive Flows, *Prog. Energy Combust. Sci.*, **11**:119–192 (1985).

[21] Fox, R. O., *Computational Models for Turbulent Reacting Flows*, Cambridge University Press, Cambridge, UK, 2003.

[22] Dopazo, C. and O'Brien, E. E., Statistical Treatment of Non-Isothermal Chemical Reactions in Turbulence, *Combust. Sci. Technol.*, **13**:99–112 (1976).

[23] Pope, S. B., The Probability Approach to Modeling of Turbulent Reacting Flows, *Combust. Flame*, **27**:299–312 (1976).

[24] Frost, V. A., Model of a Turbulent, Diffusion-Controlled Flame Jet, *Fluid Mech. Sov. Res.*, **4**:124–133 (1975).

[25] Pope, S. B., Lagrangian PDF Methods for Turbulent Flows, *Ann. Rev. Fluid Mech.*, **26**:23–63 (1994).

[26] Tolpadi, A. K., Correa, S. M., Burrus, D. L., and Mongia, H. C., Monte Carlo Probability Density Function Method for Gas Turbine Combustor Flowfield Predictions, *J. Propul. Power.*, **13**(2):218–225 (1997).

[27] Van Slooten, P. R., Jayesh, and Pope, S. B., Advances in PDF Modeling for Inhomogeneous Turbulent Flows, *Phys. Fluids*, **10**(1):246–265 (1998).

[28] Dreeben, T. D. and Pope, S. B., Probability Density Function / Monte Carlo Simulation of Near-Wall Turbulent Flows, *J. Fluid Mech.*, **357**:141–166 (1998).

[29] Hulek, T. and Lindstedt, R. P., Joint Scalar-Velocity PDF Modelling of Finite Rate Chemistry in a Scalar Mixing Layer, *Combust. Sci. Technol.*, **136**(1-6):303–331 (1998).

[30] Cannon, S. M., Brewster, B. S., and Smoot, L. D., PDF Modeling of Lean Premixed Combustion Using in Situ Tabulated Chemistry, *Combust. Flame*, **119**:233–252 (1999).

[31] Van Slooten, P. R. and Pope, S. B., Application of PDF Modeling to Swirling and Nonswirling Turbulent Jets, *Flow, Turbul. Combust.*, **62**(4):295–334 (1999).

[32] Xu, J. and Pope, S. B., PDF Calculations of Turbulent Nonpremixed Flames with Local Extinction, *Combust. Flame*, **123**:281–307 (2000).

[33] Muradoglu, K., Liu, K., and Pope, S. B., PDF Modeling of a Bluff-Body Stabilized Turbulent Flame, *Combust. Flame*, **132**:115–137 (2003).

[34] Masri, A. R., Cao, R., Pope, S. B., and Goldin, G. M., PDF Calculations of Turbulent Lifted Flames of H-2/N-2 Fuel Issuing into a Vitiated Co-flow, *Combust. Theor. Model.*, **8**(1):1–22 (2004).

[35] Vicente, W., Salinas, M., Barrios, E., and Dopazo, C., PDF Modeling of CO and NO Formation in Lean Premixed Methane Flames, *Combust. Sci. Technol.*, **176**(4):585–601 (2004).

[36] Cao, R. R., Pope, S. B., and Masri, A. R., Turbulent Lifted Flames in a Vitiated Coflow Investigated Using Joint PDF Calculations, *Combust. Flame*, **142**(4):438–453 (2005).

[37] Liu, K., Pope, S. B., and Caughey, D. A., Calculations of Bluff-Body Stabilized Flames Using a Joint Probability Density Function Model with Detailed Chemistry, *Combust. Flame*, **141**:89–117 (2005).

[38] Bilger, R. W., Pope, S. B., Bray, K. N. C., and F., D. J., Paradigms in Turbulent Combustion Research, *Proc. Combust. Inst.*, **30**:21–42 (2005).

[39] Lindstedt, R. P. and Ozarovsky, H. C., Joint Scalar Transported PDF Modeling of Nonpiloted Turbulent Diffusion Flames, *Combust. Flame*, **143**(4):471–490 (2005).

[40] Lindstedt, R. P. and Vaos, E. M., Transported PDF Modeling of High-Reynolds-Number Premixed Turbulent Flames, *Combust. Flame.*, **145**(3):495–511 (2006).

[41] Gordon, R. L., Masri, A. R., Pope, S. B., and Goldin, G. M., A Numerical Study of Auto-Ignition in Turbulent Lifted Flames Issuing into a Vitiated Co-Flow, *Combust. Theor. Model.*, **11**(3):351–376 (2007).

[42] Gkagkas, K. and Lindstedt, R. P., Transported PDF Modelling with Detailed Chemistry of Pre- and Auto-Ignition in CH4/Air Mixtures, *Proc. Combust. Inst.*, **31**:1559–1566 (2007).

[43] Wang, A., Modest, M. F., Haworth, D. C., and Wang, L. Y., Monte Carlo Simulation of Radiative Heat Transfer and Turbulence Interactions in Methane/Air Jet Flames, *J. Quant. Spectrosc. Radiat. Transfer*, **109**(2):269–279 (2008).

[44] Peters, N., *Turbulent Combustion*, Cambridge University Press, Cambridge, UK, 2000.

[45] Zhou, X. Y. and Pereira, J. C. F., Large Eddy Simulation (2D) of a Reacting Plan Mixing Layer Using Filtered Density Function, *Flow, Turbul. Combust.*, **64**:279–300 (2000).

[46] James, S. and Jaberi, F. A., Large Scale Simulations of Two-Dimensional Nonpremixed Methane Jet Flames, *Combust. Flame*, **123**:465–487 (2000).

[47] Sheikhi, M. R. H., Drozda, T. G., Givi, P., and Pope, S. B., Velocity-Scalar Filtered Density Function for Large Eddy Simulation of Turbulent Flows, *Phys. Fluids*, **15**(8):2321–2337 (2003).

[48] Raman, V., Pitsch, H., and Fox, R. O., Hybrid Large-Eddy Simulation/Lagrangian Filtered-Density-Function Approach for Simulating Turbulent Combustion, *Combust. Flame*, **143**(1-2):56–78 (2005).

[49] Sheikhi, M. R. H., Drozda, T. G., Givi, P., Jaberi, F. A., and Pope, S. B., Large Eddy Simulation of a Turbulent Nonpremixed Piloted Methane Jet Flame (Sandia Flame D), *Proc. Combust. Inst.*, **30**:549–556 (2005).

[50] Garrick, S. C., Jaberi, F. A., and Givi, P., Large Eddy Simulation of Scalar Transport in a Turbulent Jet Flow, in Knight, D. and Sakell, L., editors, *Recent Advances in DNS and LES*, *Fluid Mechanics and its Applications*, Vol. 54, pp. 155–166, Kluwer Academic Publishers, The Netherlands, 1999.

[51] Heinz, S., On Fokker-Planck Equations for Turbulent Reacting Flows. Part 2. Filter Density Function for Large Eddy Simulation, *Flow, Turbul. Combust.*, **70**(1-4):153–181 (2003).

[52] Carrara, M. and DesJardin, P., A Filtered Mass Density Function Approach for Modeling Separated Two-Phase Flows for LES I: Mathematical Formulation, *Int. J. Multiphase Flow*, **32**(3):365–384 (2006).

[53] Raman, V., Cook, D., and Pitsch, H., Hybrid LES/FDF Simulation of a Non-Premixed Bluff-Body Stabilized Flame, *Bull. Amer. Phys. Soc.*, **49**(9):57 (2004).

[54] Drozda, T., Sheikhi, M., Madnia, C., and Givi, P., Developments in Formulation and Application of the Filtered Density Function, *Flow, Turbul. Combust.*, **78**(1):35–67 (2007).

[55] Sheikhi, M. R. H., Givi, P., and Pope, S. B., Velocity-Scalar Filtered Mass Density Function for Large Eddy Simulation of Turbulent Reacting Flows, *Phys. Fluids*, **19**(9):095106 (2007).

[56] Réveillon, J. and Vervisch, L., Subgrid-Scale Turbulent Micromixing: Dynamic Approach, *AIAA J.*, **36**(3):336–341 (1998).

[57] Cha, C. M. and Troullet, P., A Subgrid-Scale Mixing Model for Large-Eddy Simulations of Turbulent Reacting Flows Using the Filtered Density Function, *Phys. Fluids*, **15**(6):1496–1504 (2003).

[58] Tong, C., Measurements of Conserved Scalar Filtered Density Function in a Turbulent Jet, *Phys. Fluids*, **13**(10):2923–2937 (2001).

[59] Wang, D. and Tong, C., Conditionally Filtered Scalar Dissipation, Scalar Diffusion, and Velocity in a Turbulent Jet, *Phys. Fluids*, **14**(7):2170–2185 (2003).

[60] Rajagopalan, A. G. and Tong, C., Experimental Investigation of Scalar-Scalar-Dissipation Filtered Joint Density Function and its Transport Equation, *Phys. Fluids*, **15**(1):227–244 (2003).

[61] Wang, D. H., Tong, C. N., and Pope, S. B., Experimental Study of Velocity Filtered Joint Density Function for Large Eddy Simulation, *Phys. Fluids*, **16**(10):3599–3613 (2004).

[62] Chandy, A., Goldin, G. M., and Frankel, S. H., Modeling Turbulent Non-Premixed Jet Flames Using Fluent's PDF Transport Model: Effect of Mixing Model on Flame Extinction, in *30th International Symposium on Combustion, Abstracts of Work-in-Progress Posters*, p. 447, Pittsburgh, PA, 2004, The Combustion Institute.

[63] Glaze, D. J., Frankel, S. H., and Hewson, J. C., Non-Premixed Turbulent Jet Mixing Using LES with the FMDF Model, in *30th International Symposium on Combustion, Abstracts of Work-in-Progress Posters*, p. 79, Pittsburgh, PA, 2004, The Combustion Institute.

[64] Heinz, S., On Fokker-Planck Equations for Turbulent Reacting Flows. Part 1. Probability Density Function for Reynolds-Averaged Navier-Stokes Equations, *Flow, Turbul. Combust.*, **70**(1-4):115–152 (2003).

[65] Jaberi, F. A., Madnia, C., and Givi, P., Large Eddy Simulation of Heat and Mass Transport in Turbulent Flows, in Minkowycz, W. J., Sparrow, E. M., and Murthy, J. Y., editors, *Handbook of Numerical Heat Transfer*, Chapter 5, pp. 167–190, John Wiley & Sons, Inc., New York, NY, 2nd edition, 2006.

[66] Pan, J. C., Laser-Diagnostic Studies of Confined Turbulent Premixed Flames Stabilized by Conical Bluff Bodies, PhD Thesis, The University of Dayton, Dayton, OH, 1991.

[67] Nandula, S. P., Pitz, R. W., Barlow, R. S., and Fiechtner, G. J., Rayleigh/Raman/LIF Measurements in a Turbulent Lean Premixed Combustor, AIAA Paper 96-0937, AIAA, 1996.

[68] Chen, Y.-C., Peters, N., Schneemann, G. A., Wruck, N., Renz, U., and Mansour, M. S., The Detailed Flame Structure of Highly Stretched Turbulent Premixed Methane-Air Flames, *Combust. Flame*, **107**(3):223–226 (1996).

[69] Williams, F. A., *Combustion Theory: The Fundamental Theory of Chemically Reacting Flow Systems*, Addison Wesley Publishing Company, Menlo Park, CA, 2nd edition, 1985.

[70] Brewster, B. S., Cannon, S. M., Farmer, J. R., and Meng, F., Modeling of Lean Premixed Combustion in Stationary Gas Turbines, *Prog. Energy Combust. Sci.*, **25**(4):353–385 (1999).

[71] Raman, V., Fox, R. O., and Harvey, A. D., Hybrid Finite-Volume/Transported PDF Simulations of a Partially Premixed Methane-Air Flame, *Combust. Flame.*, **136**(3):327–350 (2004).

[72] Lindstedt, R. P., Louloudi, S. A., and Vaos, E. M., Joint Scalar Probability Density Function Modeling of Pollutant Formation in Piloted Turbulent Jet Diffusion Flames with Comprehensive Chemistry, *Proc. Combust. Inst.*, **28**:149–156 (2000).

[73] Barlow, R. S. and Frank, J. H., Effects of Turbulence on Species Mass Fractions in Methane/Air Jet Flames, *Proc. Combust. Inst.*, **27**:1087–1095 (1998).

[74] Tang, Q., Xu, J., and Pope, S. B., PDF Calculations of Local Extinction and NO Production in Piloted-Jet Turbulent Methane/Air Flames, *Proc. Combust. Inst.*, **28**:133–139 (2000).

[75] Wang, H. and Pope, S. B., Lagrangian Investigation of Local Extinction, Re-Ignition and Auto-Ignition in Turbulent Flames, *Combust. Theor. Model.*, **12**(5):857–882 (2008).

[76] Dally, B. B., Masri, A. R., Barlow, R. S., and Fiechtner, G. J., Instantaneous and Mean Compositional Structure of Bluff-Body Stabilized Nonpremixed Flames, *Combust. Flame*, **114**:119–148 (1998).

[77] Masri, A. R., Pope, S. B., and Dally, B. B., PDF Computations of a Strongly Swirling Nonpremixed Flame Stabilised on a New Swirl Burner, *Proc. Combust. Inst.*, **28**:123–131 (2000).

[78] Fueyo, N., Vicente, W., Blasco, J., and Dopazo, C., Stochastic simulation of NO formation in lean premixed methane flames, *Combust. Sci. Technol.*, **153**:295–311 (2000).

[79] Nanduri, J. R., Parsons, D. R., Yilmaz, S. L., Celik, I. B., Givi, P., and Strakey, P. A., Effects of Turbulence Models, Turbulence-Combustion Interaction Models and Reaction Mechanisms on Prediction of Turbulent Combustion Emissions Using RANS-Based Methods, *Combust. Theor. Model.*, (2008), submitted.

[80] ANSYS Inc., FLUENT Commercial CFD Package (v6.2), `http://www.fluent.com/`, 2008.

[81] Lindstedt, R. P., Modeling of Chemical Complexities of Flames, *Proc. Combust. Inst.*, **27**:269–285 (1998).

[82] Smith, G. P., Golden, D. M., Frenklach, M., Moriarty, N. W., Eiteneer, B., Goldenberg, M., Bowman, C. T., Hanson, R. K., Song, S., Gardiner, J. W. C., Lissianski, V. V., and Qin, Z., GRI-MECH 3.0, `http://www.me.berkeley.edu/gri_mech/`, 2008.

[83] Favrè, A., Statistical Equations of Turbulent Gases, in *Problems of Hydrodynamics and Continuum Mechanics*, pp. 37–44, SIAM, Philadelphia, PA, 1969.

[84] Pope, S. B., Transport Equation for the Joint Probability Density Function of Velocity and Scalars in Turbulent Flow, *Phys. Fluids*, **24**(4):588–596 (1981).

[85] Ievlev, V. M., Approximate Equations of Turbulent Incompressible Fluid Flow, *Izv. Akad. Nauk. S.S.S.R. Mekh. Zhidk. Gaza*, **5**(1):91–103 (1970).

[86] Soong, T. T., *Random Differential Equations in Science and Engineering*, Academic Press, New York, NY, 1973.

[87] Arnold, L., *Stochastic Differential Equations: Theory and Applications*, Krieger Publishing Co., Malabar, FL, 1974.

[88] Karlin, S. and Taylor, H. M., *A Second Course in Stochastic Processes*, Academic Press, New York, NY, 1981.

[89] Coffey, W. T., Kalmykov, Y. P., and Waldron, J. T., *The Langevin Equation*, *World Scientific Series in Contemporary Chemical Physics*, Vol. 14, World Scientific Publishing Co., Hackensack, NJ, 2nd edition, 2004.

[90] Risken, H., *The Fokker-Planck Equation, Methods of Solution and Applications*, Springer-Verlag, New York, NY, 1989.

[91] Grigoriu, M., *Applied Non-Gaussian Processes*, Prentice-Hall, Englewood Cliffs, NJ, 1995.

[92] Kloeden, P. E., Platen, E., and Schurz, H., *Numerical Solution of SDE Through Computer Experiments*, Springer-Verlag, New York, NY, 3rd edition, 2002.

[93] Xu, J. and Pope, S. B., Assessment of Numerical Accuracy of PDF/Monte Carlo Methods for Turbulent Reacting Flows, *J. Comput. Phys.*, **152**:192–230 (1999).

[94] Muradoglu, M., Jenny, P., Pope, S. B., and Caughey, D. A., A Consistent Hybrid-Volume/Particle Method for the PDF Equations of Turbulent Reactive Flows, *J. Comput. Phys.*, **154**(2):342–371 (1999).

[95] Jaberi, F. A., Colucci, P. J., James, S., Givi, P., and Pope, S. B., Filtered Mass Density Function for Large Eddy Simulation of Turbulent Reacting Flows, *J. Fluid Mech.*, **401**:85–121 (1999).

[96] Muradoglu, M., Pope, S. B., and Caughey, D. A., The Hybrid Method for the PDF Equations of Turbulent Reactive Flows: Consistency Conditions and Correction Algorithms, *J. Comput. Phys.*, **172**:841–878 (2001).

[97] Mallampalli, H. P., Fletcher, T. H., and Chen, J. Y., Evaluation of CH_4/NO_x Reduced Mechanisms Used for Modeling Lean Premixed Turbulent Combustion of Natural Gas, *J. Eng. Gas Turb. Power*, **120**:703–712 (1998).

[98] Bowman, C. T., Hanson, R. K., Gardiner, W. C., Lissianski, V., Frenklach, M., Goldenberg, M., Smith, G. P., Crosley, D. R., and Golden, D. M., GRI-Mech 2.11–An Optimized Detailed Chemical Reaction Mechanism for Methane Combustion and NO Formation and Reburning, Report GRI-97/0020, Gas Research Institute, Chicago, IL, 1997.

[99] Rotta, J., Statistiche Theorie Nichththomogener Turbulenz, *Z. Phys.*, **129**:547–572 (1951), Translation in English available in NASA TM-14560 (1982).

[100] Afshari, A., Jaberi, F. A., and Shih, T. I. P., Large-Eddy Simulations of Turbulent Flows in an Axisymmetric Dump Combustor, *AIAA J.*, **46**(7):1576–1592 (2008).

[101] Williams, F. A., Turbulent Combustion, in Buckmaster, J. D., editor, *The Mathematics of Combustion*, SIAM, Philadelphia, PA, 1985.

[102] Peters, N., A Spectral Closure for Premixed Turbulent Combustion in the Flamelet Regime, *J. Fluid Mech.*, **242**:611–629 (1992).

[103] Peters, N., The Turbulent Burning Velocity for Large-Scale and Small-Scale Turbulence, *J. Fluid Mech.*, **384**:107–132 (1999).

[104] Osher, S. and Fedkiw, R. P., Level Set Methods: An Overview and Some Recent Results, *J. Comput. Phys.*, **169**(2):463–502 (2001).

[105] Prasad, R. O. S. and Gore, J. P., An Evaluation of Flame Surface Density Models for Turbulent Premixed Jet Flames, *Combust. Flame.*, **116**(1-2):1–14 (1999).

[106] Herrmann, M., Numerical Simulation of Turbulent Bunsen Flames with a Level Set Flamelet Model, *Combust. Flame*, **145**(1-2):357–375 (2006).

[107] Pitsch, H. and de Lageneste, L. D., Large-Eddy Simulation of Premixed Turbulent Combustion Using a Level-Set Approach, *Proc. Combust. Inst.*, **29**:2001–2008 (2002).

[108] Sagaut, P., *Large Eddy Simulation for Incompressible Flows*, Springer-Verlag, New York, NY, 3rd edition, 2005.

[109] Ghosal, S. and Moin, P., The Basic Equations for the Large Eddy Simulation of Turbulent Flows in Complex Geometry, *J. Comput. Phys.*, **118**:24–37 (1995).

[110] Vreman, B., Geurts, B., and Kuerten, H., Realizability Conditions for the Turbulent Stress Tensor in Large-Eddy Simulation, *J. Fluid Mech.*, **278**:351–362 (1994).

[111] Canuto, V. M., Large Eddy Simulation of Turbulence : A Subgrid Scale Model Including Shear, Vorticity, Rotation, and Buoyancy, *Astro. Phys. Journal*, **428**:729–752 (1994).

[112] Ciofalo, M., Large Eddy Simulation : A Critical Survey of Models and Applications, in *Advances in Heat Transfer*, pp. 321–419, Academic Press, New York, NY, 1994, Vol 25.

[113] Lesieur, M. and Metais, O., New Trends in Large Eddy Simulations of Turbulence, *Ann. Rev. Fluid Mech.*, **28**:45–82 (1996).

[114] Bardina, J., Ferziger, J. H., and Reynolds, W. C., Improved Turbulence Models Based on Large Eddy Simulations of Homogeneous, Incompressible, Turbulent Flows, Department of Mechanical Engineering Report TF-19, Stanford University, Stanford, CA, 1983.

[115] Eidson, T. M., Numerical Simulation of the Turbulent Rayleigh-Benard Problem using Subgrid Modelling, *J. Fluid Mech.*, **158**:245–268 (1985).

[116] Lundgren, T. S., Model Equation for Nonhomogeneous Turbulence, *Phys. Fluids*, **12**(3):485–497 (1969).

[117] Oran, E. S. and Boris, J. P., *Numerical Simulation of Reactive Flows*, Cambridge University Press, New York, NY, 2nd edition, 2001.

[118] Gardiner, C. W., *Handbook of Stochastic Methods for Physics, Chemistry and the Natural Sciences*, Springer-Verlag, New York, NY, 2nd edition, 1990.

[119] Carpenter, M. H., A High-Order Compact Numerical Algorithm for Supersonic Flows, in Morton, K. W., editor, *Twelfth International Conference on Numerical Methods in Fluid Dynamics*, *Lecture Notes in Physics*, Vol. 371, pp. 254–258, Springer-Verlag, New York, NY, 1990.

[120] Poinsot, T. J. and Lele, S. K., Boundary Conditions for Direct Simulations of Compressible Viscous Flows, *J. Comput. Phys.*, **101**:104–129 (1992).

[121] Poinsot, T. and Veynante, D., *Theoretical and Numerical Combustion*, R.T. Edwards, Inc., Philadelphia, PA, 2nd edition, 2005.

[122] Law, C. K. and Lu, T. F., Towards Accommodating Realistic Fuel Chemistry in Large-Scale Computations, AIAA Paper 2008-969, AIAA, 2008.

[123] Peters, N., Reducing Mechanisms, in Smooke, M. D., editor, *Reduced Kinetic Mechanisms and Asymptotic Approximations for Methane-Air Flames*, *Lecture Notes in Physics*, Vol. 384, Chapter 3, pp. 48–67, Springer-Verlag, Berlin, 1991.

[124] Maas, U. and Pope, S. B., Simplifying Chemical-Kinetics - Intrinsic Low-Dimensional Manifolds in Composition Space, *Combust. Flame.*, **88**(3-4):239–264 (1992).

[125] Lu, T. F., Ju, Y. G., and Law, C. K., Complex CSP for Chemistry Reduction and Analysis, *Combust. Flame.*, **126**(1-2):1445–1455 (2001).

[126] Djouad, R., Sportisse, B., and Audiffren, N., Reduction of Multiphase Atmospheric Chemistry, *J. Atmos. Chem.*, **46**(2):131–157 (2003).

[127] Blasco, J. A., Fueyo, N., Larroya, J. C., Dopazo, C., and Chen, Y. J., A Single-Step Time-Integrator of a Methane-Air Chemical System Using Artificial Neural Networks, *Comput. Chem. Eng.*, **23**(9):1127–1133 (1999).

[128] Chen, J. Y., Blasco, J. A., Fueyo, N., and Dopazo, C., An Economical Strategy for Storage of Chemical Kinetics: Fitting In Situ Adaptive Tabulation with Artificial Neural Networks, *Proc. Combust. Inst.*, **28**:115–121 (2000).

[129] Blasco, J. A., Fueyo, N., Dopazo, C., and Chen, J. Y., A Self-Organizing-Map Approach to Chemistry Representation in Combustion Applications, *Combust. Theor. Model.*, **4**(1):61–76 (2000).

[130] Montgomery, C. J., Yang, C. G., Parkinson, A. R., and Chen, J. Y., Selecting the Optimum Quasi-Steady-State Species for Reduced Chemical Kinetic Mechanisms Using a Genetic Algorithm, *Combust. Flame.*, **144**(1-2):37–52 (2006).

[131] Lu, T. F. and Law, C. K., A Directed Relation Graph Method for Mechanism Reduction, *Proc. Combust. Inst.*, **30**:1333–1341 (2005).

[132] Lu, T. F. and Law, C. K., Linear Time Reduction of Large Kinetic Mechanisms with Directed Relation Graph: *n*-Heptane and Iso-Octane, *Combust. Flame.*, **144**(1-2):24–36 (2006).

[133] Pope, S. B., Computationally Efficient Implementation of Combustion Chemistry using *in situ* Adaptive Tabulation, *Combust. Theor. Model.*, **1**(1):41–63 (1997).

[134] Brown, P. N., Bryne, G. D., and Hindmarsh, A. C., VODE:A Variable-Coefficient ODE Solver, *SIAM J. Sci. Stat. Comp.*, **10**(5):1038–1051 (1989).

[135] Colucci, P. J., Jaberi, F. A., Givi, P., and Pope, S. B., Filtered Density Function for Large Eddy Simulation of Turbulent Reacting Flows, *Phys. Fluids*, **10**(2):499–515 (1998).

[136] Karypis, G. and Kumar, V., *MeTis: Unstrctured Graph Partitioning and Sparse Matrix Ordering System, Version 4.0*, University of Minnesota, Minneapolis, MN, 1998.

[137] Lu, T. and Law, C. K., An Efficient Reduced Mechanism for Methane Oxidation with NO Chemistry, in *Joing Meeting of the U.S. Sections of the Combustion Institute*, University of California at San Diego, 2007.

[138] Danaila, I. and Boersma, B. J., Direct Numerical Simulation of Bifurcating Jets, *Phys. Fluids*, **12**(5):1255–1257 (2000).

[139] Rudy, D. H. and Strikwerda, J. C., A Nonreflecting Outflow Boundary Condition for Subsonic Navier-Stokes Calculations, *J. Comput. Phys.*, **36**:55–70 (1980).

[140] Gicquel, L. Y. M., Givi, P., Jaberi, F. A., and Pope, S. B., Velocity Filtered Density Function for Large Eddy Simulation of Turbulent Flows, *Phys. Fluids*, **14**(3):1196–1213 (2002).

[141] Cao, R. R. and Pope, S. B., The Influence of Chemical Mechanisms on PDF Calculations of Nonpremixed Piloted Jet Flames, *Combust. Flame*, **143**(4):450–470 (2005).

[142] Givi, P., Sheikhi, M. R. H., Drozda, T. G., and Madnia, C. K., Large Scale Simulation of Turbulent Combustion, *Combust. Plasma Chem.*, **6**(1):1–9 (2008).

[143] Sheikhi, M. R. H., Givi, P., and Pope, S. B., Frequency-Velocity-Scalar Filtered Mass Density Function for Large Eddy Simulation of Turbulent Reacting Flows, *in progress*, (2008).

[144] Jaberi, F. A., Miller, R. S., Mashayek, F., and Givi, P., Differential Diffusion in Binary Scalar Mixing and Reaction, *Combust. Flame*, **109**:561–577 (1997).

[145] Smith, L. L., Dibble, R. W., Talbot, L., Barlow, R. S., and Carter, C. D., Laser Raman Scattering Measurements of Differential Molecular Diffusion in Nonreacting Turbulent Jets of H_2/CO_2 Mixing with Air, *Phys. Fluids*, **7**(6):1455–1466 (1995).

[146] Kerstein, A. R., Cremer, M. A., and McMurtry, P. A., Scaling Properties of Differential Molecular Diffusion Effects in Turbulence, *Phys. Fluids*, **7**(8):1999–2007 (1995).

[147] Long, M. B., Starner, S. H., and Bilger, R. W., Differential Diffusion in Jets using Joint PLIF and Lorenz-Mie Imaging, *Combust. Sci. Technol.*, **92**:209–224 (1993).

[148] Nilsen, V. and Kosaly, G., Differential Diffusion in Turbulent Reacting Flows, *Combust. Flame.*, **117**(3):493–513 (1999).

[149] Yeung, P. K., Xu, S. Y., and Sreenivasan, K. R., Schmidt number effects on turbulent transport with uniform mean scalar gradient, *Physics Of Fluids*, **14**(12):4178–4191 (2002).

[150] McDermott, R. and Pope, S. B., A Particle Formulation for Treating Differential Diffusion in Filtered Density Function Methods, *J. Comput. Phys.*, **226**:947–993 (2007).